UNIVERSITY OF SHEFFIELD

On Advanced Channel Modelling for Network Planning

by

Jialai Weng

Faculty of Engineering
Department of Electronic and Electrical Engineering

October 2017

Declaration of Authorship

Part of the work included in this thesis has been published in the following publications:

2015 **An Averaging Path Loss Prediction Model Based on Ray Tracing** (Jialai Weng, Cong Wang, Jie Zhang) *Accepted In ZTE Communications*

2015 **A Mathematical Formulation for Channel Map and Its Application in MIMO Systems** (Jialai Weng, Wuling Liu, Haonan Hu, Xiaoli Chu, Jie Zhang) *In Antennas and Propagation Conference (LAPC), 2015 Loughborough*

2015 **A Simulation Based Distributed MIMO Network Optimisation Using Channel Map** (Jialai Weng, Jonathan M. Rigelsford, and J. Zhang) *PIERS (Progress In Electromagnetics Research Symposium), Prague, Czech Republic*, July 2015.

2015 **Modelling the mmWave Channel Based on Intelligent Ray Launching Model** (Jialai Weng, Xiaoming Tu, Zhihua Lai, Jie Zhang), *In Antennas and Propagation (EUCAP), Proceedings of the 9th European Conference on*, April, 2015.

2014 **Indoor Massive MIMO Channel Modelling Using Ray-Launching Simulation** (Jialai Weng, Xiaoming Tu, Zhihua Lai, Sana Salous, Jie Zhang), *In International Journal of Antennas and Propagation*, 2014

2014 **Capacity Field: Modelling Channel Capacity from Electromagnetic Propagation Perspective** (Jialai Weng, Xiaoming Tu, Jie Zhang), *In Antennas and Propagation (EUCAP), Proceedings of the 8th European Conference on*, 2014.

The rest part of the work during my PhD has not been included in this thesis. They are in preparation to be published or have been published as:

2015 **Wireless Channel Capacity from Electromagnetic Perspective** (Jialai Weng)In Preparation

2015 **The Impact of Propagation Mechanisms on Wireless Channel Capacity** (Jialai Weng)In Preparation

2015 **An Averaging Path Loss Prediction Model Based on Ray Tracing** (Jialai Weng, Jie Zhang) In Press

2015 Coverage Performance Analysis of FeICIC Low Power Subframes (Haonan Hu, Jialai Weng, Jie Zhang), submitted to IEEE Transaction on Wireless Communications, Accepted

2015 How Densely Should Wireless Networks be Deployed? (Jialai Weng, Haonan Hu, Jie Zhang)*In The University of Sheffield Engineering Symposium (USES) 2015*, June, 2015

2015 A Network Deployment Strategy for Home Area Networks in Smart Grid (Dehua Li, Jialai Weng, Xiaoli Chu, Jie Zhang) *2015 IEEE 25th International Symposium on Personal, Indoor and Mobile Radio Communications - (PIMRC)*

2014 On the Use of an Intelligent Ray Launching in MIMO channel Modelling for Network Planning (Xiaoming Tu, Jialai Weng, S. Salas, Jie Zhang), *In General Assembly and Scientific Symposium (URSI GASS), 2014 XXXIth URSI*, pp. 1-4, 2014.

2013 A Dual-Polarisation Modelling Method for Simulation-based Propagation Models (Jialai Weng, Zhihua Lai, Jie Zhang), *In Antennas and Propagation Conference (LAPC), 2013 Loughborough*, pp. 436-440, 2013.

2013 Realistic Prediction of BER and AMC with MRC Diversity for Indoor Wireless Transmissions (Meiling Luo, G. Villemaud, Jialai Weng, J.-M. Gorce, Jie Zhang), *In Wireless Communications and Networking Conference (WCNC), 2013 IEEE*, pp. 4059-4064, 2013.

2011 Channel Measurement and Characterization of Interference Between Residential Femto-cell Systems (Xiang Gao, A. Alayon Glazunov, Jialai Weng, Cheng Fang, Jie Zhang, F. Tufvesson), *In Antennas and Propagation (EUCAP), Proceedings of the 5th European Conference on*, pp. 3769-3773, 2011.

UNIVERSITY OF SHEFFIELD

Abstract

Faculty of Engineering
Department of Electronic and Electrical Engineering

by Jialai Weng

With the increasing demand for high speed wireless network services, the next generation wireless networks are proposed to use advanced wireless communication technologies. These technologies include massive MIMO, mmWave and distributed MIMO. In order to deploy wireless networks equipped with these technologies, channel models capturing the channel features and characteristics of these wireless technologies are essential in the planning and optimisation of networks. However, conventional channel models lack the capability to support these next generation network technologies. In this PhD thesis, I investigated the channel models for the next generation wireless technologies, including massive MIMO, mmWave communications and distributed MIMO. I developed channel models for network planning and optimisation based on conventional ray launching algorithms for these wireless technologies. The models have been validated and applied to optimise network performance. The existing challenge in wireless channel modelling is the improvement of modelling accuracy without increasing modelling complexity. In order to achieve this goal, a new calibration method is developed to improve the accuracy of the predication model when measurements are available. Moreover, in order to use the channel models as an effective tool in wireless network planning and optimisation, a new wireless capacity definition from radio propagation perspective is also investigated. It provides insight to the physical limit of wireless channel capacity from a radio propagation perspective.

Acknowledgements

First, I would like to thank my PhD supervisor Prof. Jie Zhang. He helped me to choose the research project on channel modelling. Through the PhD research project, his support and advice inspired many interesting research discussion and exploration. Without his help and guidance, this thesis would be impossible.

Second, I would like to thank the thesis examiners, Prof. Sana Salous and Dr. Jonathan Rigelsford for their meticulous review and valuable comments to the first submission of this thesis. Their review and feedback significantly improved the quality of this thesis.

Third, I would like to thank many colleagues from the Communication Research Group: Dr. Xiaoli Chu, Mr. Wuling Liu, Mr. Dehua Li, Mr. Haonan Hu, Mr. Yue Wu, Mr. Ran Tao, Mr. Qi Hong and Miss Hui Zheng. Thank you! It is a lovely experience to work with you in the communication group. Thank you for all the discussions and help!

I would also like to thank my collaborators at Ranplan Wireless Network Design: Dr. Zhihua Lai, Mr. Xiaoming Tu and Mr. Hanye Hu. Thank you for your help!

Last but not least, I would like to thank Prof. Sana Salous at Durham University for hosting me as a visiting PhD student in 2013 to 2014 and offering me research opportunity to work on channel measurement.

Contents

List of Figures

List of Tables

Abbreviations

2.5D	**2.5 D**imensional
3D	**3 D**imensional
3GPP	**3**rd **G**eneration **P**artnership **P**roject
4G	4th **G**eneration
5G	5th **G**eneration
CDMA	**C**ode **D**ivision **M**ultiple **A**ccess
EM	**E**electro**M**agnetics
FDTD	**F**inite **D**ifference **T**ime **Domain**
GA	**G**enetic **A**lgorithm
GR	**GR**eedy Algorithm
GO	**G**eometric **O**ptics
HetNet	**H**eterogeneous **N**etwork
LS	**L**east **S**quare
LTE	**L**ong **T**erm **E**volution
LTE-A	**L**ong **T**erm **E**volution **A**dvanced
MIMO	**M**ultiple **I**nput **M**ultiple **O**utput
mmWave	Millimetre **W**ave
RMS	**R**oot **M**ean **S**quare
UMTS	**U**niversal Mobile **T**elecommunications **S**ystem
UTD	**U**niform **T**heory of **D**iffraction
WISE	**W**ireless **S**ystem **E**ngineering

Chapter 1

Background and Research Problems

1.1 Introduction

With the increasing demand for wireless data services, current wireless networks are facing challenges to support high quality of service. The next generation wireless networks are designed to support 1000x capacity increase with low latency and high energy efficiency. Network planning and optimisation are stages in the process of wireless network deployment to achieve high quality of service. A site-specific radio propagation channel model is designed to provide channel information to the network deployment site. By utilising the radio propagation channel model, the network deployment and optimisation process can be carried out through the computer aided network design and simulation tools. Such a computer aided design process significantly reduces the network deployment cost and improves the design quality in the network deployment and planning process. In order to efficiently plan and optimise radio access networks, a radio propagation channel model is essential.

With the future communication techniques for 5G networks, such as massive multiple-input and multiple-output (MIMO) and millimetre wave (mmWave) communications, conventional propagation channel models fail to incorporate the advanced 5G communication techniques. Radio channel modelling is facing challenges to provide accurate propagation channel models for future 5G network planning and optimisation. Moreover, conventional propagation channel models lack the capability to characterise the performance limits of the wireless network from radio propagation perspective, which

is the fundamental limit in wireless communication systems. In order to characterise the fundamental limit to the wireless communication networks, a new perspective on wireless communication capacity from radio propagation physics is needed.

In this PhD research project, I investigate novel propagation channel models by considering 5G communication techniques including massive MIMO and mmWave communications. I developed propagation channel models for network planning and optimisation applications equipped with these 5G techniques. Furthermore, I developed a novel wireless channel capacity definition from electromagnetic propagation perspective to address the physical limit for the wireless communication systems. This new wireless channel capacity definition has potential to be used in studying the radio propagation mechanisms on the wireless communication performance.

1.2 Background

Wireless network planning is the design of wireless networks to achieve optimal performance with minimum cost. With the increasing demand for high data rate network traffic and higher cost of operating communication networks, to achieve the optimal performance with minimum cost is a challenge that most network operators face. Modern network planners resort to computer-aided network planning tools to facilitate the complex task of network planning and to achieve the goal of optimal network performance.

One of the key tasks of network planning is to find the optimal locations of the network deployment nodes. The task can be performed based on the network coverage requirement and the network capacity requirement. To perform the location optimisation algorithm, a channel information map that describes the channel information of the planning space is therefore essential.

Most simulation-based channel prediction tools estimate the channel information maps via various channel models. In this regard, a channel model plays a central role in the construction of channel information map for network planning. With the future 5G communication techniques such as massive MIMO and millimetre wave communication techniques, new channel models are needed for the deployment and optimisation for future networks equipped with these techniques.

Moreover, network capacity is one of the key performance metrics in network planning and optimisation. Current network planning tools focus on the signal coverage performance. Designing a network planning tool directly addressing the network capacity from the radio propagation channel perspective is necessary to understand the fundamental capacity limits.

In this part, I first give a literature review on the topic of network node location optimisation. Next, I review the state-of-the-art of channel modelling works for 5G networks including: massive MIMO, millimetre wave channel, distributed MIMO and a new model calibration method. At last, I review the channel capacity as a concept from the electromagnetic perspective.

1.2.1 Wireless Network Planning

Network planning is to design wireless networks before the physical deployment of the network. It consists of 5 steps, dimensioning, pre-planning, detailed-planning, verification and optimisation [1]. Each stage of the network planning process has its specific goal. The overall purpose of the network planning process is to achieve the optimal network performance at minimum cost.

In each stage, the network planner performs different tasks. For a typical network planning process, the five stages of the planning process consist of the following specific planning tasks. For the Dimensioning stage, the task is to assess the planning scale and to give an estimation of the required number of base stations and other network resources. The Planning stage has two tasks, coverage planning and capacity planning. The target of coverage planning is to achieve satisfactory network coverage. The capacity planning is to allocate network capacity with the consideration of service quality requirements. The Detailed Planning stage has three detailed tasks, frequency planning, neighbour planning and parameter planning. The stages of the network planning are given in the following flow chart.

Network deployment is a highly complex task. There are numerous factors to consider in the deployment of a large wireless networks. On one hand, the demand of high data rate network service increased exponentially in recent years with the development of mobile technologies. However, on the other hand, the resources to support high data

rate communication such as energy and frequency band, are ever more scarce. Under such demanding conditions, to deploy and operate the wireless networks with high standard service quality at minimum cost is key to the network operators. The purpose of network planning is to achieve the optimal network deployment scheme.

Early works in network planning focused on achieving coverage planning. The early work of [2] gave a non-linear optimisation model for the problem of finding the optimal transmitter location in micro-cellular networks. The work of [3] investigated the optimisation algorithms for the base station location placement in Universal Mobile Telecommunications System (UMTS) networks, with the consideration of not only signal coverage but both of network traffic and power control. Following this research, the work of [4] made the effort to optimise the UMTS network coverage by optimising the antenna configuration, which can be seen as a step further ahead from base station location optimisation. The recent work of [5] studied the optimisation algorithms for base station placement and proposed a hierarchical search algorithm for the optimisation problem. The network base station location optimisation problem has been an active research topic since the second generation wireless network and it is still a key problem for the next generation networks, such as heterogeneous networks (HetNet) [6].

To achieve the target of optimal base station deployment, a signal coverage map over the deployment space is essential. Various candidate locations in the map are compared and the optimal one is chosen. Such a coverage map is widely used in the network planning practice. Many researches have been devoted in building such a coverage map for the network planning purpose. The pioneering work in [7] partitioned the map into areas and adopted empirical model to predict the path loss contour plot as a path loss map. The work in [8] followed this method and extended it to an outdoor-indoor transient situation. To accurately predict the channel information requires significant amount of computation, therefore many research works are devoted to computer-based simulation. Early works such as the WISE tools by Bell Labs [9] and the CINDOOR [10] were specially designed for designing and planning indoor networks. The method of building such channel maps is mainly a deterministic channel propagation model, which contains roughly two major modelling methods: FDTD related models and ray based models. The work in [11] first used the name of channel map and proposed a ray tracing method for building the channel map. The work in [12] proposed an efficient

computational electromagnetic method for building the channel map. For a complete review of the channel modelling in HetNet works, we refer the readers to the work of [6]. The channel map has long been widely used as an essential tool in network design. However, it still lacks a rigorous mathematical formulation, which limits the further development of the channel map as an essential tool in network planning, especially for MIMO network planning.

The early work in [9] introduced computer aided network planning software WISE. The concept is to facilitate the complex network planning process through an interactive two stage computer prediction and then optimisation process. The software employs propagation channel models to predict the signal coverage of the design space first. Then in the second stage an optimisation algorithm is used to find the optimal base station locations based on the channel prediction information in the first stage. The WISE software comprises 5 key components : propagation model, building information database, channel prediction, base station optimisation and graphical user interface. The software WISE first raised a computer aided solution to the complex networking planning process. The target of the optimal network planning solution is to find the optimal locations for the base stations in the network to support satisfying network service. The key to achieve this goal is to model the location finding problem as an optimisation problem and then apply a suitable searching algorithm to obtain the optimal solution. In this regard, the channel prediction became a key component in supporting the searching for the optimal locations of base stations. One distinctive characteristic of the channel prediction information for using as input to the optimal base station location search algorithm, is that the channel information is associated with physical location information.

The work in [13] followed the work of WISE and proposed a novel combinatorial optimisation algorithm for the direct search for the optimal base station location, other than the simple algorithm used in WISE. The authors also compared the performance of the Genetic Algorithm (GA) and the Greedy Algorithm (GR) and showed the advantage of the combinatorial algorithm. The authors pointed out that the optimal base station location problem can be solved by various searching algorithms: GA, GR, Simplex and simulated annealing. However the work adopted the same optimisation model as in the work of WISE. This model requires the channel prediction information with physical location information to provide the necessary input for the optimal location

search algorithm. Another early research work of optimal location of transmitter is [2]. This work adopted a different optimisation model and a different definition for network coverage. In this work, the authors set out to search the whole network design space to find the optimal base station location while in [9] and [13], the optimisation is to search for a set of potential candidate locations. Furthermore, the authors used the minimum sum path loss as the network coverage criterion. This new definition led to the new objective function in the optimisation algorithm. The authors proposed 3 objective functions based on different network planning constraints. The resulting optimisation problem is a nonlinear programming problem and 3 algorithms were proposed to solve the problem. Although this work proposed a different base station location optimisation model, the importance of the channel information associated with location information remains central to the base station location optimisation problem. To find the optimal base station location, the channel information is required to be mapped on to the physical locations.

A research work focused on optimal transmitter location in UMTS networks is given in [3]. This work is the first research work focused on CDMA networks with special consideration of power control. The authors pointed out that for the third generation wireless networks the transmitter location optimisation model needs to incorporate other network planning considerations, such as capacity, in the planning process. This is a new planning model different from the early second generation networks. In the second generation networks the planning contains two independent stage: coverage planning and capacity planning, while in this work the authors proposed to consider both criterion jointly in the planning stage. This concept has then been adopted by many researchers in 3G and later wireless networks [14].

With a new optimisation model proposed, however, the requirements to the channel prediction model remains the same. For the location optimisation problem, with joint consideration of network traffic, power control, frequency allocation, the channel information together with location information is essential to implement the location optimisation algorithms. The work in [4] is a more recent work following the work of [3]. The authors focused on the specific command channel in the UMTS networks and considered detailed antenna configurations. However, to optimise the service coverage and even the antenna configuration in this work, an accurate channel information map for the targeted network planning area remains a vital part of the planning process. The

work in [5] represents a very recent research effort on the topic of transmitter location optimisation. The authors proposed novel iterative algorithms for jointly finding the minimum number of base stations and the optimal base station locations. The success of the optimisation algorithm depends on an accurate and efficient channel information map as an input to the optimisation programme.

The above reviewed literatures focus on the location optimisation problem research development in network planning. Their usage of the channel prediction model is representative as the common requirements for channel models, from network planning purposes. Although they deal with various network planning aspects, a common characteristic feature we can draw for the channel prediction model from these works is: they all require channel information associated with location information and the optimisation procedure is carried out based on the channel location information.

1.2.2 Channel Modelling for Network Planning

Channel models give physical characteristics that are of interest to the applications. With an appropriate channel model, the channel characteristics can be predicted based on limited model inputs, while still without a comprehensive measurement of the channel. Channel modelling is essential to the design of communication networks. It facilitates the prediction of communication design by avoiding the measurement of the channel information. An accurate channel model guarantees the success of the communication system design.

Some channel characteristics are key to the evaluation of the network performance. Most commonly used channel characteristic parameters are: power parameters; spatial parameters; and temporal parameters. The work of [15] is a recent tutorial on channel models.

In a network planning process, the network planner uses the channel models to predict the channel characteristics. Based on this predicted channel information, the planner estimates the performance of the network deployment scheme. One of the most important network planning tasks is to finding the optimal locations for the base stations. This poses a direct requirement on the channel characteristics that are usable in the location planning stage: the channel characteristics are required to be associated with

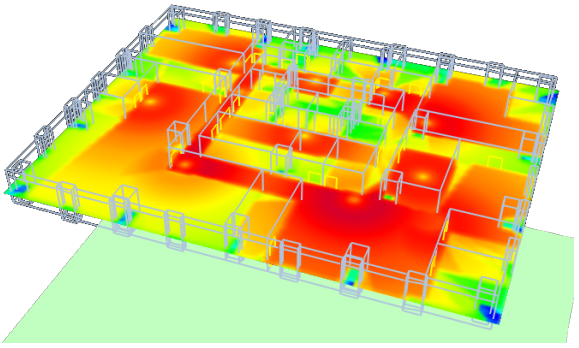

FIGURE 1.1: An Example of Channel Map for Indoor Network Planning

location information. In this sense, the network planning process requires a channel characteristics map, a channel map for short.

Channel map is a representation of the channel characteristics of certain channel coverage space, associated with location information in a form of 2-dimensional or 3-dimensional map. The channel characteristics are normally obtained by channel prediction models or by measurements. Such a concept was first proposed in the work of [11]. The channel map represents the channel characteristics over location information in a form of map. These channel characteristics include signal power, path loss and delay, depending on the network planning requirements. An example of a channel map is given in Figure 1.1.

Location planning is one key planning task in network planning. It is the foundation for the subsequent network planning stages, such as frequency planning and parameter planning. Especially in coverage planning the criterion is to evaluate the overall design space, not to a single receiving location. In this regard, a channel map for the design space is a direct way to give an overall description of the channel characteristics.

1.2.3 Ray Optics for Radio Propagation Prediction: A Brief History

One of the most popular methods to construct a channel map for wireless network planning and optimisation is using ray-based radio propagation simulation. The ray-based propagation is a high frequency approximation for electromagnetic wave propagation. It has been widely used as an efficient numerical method for computational electromagnetics. Here we give a brief review of the ray-based method in radio propagation prediction.

Ray-based propagation simulation methods can be roughly divided into two groups: ray launching and ray tracing. Ray launching simulate the radio wave propagation from the radio wave source. The radio waves are approximated as rays transmitted from the radio wave source. In contrast, the ray tracing method traces the propagating rays back to the source. In network planning, the ray launching method is widely adopted in modelling the propagation channels, as ray launching simulates the radiation and propagation of radio waves and generates the channel coverage map for network planning applications.

In [16], the authors implemented one of the earliest computer simulation based channel prediction software tools. The authors first derived a theoretical model for predicting the mean field strength based on ray optics. The model followed the same authors earlier work on the mean field strength model in urban streets in [17]. The ray optics model considered reflection and diffraction of the building environment in an urban city environment. The author implemented the model in a computer simulation tool for prediction of the propagation channel in the centre of Kyoto city environment.

The work in [18] was another early work on the ray launching model for propagation prediction. The authors focused on the channel characteristics of power delay profile and delay spread. The ray launching considered reflection, transmission and diffraction rays to emulate multipath propagation of radio channels. This work demonstrated that deterministic ray launching is capable of modelling statistical channel characteristics such as delay spread.

The Bell Labs Wireless System Engineering (WISE) software system is another early work on computer simulation based channel prediction tools [9]. The WISE system used ray launching to predict the signal coverage map. The software was first released for indoor environments. To reduce the computational complexity, WISE employed a 2.5D simplification of the environment. Later WISE was extended to the outdoor environment in [19] and further implemented in 3D simulation in [20].

Later, research works focused on improving the efficiency of the ray launching simulation as the original 3D ray optics simulation cost high computational loads. The work in [21] introduced a ray tube method. It groups the 3D rays into groups of ray tube and constructs ray tube trees based on the ray tubes. The ray tube tree then decides the ray paths to trace in the simulation. This method improved the ray tracing simulation

efficiency by reducing the ray path testing computation in the conventional simulation. Another work aimed to reduce the ray path testing is reported in [22, 23]. The work introduced the angular Z-Buffer (AZB) technique to reduce the time of identifying the ray paths. Motivated by the same purpose, the work in [24] also focused on reducing the judgement time in identifying the ray paths. The authors proposed a triangular grid method to model the ray propagation. By setting the environment to be a triangular grid, the rays enter one triangle only require to be tested on 2 edges of the triangle to decide its path, which reduces the computational time.

More recent works have focused on further improving the efficiency of ray optics model through preprocessing the environment for highly efficient ray optics simulation. The work in [25] preprocessed the environment by cube rasterisation and proposed a cube oriented ray launching (CORLA) algorithm for ray optics propagation simulation. The work in [26] implemented an intelligent ray launching algorithm in parallel computation to improve efficiency. The work in [27] proposed an efficient rasterisation implementation on GPU for parallel computation.

The ray optics models predicted the channel information in urban environment in the aforementioned works are all compared with measurement results. The error between the channel simulation results and the measurement varies from 3dB to 8dB, which is considered accurate in urban city environment.

1.3 Challenges

In the last section, I reviewed the network planning and optimisation literature and the literature on the ray optics for channel modelling. In this part, I point out the current challenges in channel modelling for network planning and optimisation in 5G wireless networks.

1.3.1 Massive MIMO Channel Models

Massive MIMO is to equip a large number of antennas at both the transmitter and the receiver. Compared with conventional MIMO systems, massive MIMO systems are normally equipped with a large number of antennas, for example, 64 by 64. It offers

a large number of degree-of-freedom (DoF) supported by the large antenna arrays. It also offers flexibility in the use of the antennas, such as multiuser beamforming and interference coordination.

Because it supports a large number of spatial DoF and flexibility in applications, it is endorsed as one of the key techniques in 5G networks [28]. Furthermore, it makes MIMO communications benefit realisable comparing to the conventional MIMO equipped with a small number of antennas.

There has been research applying the ray-based models to model MIMO channels. The work of [29] is an early research work using ray-tracing to model MIMO channel. The work focused on the limiting factors on channel capacity in MIMO system. Later, the work of [30] proposed to predict the MIMO channel using ray-tracing due to its computational efficiency under the setting with a small number of antennas. Moreover the work of [31] studied a similar model focusing on the verification of the channel capacity results. This work verified the simulation results with measurements in an indoor scenario with a 2×2 MIMO system. Furthermore, the work of [32] also studied the MIMO channel matrix based on ray-tracing: not only channel capacity but various channel parameters such as angular and delay parameters have also been characterised based on ray-tracing models. As a ray-tracing model can provide multipath information, it can be exploited for modelling various multipath channel parameters. So the work of [33] proposed a multipath channel model based on applying ray-tracing model. The MIMO channel parameters have been further derived based on this model. With various MIMO models being proposed, the work of [34] compared the 3D ray-tracing MIMO channel models and various statistical models.

The aforementioned research works of ray-based MIMO channel modelling, have focused on modelling the conventional MIMO system with a small number of antennas. A ray-based model specifically for massive MIMO system is still missing. Although some of the models can be applied to model the massive MIMO channel, the performance, especially the computational efficiency is unsatisfying to the demand of network planning and optimisation purpose. The primary challenge of modelling the massive MIMO channel using ray-based site-specific models, especially for applications in wireless network deployment, is the high computational cost, caused by the large number

of antennas. A computationally efficient site-specific channel model for massive MIMO is still missing.

1.3.2 Millimetre Wave Channel Models

The frequency band from 30 GHz to 300 GHz has the wavelength from 1 millimetre to 10 millimetres. This frequency band used to be reserved for radio astronomy and remote sensing. There are many unlicensed frequency bands in the mmWave frequency range.

With the increasingly high demand for radio spectrum resources for future networks, the rich unlicensed spectrum in mmWave frequency band is proposed to be used in the 5G networks [35]. It offers rich radio frequency spectrum resources to the currently crowded network frequency spectrum. It is deemed as one of the key techniques in the 5G networks [28].

The mmWave frequency band has been used in radar [36], interchip communication [37, 38], in-car communication [39] and in-cabin communication [40] and in-flight communication [41] and wireless backhaul [42]. Recently it has been endorsed as one promising technique in 5G networks [28, 35].

In order to utilise the mmWave channel in 5G networks, more work focused on the modelling and characterisation of the mmWave channels. The work in [43] gives a multipath clustering model for indoor mmWave channel. The work in [44] characterised the effects of human bodies on the propagation of mmWave channel. The work in [45] studied the capacity gain of using mmWave channels based on channel measurement data.

The work in [46] reviewed the statistical characterisation including large scale fading and small scale parameters of the 60 GHz indoor channel from published measurement. The work in [47] developed spatial statistical models for 28 GHz and 73 GHz using urban measurements. The work in [48] carried measurements at 38 GHz in urban environments and channel characteristics were extracted from the measurements.

1.3.3 Distributed MIMO

By deploying the MIMO system through a distributed antenna system, the MIMO system is implemented in a distributed fashion. A distributed MIMO system can offer flexibility in deployment to overcome the half wavelength antenna distance constraints of MIMO arrays. On the other hand, a distributed MIMO system can utilise the multipath propagation more efficiently for it can avoid correlation between antennas by deploying the antennas in a distributed fashion. A distributed MIMO system can be deployed to support reliable and high-throughput data links in wireless backhaul connections.

In Small Cell networks and Heterogeneous Networks, it is important to provide a reliable and high throughput data link to support the backhaul connections. In complex indoor environment where multipath propagation dominates, distributed MIMO offers an ideal solution to support the wireless backhaul connections.

To achieve the target of optimal base station deployment, a signal coverage map over the deployment space is essential. Various candidate locations in the map are compared and the optimal one is chosen. Such a coverage map is widely used in the network planning practice. A large amount of effort has been devoted in building such a coverage map for network planning purposes. The pioneering work in [7] partitioned the map into areas and adopted the empirical model to predict the path loss contour plot as a path loss map, which is extended in [8] to an outdoor-indoor transient scenario. To accurately predict the channel information requires significant amount of computation and resources, hence computer-based simulation tools such as the WISE tool by Bell Labs [9] and the CINDOOR [10] were specially designed for planning indoor networks. The method of building such channel maps is mainly based on two deterministic channel modelling methods: finite-difference time-domain (FDTD) related models and ray based models. The work in [11] first used the name of channel map and proposed a ray tracing method for building the channel map. The work in [12] proposed a computationally efficient numerical method for building the channel map. A complete review of the channel modelling in HetNet can be found in [6]. The channel map has long been widely used as an essential tool in network design. However, it still lacks a rigorous mathematical formulation thereby limiting the further application of the channel map as an essential tool in network planning, especially for MIMO network planning.

Channel maps and channel models are used interchangeably in the channel modelling community. This stems from the fact that the electromagnetic simulation based channel models outputs a channel modelling result in the form of a channel map, such as [12, 49]. However, according to the definition of channel model in [50], the concept of channel map is different from channel model, although channel models provide the basis for building a channel map. There has been no rigorous definitions for channel map.

With the application of advanced wireless transmission techniques, such as MIMO, the network performance is largely improved [6]. Meanwhile, to plan networks equipped with these advanced techniques is challenging, especially due to a lack of rigorous formulation for the channel map. This limits the application and functionality of the channel map as a tool in advanced network planning, such as MIMO network planning.

1.3.4 Hybrid Propagation Model

Physical propagation model based on radio wave propagation offers high accuracy. However, it has the drawback of high complexity and high computational cost. On the other hand, empirical model is computationally efficient but offers low accuracy. In order to improve the efficiency of the physical models, a hybrid model is designed to determine physical model parameters through available channel measurement. In such a way, the complex physical modelling is avoided and the computational cost is reduced.

In many network planning and optimisation applications to construct a channel map, it is important to have an efficient channel model. By reducing the computational complexity and cost of the physical models, a hybrid model offers an efficient modelling method for channel map construction for network planning and optimisation.

The ray optics algorithm has a long history of being employed to simulate the multipath propagation nature of the wireless channel. The early work in [17] first proposed to model the geometric mean value of the multipath channel components using the ray optics method in city street environments. This optic ray based model has been extended to model the mean channel strength a large urban environment of Tokyo in [16]. The Bell Labs also developed a ray tracing simulation based channel prediction software tool (WISE) first for indoor environment [9], then extended to 2D urban environments [19]

and full 3D urban environments [20]. The work in [18] developed a ray launching model to model the wireless channel parameters via the simulation of reflection, transmission and diffraction of ray propagation mechanisms for the indoor environment. For the outdoor environment, the work in [51] employed the ray launching model to predict the path loss values. In order to improve the modelling accuracy, the effective building material properties, which use the measurement to calibrate the modelling parameters, have been introduced in [52].

On the other hand, more work has been focused on improving the computational efficiency of the ray optics based simulation channel models. The work in [24, 25, 27] proposed more efficient 3D environment modelling and processing methods for ray optics simulation. These efficient environment modelling and processing methods significantly improved the computational efficiency of the ray optics simulation based channel prediction models.

Despite the aforementioned research works on using ray optics as an effective channel modelling tool, a ray tracing model which directly models the path loss values is still missing. The conventional electromagnetic ray tracing algorithm computes the electromagnetic field, which is a complex value. In order to consider the multipath effect in the path loss calculation, the complex number field values are summed and squared to calculate the power loss from the field value. Such a way is computationally costly. Furthermore, the model is required to use the theoretical values to model the parameter. This makes it almost impossible to calibrate the modelling parameter via electromagnetic measurements. Because the electromagnetic measurement measures the power values while the model only calculates the field values.

1.3.5 Capacity from Electromagnetic Perspective

With the development of modern computer-aided network planning tools, the complex task of network planning is integrated with the design of the propagation environment, such building construction and materials. It is observed that the propagation environment influences the network performance. The challenge is to identify the direct connection between the network performance and the environment.

The challenge arises from the optimal design of network performance by jointly designing the network deployment and the building construction. A direct connection between the network performance and the environment makes such joint design of network and building environment feasible.

Conventional works build network performance parameters via the predicted channel information, for example, in [53]. However, such a method offers little insight to the fundamental connection between the network performance and the environment. This way is even cumbersome in the design and planning of networks.

The purpose of the research is to formulate a connection between the propagation environment and the network performance parameters. Such a connection is vital to the understanding of the influence of environment on the network performance. It significantly simplifies the network planning process.

Moreover, It makes the integrated design of building and network feasible, by considering the direct interconnection between the potential building design and the network planning design. The ultimate goal of the joint design of building and networks requires a direct connection between network performance and propagation environment. The application of such a connection facilitates both the design and construction of a new building with high performance networks. From this perspective, both building constructors and network planners are benefited if this insight is put into application.

1.4 Contributions

In the previous section, I introduced the challenges and research problems currently facing the propagation channel modelling for network planning and optimisation. In this section, I give a brief introduction to the contributions I have done during this PhD project to address these challenges and research problems.

1.4.1 Massive MIMO

I developed a 4 simplified modelling methods for a site-specific ray launching simulation model for massive MIMO in indoor environments. The 4 modelling methods are based on ray launching algorithm. In order to improve the efficiency, I developed a the

simplified versions of the model utilising the antenna array geometry and also channel characteristics. The modelling results are validated by channel measurement data. Comparison also shows that the simplified model improved computational efficiency in simulation. This results demonstrated that the complexity of massive MIMO channel models can be reduced by incorporating the physical properties of the channel and the characteristics of the massive MIMO channel.

1.4.2 mmWave Channel

I developed a ray based path loss prediction model for mmWave channel. This model utilises the characteristic of the high attenuation in mmWave channel. Based on ray launching to simulate the multipath propagation, it uses a simple average multipath loss values to model the total path loss value. The modelling results are validated by channel measurements in an indoor environment. This model offers an efficient solution to the site-specific mmWave channel modelling.

1.4.3 Distributed MIMO

I extended the single antenna simulation channel map to MIMO systems. By extending the single antenna channel map concept to a vector case, I apply the same single antenna ray launching simulation model to construct a distributed MIMO channel map. The simulation model is applied to a distributed MIMO backhaul link optimisation case. The simulation results show that the simulation tool supports the planning and optimisation of distributed MIMO networks. This results demonstrated that a vector channel map for MIMO network can be constructed based on the single antenna channel maps.

1.4.4 Channel Model Calibration

I developed a channel model calibration method based on the least squares (LS) method. The model is based on the path loss model developed in Chapter 3 and in Chapter 5. In this chapter, I parametrised the model to accommodate the loss values of the propagation mechanisms. I also extended the model to consider the incidence angle as a modelling parameter. The modelling parameters are calibrated using this LS calibration

method and the available measurement data. The results show that this LS method is effective in improving the accuracy of the simulation model when measurements are available.

1.4.5 Channel Capacity from Electromagnetic Perspective

I introduced a new wireless channel capacity definition based on electromagnetic wave propagation. The capacity values of an enclosed volume space for both a sphere volume space and a cube volume space are calculated. The impact of the volume of space and the antenna types on the total channel capacity is studied and compared. This wireless channel capacity result showed potential in the application of indoor wireless network planning and optimisation.

1.5 Thesis Overview

This rest of this thesis is structured as follows: In Chapter 2, I investigate the channel modelling for massive MIMO. In Chapter 3, I present the work on mmWave channel modelling. Chapter 4 gives the distributed MIMO channel map method and the simulation results on distributed MIMO optimisation. Chapter 5 presents a new calibration method for the ray launching based path loss model based on the LS method. In Chapter 6, I present the work on the new definition of wireless channel capacity from electromagnetic perspective. Chapter 7 concludes the thesis.

Chapter 2

Indoor Massive MIMO Channel Modelling using Ray Launching

2.1 Introduction

Massive MIMO is to equip a large number of antennas at both the transmitter and the receiver in a wireless communication system. It is also known as large array system. Massive MIMO has the advantage of providing both higher spectral efficiency and power efficiency. Recently, massive MIMO has been widely accepted as a promising technique for the next generation wireless communication system [54]. See both [55] and [56] for a recent survey on the topic of massive MIMO systems.

Site-specific channel modelling is to model the channel using the environment information and physical radio propagation model to obtain the channel information for specific scenarios. Popular site-specific channel models are electromagnetic propagation based methods such as finite-difference time-domain (FDTD) and ray-based methods. One of the major applications for the site-specific channel models is wireless network deployment. The ray launching algorithm is especially suitable for this application purpose due to the modelling efficiency [57].

In ray launching simulation, the environment model is built based on site maps or building floor maps. The propagation parameters can either from empirical value or from measurement. In this chapter, the values of the propagation parameters are from

empirical values such as the values provided in [58]. In Chapter 5, I will present a calibration method to calibrate the parameter values using available measurement data.

Wireless network planning and optimisation is one of the major applications of the site-specific channel models. To optimise the locations of the network nodes, such as base station, a large number of potential locations is predicted, which is computationally demanding. Furthermore, large network deployment environments, such as shopping malls and airports, also pose high computational demands on the prediction model. Therefore, for the application of network deployment and optimisation, a computationally efficient channel model is highly desirable.

There has been research work applying the ray-based models to model MIMO channels. The work of [29] is an early research work using ray-tracing to model MIMO channels. The work focused on the limiting factors on channel capacity in MIMO systems. Later, the work of [30] proposed to predict the MIMO channel using ray-tracing due to its computational efficiency under the setting with a small number of antennas. Moreover the work of [31] studied a similar model focusing on verification of the channel capacity results. This work verified the simulation results with measurements in an indoor scenario with a 2×2 MIMO system. Furthermore, the work of [32] also studied the MIMO channel matrix based on ray-tracing: not only channel capacity but various channel parameters such as angular and delay parameters have also been characterised based on ray-tracing models. As ray-tracing model can provide multipath information, it can be exploited for modelling multipath channel parameters. So the work of [33] proposed a multipath channel model based on applying ray-tracing model. The MIMO channel parameters have been further derived based on this model. With various MIMO models being proposed, the work of [34] compared the 3D ray-tracing MIMO channel models and various statistical models.

The aforementioned research works of ray-based MIMO channel modelling, has all focused on modelling the conventional MIMO system with a small number of antennas. A ray-based model specifically for massive MIMO system is still missing. Although some of the models can be applied to model massive MIMO channel, the performance, especially the computational efficiency is unsatisfactory for the demand of network planning

and optimisation purpose. The primary challenge of modelling massive MIMO channel using ray-based site-specific models, especially for applications in wireless network deployment, is the high computational cost, caused by the large number of antennas.

Another popular site-specific channel modelling tool for network planning is the FDTD method and related models [12]. A comparison study between the ray launching method and the frequency domain Par-Flow model is presented in [59]. Although the FDTD and related methods offer an accurate solution to simulate the propagation channel, these methods suffer from high computational cost in simulation especially in high frequency band. On the other hand, in high frequency band ray launching offers a desirable solution with high computational efficiency even at the cost of slightly lower accuracy. The work in this chapter will show that ray launching offers an accurate channel modelling solution with moderate computational complexity.

To address the computational efficiency challenge of modelling massive MIMO channel for wireless network deployment application, we propose to apply a computationally efficient Intelligent Ray Launching Algorithm [26] to model massive MIMO systems in site-specific scenarios. Its inherent 3D modelling capability and high computational efficiency make it a highly desirable model for network planning and optimisation application.

The purpose of the chapter is to propose 4 ray-launching based models in massive MIMO channel modelling for indoor wireless network deployment application. The first ray-launching model is a direct application of ray-launching to massive MIMO modelling. Based on the first model, we propose a simplified model. Later we further propose ray-launching based probabilistic channel models. These models have the advantage of computational efficiency in massive MIMO modelling. Furthermore comparison between the model simulation results and channel measurements shows good agreements.

The organisation of the chapter is as follows: In Section 2.2.1 we establish the 4 ray-launching based models for massive MIMO channel. In Section 2.3 we present the simulation and measurement scenarios. In Section 2.4.1 we analyse and discuss the simulation results. Section 2.5 concludes the work.

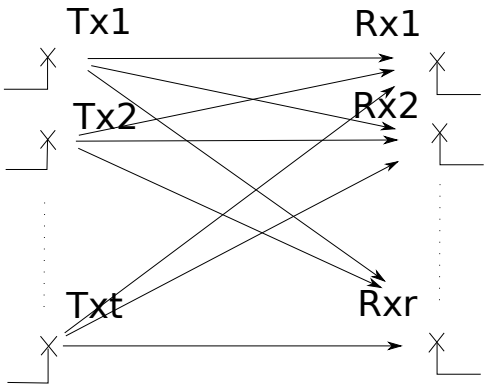

FIGURE 2.1: MIMO Transmitter and Receiver Scheme

2.2 MIMO Modelling using Ray Launching

2.2.1 Model 1: Deterministic Ray-Launching Model for Massive MIMO

A MIMO system has multiple antennas both at the transmitter and at the receiver. Figure 2.1 illustrates a MIMO channel. The transmitter is equipped with a t-element antenna array and the receiver is equipped with a r-element antenna array. The MIMO channel is then written in the form of a matrix

$$\mathbf{H} = \begin{bmatrix} H_{1,1} & H_{1,2} & \cdots & H_{1,r} \\ H_{2,1} & H_{2,2} & \cdots & H_{2,r} \\ \vdots & \vdots & \ddots & \vdots \\ H_{t,1} & H_{t,2} & \cdots & H_{t,r} \end{bmatrix} \tag{2.1}$$

The matrix element $H_{m,n}$ characterises the channel between the transmitter element n and the receiver element m. In a site-specific channel prediction scenario, the MIMO channel matrix is a function of the locations of the network deployment site. Thus we can write the channel as in (2.2): In this work, we are interested in finding the set of MIMO channel matrices over the targeted network deployment site. We assume the MIMO channel is narrow band throughout the chapter.

$$\mathbf{H}(x,y,z,\omega) = \begin{bmatrix} H_{1,1}(x,y,z,\omega) & H_{1,2}(x,y,z,\omega) & \cdots & H_{1,r}(x,y,z,\omega) \\ H_{2,1}(x,y,z,\omega) & H_{2,2}(x,y,z,\omega) & \cdots & H_{2,r}(x,y,z,\omega) \\ \vdots & \vdots & \ddots & \vdots \\ H_{t,1}(x,y,z,\omega) & H_{t,2}(x,y,z,\omega) & \cdots & H_{t,r}(x,y,z,\omega) \end{bmatrix} \tag{2.2}$$

Ray is an accurate model for the electromagnetic propagation in high frequency and has been a popular modelling tool due to its accuracy and efficiency. Ray-based models are based on the geometric optics (GO) and uniform theory of diffraction (UTD)[60]. Ray launching is a propagation model to simulate the transmission of the electromagnetic waves by tracing along the rays from the transmitter. In wireless channel modelling, ray launching has the advantage of capturing the multipath propagation nature of the wireless channel. According to the ray-launching model, each ray can be seen as an individual multipath component. Following the multipath propagation using ray-launching, we can write the channel element between the receiver n and the transmitter m in the time domain as

$$h_{m,n}(t,\tau) = \sum_{\alpha=1}^{q} A_\alpha \mathrm{e}^{-j\omega_0(t+\tau_\alpha)} \cdot \delta(\tau - \tau_\alpha)$$

where A_α is the amplitude of the α-th ray; q is the total number of rays; τ is the time delay and τ_α is the delay of the α-th ray.

In a static environment, the channel is static. Thus we have $h(t,\tau) = h(t=0,\tau)$. We can then write the channel delay response as the function of the delay τ

$$h_{m,n}(\tau) = \sum_{\alpha=1}^{q} A_\alpha \mathrm{e}^{-j\omega_0(\tau_\alpha)} \cdot \delta(\tau - \tau_\alpha)$$

Taking the Fourier Transform with respect to the time delay τ, we have the frequency response of the channel:

$$H_{m,n}(\omega) = \sum_{\alpha=1}^{q} A_\alpha \mathrm{e}^{-j(\omega_0+\omega)\tau_\alpha}$$

If we set the angular frequency $\omega = 0$, we have the channel frequency response at the central angular frequency ω_0. Due to the delay spread, we have a band-pass shape in the frequency domain, and the frequency band is determined as the coherent bandwidth in wireless communication channel modelling. However, for the purpose of wireless network deployment, especially for indoor scenarios where the delay spread is small, the primary channel parameter we are interested in is the channel frequency response at the central angular frequency ω_0.

$$H_{m,n}(\omega_0) = \sum_{\alpha=1}^{q} A_\alpha \mathrm{e}^{-j\omega\tau_\alpha}$$

As the ray-launching model traces the ray parameters such as the amplitude A_α and delay τ_α along the ray in the ray propagation space; we can further write the above equation as a function of the locations in the ray coverage space as:

$$H_{m,n}(x, y, z, \omega_0) = \sum_{\alpha=1}^{q} A_\alpha(x, y, z)\mathrm{e}^{-j\omega\tau_\alpha(x,y,z)} \tag{2.3}$$

This equation gives the channel frequency response as a result of the summation of the rays or multipath components. It is the mathematical relationship we use to obtain the channel from the ray-launching model.

By applying this relationship, the ray-launching model can be used to predict the set of MIMO channel matrices over the targeted network deployment site. We can write the channel frequency response as in (2.4), where the individual channel element $H_{m,n}(x, y, z, \omega_0)$ is given by the equation in (2.3).

The channel parameters, the amplitude $A_\alpha(x, y, z)$ and the delay $\tau_\alpha(x, y, z)$ are given by the ray-launching model based on GO and UTD. The model calculates each channel element according to (2.3) sequentially, until all the elements are calculated. To obtain a complete set of MIMO channel matrices of the network deployment site, the prediction is repeated over the locations of the deployment site, until the set of locations (x, y, z) covers the deployment site. Figure 2.2 shows an example of ray-launching model in an indoor office environment.

We name the above model as Model 1. To further improve the computational efficiency, next we propose a simplified model based on this model.

$$\mathbf{H}(x, y, z, \omega_0) = \begin{bmatrix} H_{1,1}(x, y, z, \omega_0) & H_{1,2}(x, y, z, \omega_0) & \cdots & H_{1,r}(x, y, z, \omega_0) \\ H_{2,1}(x, y, z, \omega_0) & H_{2,2}(x, y, z, \omega_0) & \cdots & H_{2,r}(x, y, z, \omega_0) \\ \vdots & \vdots & \ddots & \vdots \\ H_{t,1}(x, y, z, \omega_0) & H_{t,2}(x, y, z, \omega_0) & \cdots & H_{t,r}(x, y, z, \omega_0) \end{bmatrix} \tag{2.4}$$

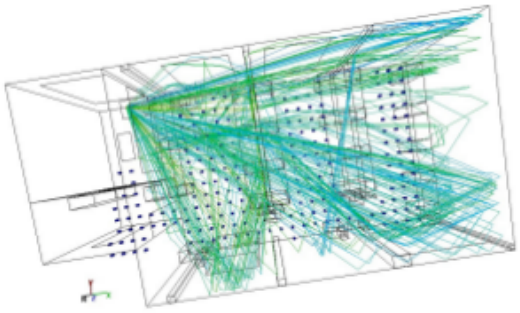

FIGURE 2.2: Ray Launching in an Indoor Environment

2.2.2 Model 2: Ray-Launching Based Deterministic Phase-shift Model for Massive MIMO

Deterministic Phase-shift model is a model based on modelling the MIMO channel through the array response of the receiver antenna array. The transmitter array and propagation mechanisms are modelled by the ray-launching model. For a receiver array, we can write the channel output in the time domain as:

$$h(t) = s(t) * r(t)$$

where $s(t)$ is the ray arriving at the receiver array and $r(t)$ is the array response. The symbol $*$ represents the convolution operation. The total channel effect is the convolution of the arriving rays at the receiver array. We can write this relationship in the frequency domain as:

$$\mathbf{H}(\omega) = \mathbf{R}'(\omega) \cdot \mathbf{S}(\omega) \tag{2.5}$$

where $\mathbf{H}(\omega)$ is the full channel matrix; $\mathbf{S}(\omega)$ is the group of rays arriving at the receiver array in a row vector and $\mathbf{R}(\omega)$ is the array response vector; $'$ denotes the matrix transpose. The vectors $\mathbf{R}$ and $\mathbf{S}$ are both row vectors.

The array response can be written in a row vector form as:

$$\mathbf{R}(\omega) = \begin{bmatrix} r_1(\omega)\mathrm{e}^{\frac{-2j\pi\Delta d_1}{\lambda}} & r_2(\omega)\mathrm{e}^{\frac{-2j\pi\Delta d_2}{\lambda}} & \cdots & r_r(\omega)\mathrm{e}^{\frac{-2j\pi\Delta d_r}{\lambda}} \end{bmatrix} \tag{2.6}$$

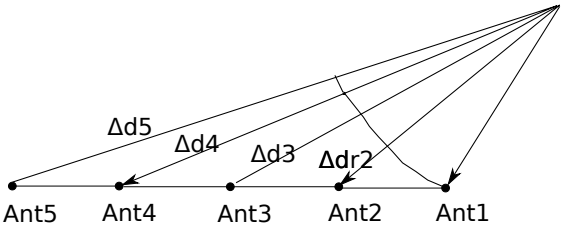

FIGURE 2.3: An Illustration of the Phase Shift Model in a Linear Array

where λ is the wavelength of the electromagnetic wave; r_r is the amplitude of the array response and Δd_r is the distance difference between the rth ray and the representative ray arriving at the reference point. Together with this vector, the equation in (2.5) characterises the matrix array response by modelling the complete channel matrix as the output of the receiver array. The relationship is illustrated in Figure 2.3.

On the other hand, the arriving group of rays can be written as:

$$\mathbf{S}(\omega) = \begin{bmatrix} s_1(\omega) & s_2(\omega) & \cdots & s_t(\omega) \end{bmatrix}$$

The matrix elements h_t are calculated by the ray-launching model in (2.3). In the direct ray-launching model, the matrix elements are calculated sequentially until the full channel matrix is completed. In application, we notice such a way of calculating each individual channel matrix element is cumbersome and unnecessary. We can approximate the group of arriving rays by using a single representative ray. If we choose the ray arriving at the array centre as the representative ray, the above matrix can be written as:

$$\mathbf{S}(\omega) = \begin{bmatrix} s_c(\omega) & s_c(\omega) & \cdots & s_c(\omega) \end{bmatrix}$$

where $s_c(\omega)$ is the ray arriving at the array center. Its exact value is determined by (2.3) through tracing along the propagating rays. In contrast to the model of calculating all the individual matrix elements in (2.4), this model significantly reduces the computational complexity. Combining this equation with (2.6) according to (2.5), we have the model for the MIMO channel matrix as in (2.7).

Although it is an approximation, we notice in most applications it has a satisfying degree of accuracy. We will compare the model with the measurement in Section

2.4.1. However, from the computational efficiency perspective, this model significantly reduces the computational complexity by reducing the repetitions of the ray-launching simulation to only once.

Here we derive the model for the receiver array used in the measurement using the above phase-shift model. Figure 2.4 shows a cylindrical antenna array with 4 rings of 16-element array mounted on the cylindrical surface. The radius of the cylinder is r_a and the distance between the rings is h_a. This cylindrical antenna array has been developed at the Communication Engineering Department of Lund University in Sweden. Various channel measurement has been carried out using this cylindrical antenna array [61]. We also had a channel measurement campaign at Lund University in 2010 using this array.

We can identify the distance differences by the geometric relationship. The distance difference has four possible values as in (2.8) and (2.9) for the two inner rings of elements; and as in (2.10) and (2.11) for the two outer rings of elements, where d_0 is the distance between the transmitter and the array centre in the horizontal plane; ϕ_i is the azimuth angle of the ith element with respect to the reference direction.

Thus, the array response vector is written as in (2.12). In this equation the array response can be uniformly divided into 4 parts corresponding to the 4 rings of elements. Each part contains a 16-element vector corresponding to the 16 elements in each ring. With the ray-launching model to feed the rays as the input, we can obtain the complete channel matrix.

A similar phase-shift model has also been used in MIMO channel modelling in [62]. However, using only a single ray to approximate the whole array has low accuracy, especially for modelling large array systems. Therefore, we can further choose more representative rays to model the large size array to improve accuracy. For example, in the cylindrical array in Figure 2.4, we can model the cylindrical array as 4 layers of 2D uniform circular array. Each consists of 16 antenna elements. Thus, instead of choosing

$$\mathbf{H}(\omega) = \begin{bmatrix} h_c(\omega)\mathrm{e}^{\frac{-2j\pi d_{1,1}}{\lambda}} & h_c(\omega)\mathrm{e}^{\frac{-2j\pi d_{1,2}}{\lambda}} & \cdots & h_c(\omega)\mathrm{e}^{\frac{-2j\pi d_{1,r}}{\lambda}} \\ h_c(\omega)\mathrm{e}^{\frac{-2j\pi d_{2,1}}{\lambda}} & h_c(\omega)\mathrm{e}^{\frac{-2j\pi d_{2,2}}{\lambda}} & \cdots & h_c(\omega)\mathrm{e}^{\frac{-2j\pi d_{2,r}}{\lambda}} \\ \vdots & \vdots & \ddots & \vdots \\ h_c(\omega)\mathrm{e}^{\frac{-2j\pi d_{t,1}}{\lambda}} & h_c(\omega)\mathrm{e}^{\frac{-2j\pi d_{t,2}}{\lambda}} & \cdots & h_c(\omega)\mathrm{e}^{\frac{-2j\pi d_{t,r}}{\lambda}} \end{bmatrix} \tag{2.7}$$

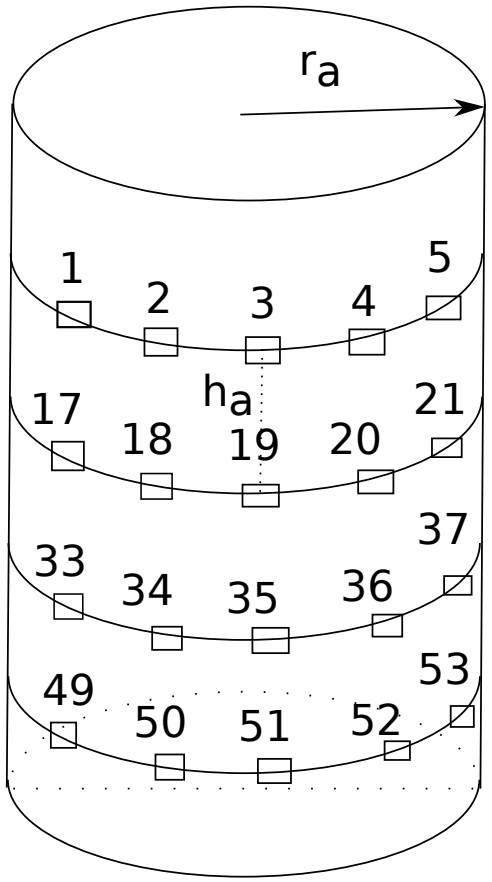

FIGURE 2.4: A Cylindrical Antenna Array

the cylindrical array centre as the reference point, we choose the centres of the 4 layers of the 2D circular array. We then have 4 rays to approximate the whole channel matrix.

$$\Delta d_1 = \sqrt{r_a^2 + d^2 + \frac{1}{4}h_a^2 - h_a\sqrt{d^2 - (d_0 + r_a)^2} - 2r(d_0 + r_a)\cos\phi_i} \tag{2.8}$$

$$\Delta d_2 = \sqrt{r_a^2 + d^2 + \frac{1}{4}h_a^2 + h_a\sqrt{d^2 - (d_0 + r_a)^2} - 2r(d_0 + r_a)\cos\phi_i} \tag{2.9}$$

$$\Delta d_3 = \sqrt{r_a^2 + d^2 + \frac{9}{4}h_a^2 - 3h_a\sqrt{d^2 - (d_0 + r_a)^2} - 2r(d_0 + r_a)\cos\phi_i} \tag{2.10}$$

$$\Delta d_4 = \sqrt{r_a^2 + d^2 + \frac{9}{4}h_a^2 + 3h_a\sqrt{d^2 - (d_0 + r_a)^2} - 2r(d_0 + r_a)\cos\phi_i} \tag{2.11}$$

$$\mathbf{R}(\omega) = \left[\mathrm{e}^{\frac{-2j\pi\Delta d_3}{\lambda}} \quad \cdots \quad \mathrm{e}^{\frac{-2j\pi\Delta d_1}{\lambda}} \quad \cdots \quad \mathrm{e}^{\frac{-2j\pi\Delta d_2}{\lambda}} \quad \cdots \quad \mathrm{e}^{\frac{-2j\pi\Delta d_4}{\lambda}} \quad \cdots\right] \tag{2.12}$$

In this case, the distance difference is given as:

$$\begin{aligned} \Delta d_i(p) &= \sqrt{r_a^2 + d^2(p) - 2r(d_0 + r_a)\cos\phi_i} - d_i(p) \\ \text{for } p &= \{1, 2, 3, 4\} \end{aligned} \tag{2.13}$$

where p is the 4 chosen rays; $d_i(p)$ is the distance between the transmitter and the reference points of the 4 rays. Then, the complete array response is given as in (2.14) with (2.13).

$$\mathbf{R}(\omega) = \left[e^{\frac{-2j\pi\Delta d_1(1)}{\lambda}} \quad \cdots \quad e^{\frac{-2j\pi\Delta d_{17}(2)}{\lambda}} \quad \cdots \quad e^{\frac{-2j\pi\Delta d_{33}(3)}{\lambda}} \quad \cdots \quad e^{\frac{-2j\pi\Delta d_{49}(4)}{\lambda}} \quad \cdots \right] \tag{2.14}$$

This model requires the ray-launching simulation of 4 rays. It compensates the accuracy by higher computational cost than the single ray model. We name this model as Model 2 in the following part of this chapter.

2.2.3 Model 3: Ray-Launching Based Probabilistic Model for Massive MIMO

Modelling the wireless channel as a probabilistic fading channel is another category of channel models in contrast to the deterministic channel models. It has the advantage of simplicity and efficiency when the physical model is prohibitively complex. In this part, we propose a probabilistic channel model for massive MIMO based on the ray-launching model. Considering the model specifically for the indoor scenario, we model the fading channel as a Rician distribution. The choice of Rician distribution is because it comprises a rich group of probability distributions: by determining various values for the Rician K factor, a group of statistical distributions is included. The ray-launching model supplies the multipath information to estimate the parameters for the Rician distribution. Furthermore, the channel measurement also indicates the channel elements follow a Rician distribution. A recent study to model the massive MIMO as a Rician distributed statistical model can be found in [63].

A single antenna Rician distributed channel can be written as:

$$h = \sqrt{k}h_d + \sqrt{1-k}h_s$$

where k is the K factor in Rician distribution; h_d is the direct path component and h_s is the scattering component.

We model the channel matrix element $H_{m,n}$ in (2.1) as a Rician distributed random variable:

$$H_{m,n} \sim Rice(v, \sigma)$$

where v and σ are the parameters to determine the Rician distribution. The probability distribution function of the Rician distribution is given as:

$$f(x|v, \sigma) = \frac{x}{\sigma^2} \left(\frac{-(x^2 + \sigma^2)}{2\sigma^2} \right) I_0 \left(\frac{xv}{\sigma^2} \right)$$

where $I_0(\cdot)$ is the modified Bessel function of the first kind with order zero. In order to obtain the exact distribution function, we need to estimate the two parameters v and σ. We will resort to the ray-launching model to estimate these two parameters.

The ray-launching model traces a group of rays equivalent to the multipath components. This multipath information can be used to estimate the parameters of the Rician distribution. Below we adopt the method from the work of [64] to estimate the Rician distribution parameters.

The rays are modelled as equivalent to the multipath components in (2.3). From this model, we have the values of the ray field A_α along each ray. We can use this multipath information to estimate the parameters v and σ as shown below.

According to [64] the k-factor can be estimated as:

$$k = \frac{\sqrt{1 - r}}{1 - \sqrt{1 - r}}$$

The quantity r is given as:

$$r = \frac{V[A_\alpha^2]}{(E[A_\alpha^2])^2}$$

where $V[A^2]$ is the variance of A^2.

After obtaining the k-factor, the Rician distribution parameters v and σ can be calculated from:

$$v^2 = \frac{k}{1 + k} \Omega$$

$$\sigma^2 = \frac{1}{2(1+k)}\Omega$$

where $\Omega = E[A_\alpha^2]$ is the expected value of the A_α^2. Thus, we obtain the two parameters v and σ.

Then we can write the MIMO channel matrix as in (2.15), where $v_{t,r}$ is the v parameter estimated between the r-th receiver and the t-th transmitter.

This probabilistic MIMO model requires the calculation of v and σ parameters for each channel matrix element. Such a statistical model still requires the input from the deterministic ray-launching model. However, it has the advantage of flexibility in real application since the only parameters required are the parameters for the probability distributions. Moreover, the calculation is in the same manner to repeat the calculation until all the matrix elements are computed. However, such a process costs highly in simulation. We can further simplify the calculation process in the following part.

2.2.4 Model 4: Simplified Ray-Launching Based Probabilistic Model for Massive MIMO

Similar to the simplified deterministic model for massive MIMO channel, we can choose one representative point to approximate the whole antenna array. Although such an approximation sacrifices certain accuracy, it significantly reduces the computational cost by decreasing the repetition of ray-launching model simulation to only once.

Here again we choose the array center as the representative point to calculate the probability distribution parameter v and σ for the whole channel matrix. Thus, the channel matrix is written as in (2.16), where v_c and σ_c are parameters estimated using the rays between the transmitters and the center of the receiver array. Like the simplified deterministic model, this model shows adequate accuracy in many applications. We

$$\mathbf{H} = \begin{bmatrix} H_{1,1} \sim Rice(v_{1,1}, \sigma_{1,1}^2) & H_{1,1} \sim Rice(v_{1,2}, \sigma_{1,2}^2) & \cdots & H_{1,r} \sim Rice(v_{1,r}, \sigma_{1,r}^2) \\ H_{2,1} \sim Rice(v_{2,1}, \sigma_{2,1}^2) & H_{2,2} \sim Rice(v_{2,2}, \sigma_{2,2}^2) & \cdots & H_{2,r} \sim Rice(v_{2,r}, \sigma_{2,r}^2) \\ \vdots & \vdots & \ddots & \vdots \\ H_{t,1} \sim Rice(v_{t,1}, \sigma_{t,1}^2) & H_{t,2} \sim Rice(v_{t,1}, \sigma_{t,1}^2) & \cdots & H_{t,r} \sim Rice(v_{t,r}, \sigma_{t,r}^2) \end{bmatrix} \quad (2.15)$$

will show the comparison result between this model and the measurement in Section 2.4.1.

2.3 Measurement Campaigns

Small cell and heterogeneous wireless networks, such as femtocell and wireless local area network (WLAN), are the major networks to be deployed for the next generation wireless networks. These small networks are mainly deployed in indoor environments as a complement to the larger cell networks, to deploy heterogeneous networks. The measurements are carried out in indoor environments. They are typical small cell wireless network deployment scenarios. Equipped with massive MIMO antenna arrays, they are interesting scenarios for studying the performance of next generation wireless networks with massive MIMO channels.

We have carried out two measurement campaigns for the small cell networks: downlink and uplink scenarios. We give the details of the channel measurements in the following parts of this section.

2.3.1 Measurement of Downlink Channel

The downlink channel is measured in an indoor office environment. The measurement site is in the E-Huset of Lund University, in Ole Rmers vg 3, Lund in Sweden. Figure 2.5 shows a map of the building.

The antenna array at the transmitter is a flat panel antenna array with 64 dual-polarised patch antenna elements. The left side of Figure 2.9 shows a photo of the transmitter array. The receiver array is a cylindrical array with 64 dual-polarised patch antenna elements. The right side of Figure 2.9 shows a photo of the receiver array. These antenna arrays are both with 64 antenna elements. They are typical massive MIMO antenna

$$\mathbf{H} = \begin{bmatrix} H_{1,1} \sim Rice(v_c, \sigma_c^2) & H_{1,1} \sim Rice(v_c, \sigma_c^2) & \cdots & H_{1,r} \sim Rice(v_c, \sigma_c^2) \\ H_{2,1} \sim Rice(v_c, \sigma_c^2) & H_{2,2} \sim Rice(v_c, \sigma_c^2) & \cdots & H_{2,r} \sim Rice(v_c, \sigma_c^2) \\ \vdots & \vdots & \ddots & \vdots \\ H_{t,1} \sim Rice(v_c, \sigma_c^2) & H_{t,2} \sim Rice(v_c, \sigma_c^2) & \cdots & H_{t,r} \sim Rice(v_c, \sigma_c^2) \end{bmatrix} \tag{2.16}$$

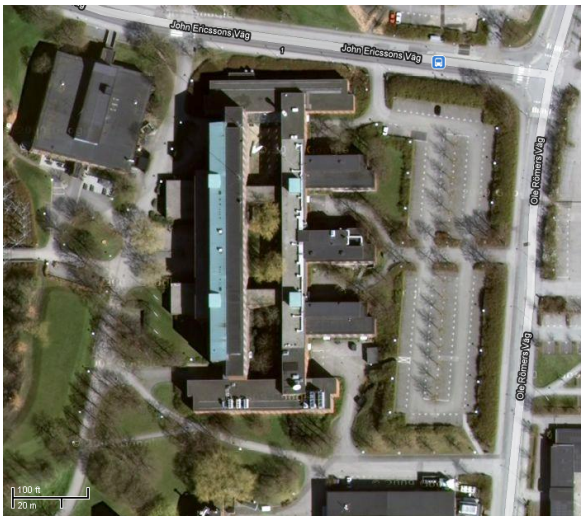

FIGURE 2.5: The E-Huset building of Lund Institute of Technology and its surrounding areas

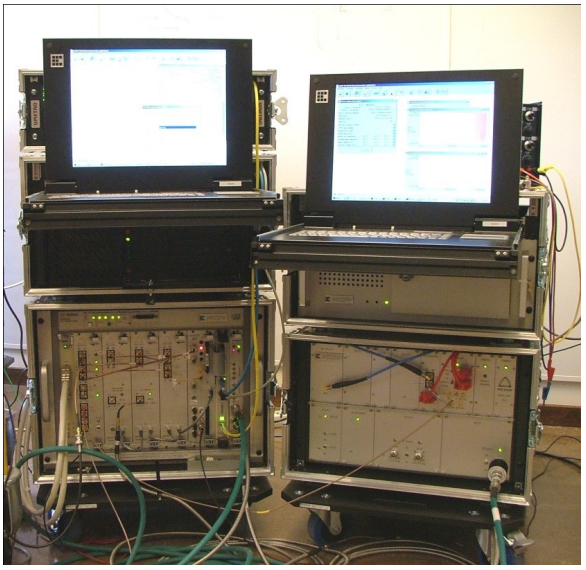

FIGURE 2.6: The RUSK Lund Channel Sounder

arrays. The antenna arrays are built by the Department of Electrical Engineering of Lund University in Sweden.

We choose to use these antenna arrays to carry out the measurement campaign to study the performance of massive MIMO channel. The frequency of the channel measurement is 2.6 GHz. The transmitter power is set to be 20 dBm to 40 dBm depending on the location. The RUSK channel sounder used in the measurement is shown in Figure 2.6. The measurement campaign was carried out in the summer of 2010. More details of the measurement campaign can be found in the works[61, 65]. An internal technical report on this measurement campaign is also available upon request [66].

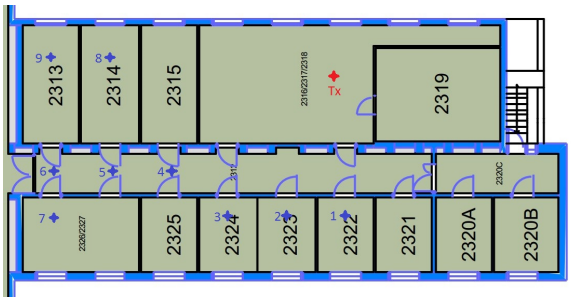

FIGURE 2.7: Building Floor Map of the Downlink Scenario and Channel Measurement Locations

The measurements have been carried out in the rooms in the building in Figure 2.5. Figure 2.7 shows a building floor map. The transmitter is fixed at the location T_x. The receivers are moved from location 1 to location 9. This is a typical downlink scenario in indoor small cell networks. We measure the channel matrices at the 9 locations marked in the map.

2.3.2 Measurement of Uplink Channel

The channel measurement for uplink scenario is carried out in the Department of Engineering and Computing Science, Durham University, UK. The measurement environment is in the Department of Computer Science of Durham University. The Durham Channel Sounder was used to carry out the channel measurement. The measurement environment and the channel sounder has also been used to measure MIMO channel with small number of antennas in the work of [67]. The information of a similar but updated channel sounder specifically for 60 GHz can be found in [68]. The measurement campaign was carried out in the Autumn of 2013. Figure 2.8 shows a map of the building floor.

The transmitter antenna array is a 32-element antenna array with 4 layers of 8-element uniform linear arrays. Each antenna element has an omnidirectional radiation pattern. The receiver antenna array has a similar structure with 4 layers of 6-element uniform linear arrays.

The measurement scenario is shown as the building map in Figure 2.8. The receiver is fixed at the location R_x. The transmitter is moved from location 1 to location 8. The frequency of of the channel measurement is 2.4 GHz. This is a typical uplink scenario

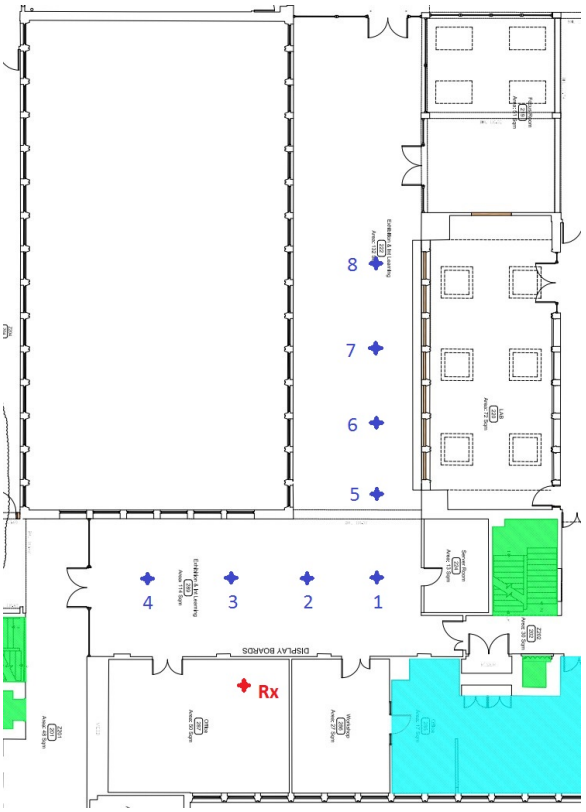

FIGURE 2.8: Building Floor Map of the Uplink Scenario and Channel Measurement Locations

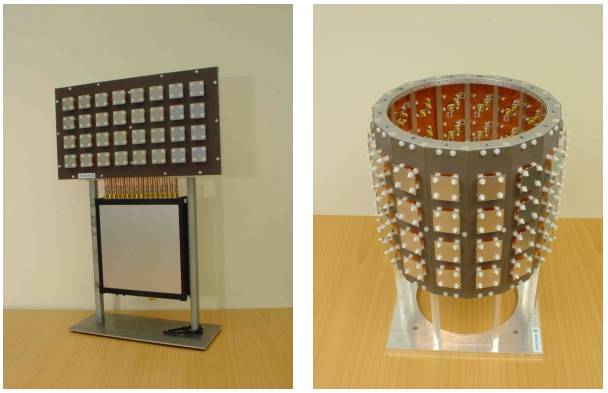

FIGURE 2.9: Transmitter Antenna Array (right) and Receiver Antenna Array (left)

in the indoor small cell networks. We measure the channel matrix at the 8 locations marked in the map.

2.4 Measurement and Simulation Comparison and Analysis

2.4.1 Computational Efficiency

In this section, first we present the computation time of the 4 models given in Section 2.2.1, using them to simulate the downlink and uplink scenarios. Table 2.1 shows the computation time the 4 models take to simulate the downlink scenario and uplink scenario. We use the ray launching simulation package from the work of [26] to simulate the ray launching. We adopt the same simulation setting as in the work of [59]. The simulation resolution is set to be 0.1 metre. We can see for a massive MIMO system the calculation of MIMO matrices for a typical indoor environment can take several hours. In our simulation Model 1 and Model 3 take about 5 hours to simulate the whole environment. The results also show that Model 2 and Model 4 use a significantly less amount of time than Model 1 and Model 3. This is due to the lower computational complexity of both Model 2 and Model 4. Model 1 and Model 3 both calculate each individual channel matrix element via ray-launching, while Model 2 and Model 4 reduce the times of repetition for ray-launching simulation. The computational cost in the simulation is mainly due to the ray-launching simulation. The computation time is linear in the repetition of the ray-launching simulation. For Model 4 the ray-launching algorithm only simulates once; Model 2 simulates 4 times; Model 1 and Model 3 both simulate 32 times. The computation time listed in Table 2.1 agrees with this analysis. The computation time of the four models shown in the table suggests that for time demanding tasks in network planning and optimisation applications, both the simplified models Model 2 and Model 4 are better choices because of less time needed for simulation.

	Downlink	Uplink
Model 1 Computation Time	302 min 56 sec	278 min 24 sec
Model 2 Computation Time	36 min 27 sec	32 min 28 sec
Model 3 Computation Time	308 min 43 sec	281 min 25 sec
Model 4 Computation Time	9 min 29 sec	8 min 30 sec

TABLE 2.1: Computation time of the models

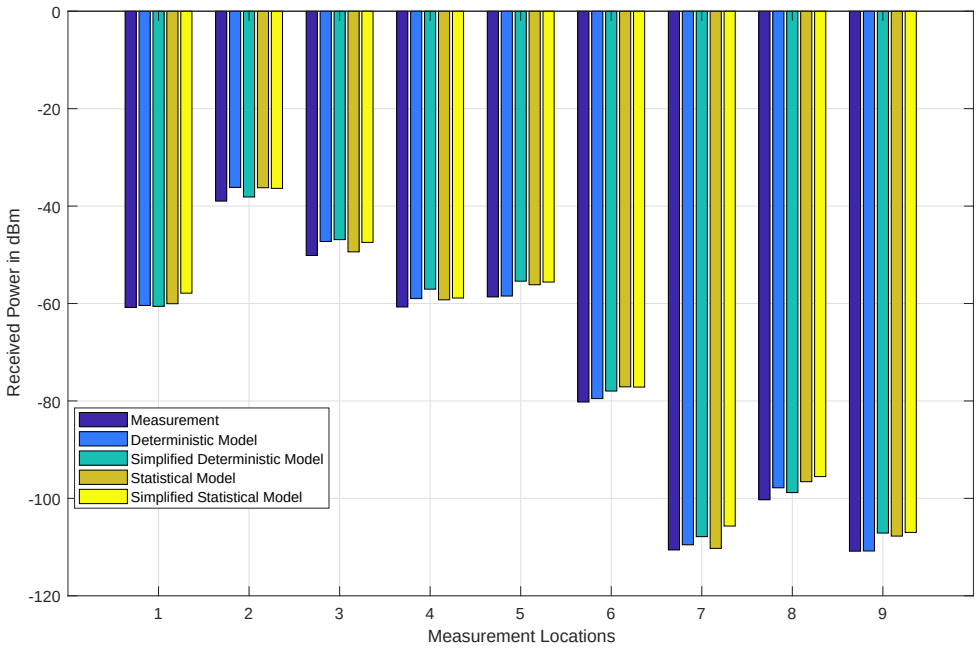

FIGURE 2.10: Average Received Power in Downlink

2.4.2 Received signal power

The received signal power is one of the most important parameters in network deployment and optimisation. It is closely related to the performance of the wireless networks. According to (2.3) the received power at a certain location is calculated as

$$P(x,y,z) = \| \sum_{\alpha=1}^{q} A_\alpha(x,y,z) \mathrm{e}^{-j\omega\tau_\alpha(x,y,z)} \|^2$$

Figure 2.10 shows the comparison between the average received power of the measurements and the simulation results in the downlink scenario. Figure 2.11 shows the same comparison result in the uplink scenario. We can see both results show good agreement.

The error between the simulation and measurements is calculated by the Root Mean Square (RMS) error as:

$$E = \frac{1}{rt} \sum_{m=1,n=1}^{m=r,n=t} \sqrt{H_{m,n}^2 - \hat{H}_{m,n}^2}$$

where $\hat{H}_{m,n}$ is the simulated channel matrix.

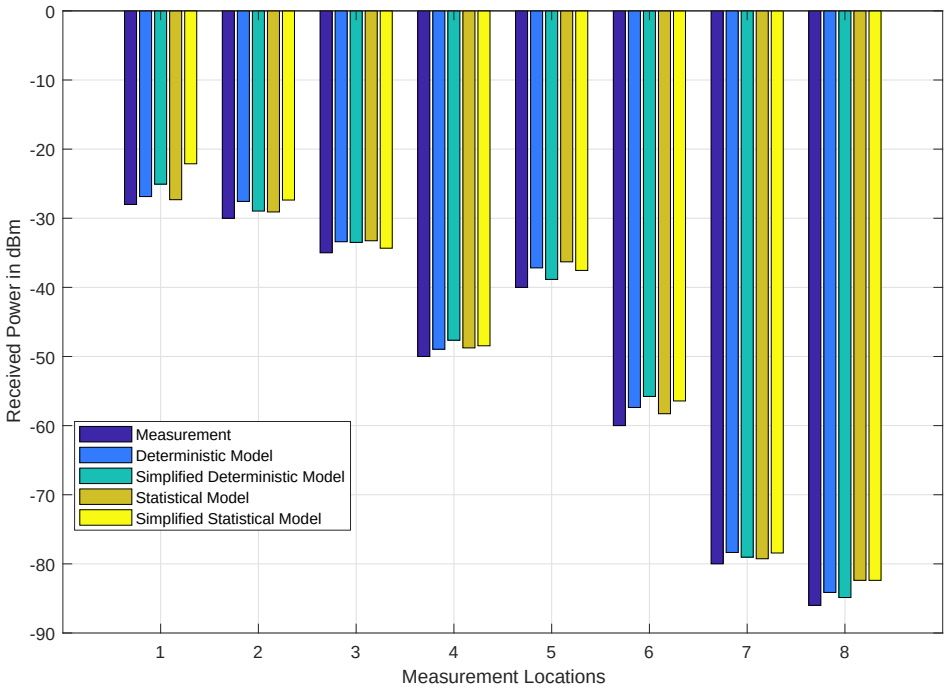

FIGURE 2.11: Average Received Power in Uplink

Following the above equation, we use the simulated channel $\hat{H}_{m,n}$ and the measured channel $H_{m,n}$ to calculate the RMS errors of the simulation models. The RMS error results are presented in Table 2.2 and Table 2.3.

The results show that the RMS errors of Model 1 and Model 3 are smaller. The RMS errors of Model 2 and Model 4 are higher but still mostly under 6 dB. This shows the accuracy of Model 1 and Model 3 is higher than that of Model 2 and Model 4. This is

Location	1	2	3	4	5	6	7	8	9
Model 1 RMS Error	3.2301	3.0285	3.4619	2.7061	3.1657	5.3280	2.3195	4.7964	3.3340
Model 2 RMS Error	3.7594	5.4562	5.4561	5.0356	5.8612	5.7495	5.8634	5.6547	5.5598
Model 3 RMS Error	4.7565	4.9863	4.8322	4.9879	4.1897	5.7882	4.6671	4.9882	4.3375
Model 4 RMS Error	5.9781	5.3245	5.4215	5.7145	5.8771	5.8873	5.3227	5.9551	5.7723

TABLE 2.2: RMS Error in Downlink Scenario

Location	1	2	3	4	5	6	7	8
Model 1 RMS Error	2.9568	2.2584	3.6514	3.9184	2.3808	2.3101	2.8085	2.2751
Model 2 RMS Error	5.8631	5.7761	4.3343	5.4475	5.2403	5.9712	5.3315	5.9882
Model 3 RMS Error	4.7701	4.2321	4.5642	5.4241	4.0214	4.0859	4.8794	4.9583
Model 4 RMS Error	5.4578	5.3762	5.4772	5.6549	5.6873	5.0857	5.7544	5.7563

TABLE 2.3: RMS Error in Uplink Scenario

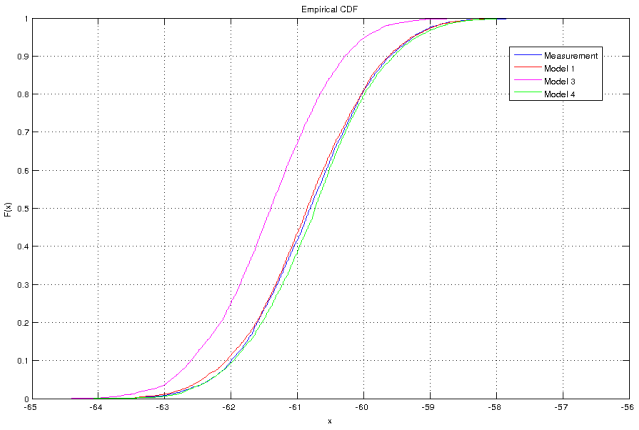

FIGURE 2.12: Distribution of Received Power of Channel Elements in Downlink

because both Model 2 and Model 4 simplify the computation by using a single ray to represent the whole array. The two simplified models trade certain degree of accuracy for computational efficiency. However, the result shows that the overall accuracy of the ray-launching models for massive MIMO systems is satisfying for the network planning and optimisation purpose.

2.4.3 Distribution of Channel Elements

Massive MIMO channels are in a form of large channel matrix. The primary modelling target for massive MIMO is to model the large channel matrices. We have 4 models to generate the channel matrices according to (2.4). In this section, we choose the measurement location 5 in the downlink scenario and measurement location 6 in the uplink scenario to show the empirical distribution of the simulated channel elements.

In Figure 2.12 we present the cumulative distribution function (CDF) of the simulated channel matrix elements of the downlink scenario in comparison with the measurement. Model 2 is not included in this simulation as the power distribution of Model 2 is determined by the choices of the rays. We can see the simulated channel matrix elements have a very close distribution to the measured channel matrix elements. This demonstrates a good agreement between the simulation model and the measurement.

The uplink scenario result in Figure 2.13 shows a similar pattern as in the downlink scenario. The above results demonstrate that the simulation models generate channel matrix elements in good agreement with the measurement.

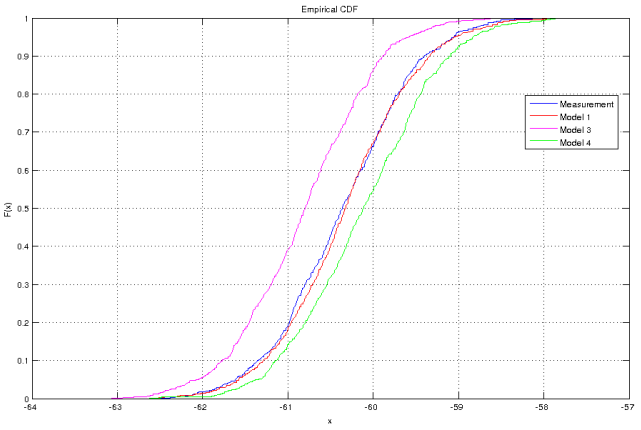

FIGURE 2.13: Distribution of Received Power of Channel Elements in Uplink

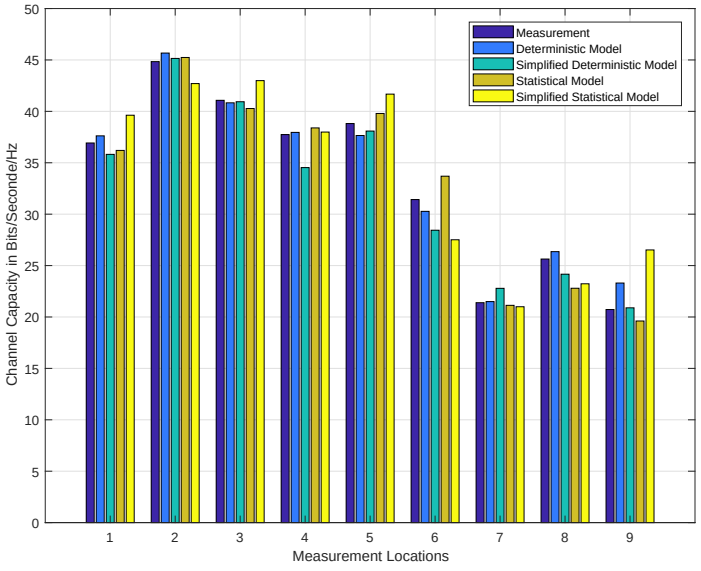

FIGURE 2.14: Channel Capacity in Downlink

2.4.4 Channel Capacity Results

Channel capacity gain is one of the most attractive features of the massive MIMO channel promised to the future wireless networks. In this part of the result, we present the channel capacity comparison between the simulated channels and the measurement.

The MIMO channel capacity is calculated according to the equation:

$$C = \log \det \left(\mathbf{I} + \frac{1}{N_0} \mathbf{H}\mathbf{H}^* \right)$$

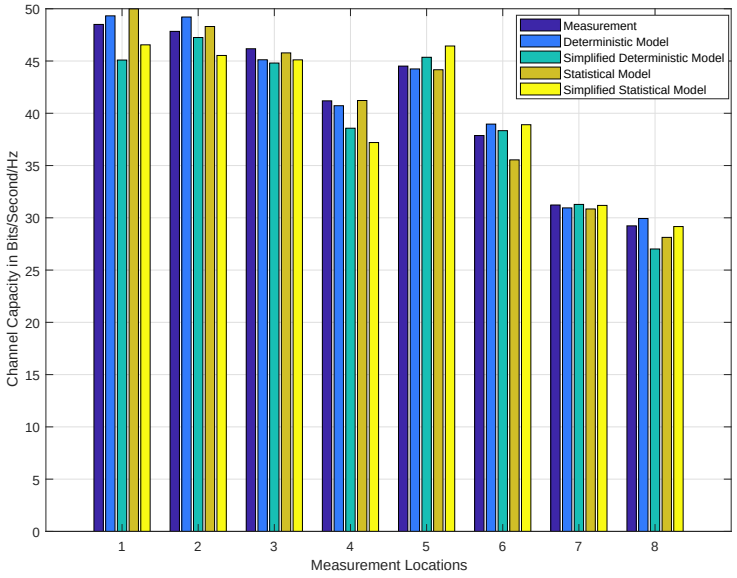

FIGURE 2.15: Channel Capacity in Uplink

We apply the above MIMO channel capacity formula to calculate the MIMO channel capacity from both the simulated channel matrices and the measured channel matrices. Figure 2.14 shows the capacity result comparison in the downlink scenario. Figure 2.15 shows the capacity result comparison in the uplink scenario. Both figures show a good agreement in the channel capacity between the simulated results and the measurement. This demonstrates that the simulation models are accurate in estimating the channel capacity. Therefore, the simulation models provide a reliable way to predict the channel capacity in network planning and optimisation.

2.5 Conclusion

In this work, we propose to use ray launching model in massive MIMO channel modelling in indoor environments. In order to limit the computational complexity in massive MIMO channels in network optimisation, we developed 4 ray-launching based simulation models for modelling massive MIMO channel. The primary application of these models is network planning and optimisation. We compare these simulation models with the measurement in two real small cell network deployment environments. The comparison results show that the models have good agreements with the measurement. Therefore, these 4 ray-launching based simulation models are efficient

and accurate models, for planning and optimising networks equipped with massive MIMO arrays.

The main contribution of this chapter is the 4 simplified modelling methods to tackle the high computational complexity challenge in massive MIMO channels. These methods reduced the complexity by exploiting the physical characteristics of the channel and the propagation environments. Therefore, our results suggested that by incorporating the physical characteristics of propagation channels, complexity and redundancy in the computational models for massive MIMO can be avoided.

Chapter 3

Ray Launching based mmWave Channel Modelling for Indoor Propagation

3.1 Introduction

Wireless network planning and optimisation is a key component in network deployment. To meet the demand of optimal network services with minimal resource and cost, network planning plays a key role in the deployment of the networks. Channel map is one of the key tools that are essential in the planning and optimisation of the networks geographically. The channel map is to indicate the channel characteristics over the geographic map of the network deployment space. A channel map is used as an essential tool to describe the channel condition geographically and then facilitates the network deployment in the design space.

Channel maps are widely constructed through computer simulation based electromagnetic propagation predication tools. One of the popular models to simulate the electromagnetic propagation is based on ray tracing. The early work in [9] first introduced the simulation based channel predication software tools WiSE. It is based on the electromagnetic propagation principles of geometrical optics (GO) and Uniform Theory of Diffraction (UTD). The software CINDOOR [10] is based on the same physical propagation simulation and is specifically designed for indoor environment. The work

in [69] extended the work to include diffusive diffraction in ray tracing. The recent work in [70] also applied the ray tracing simulation to construct MIMO channels.

Another method is based on the numerical solution of the wave propagation equation and Maxwell's equations. The finite-difference time domain (FDTD) method gives a numerical solution to the electromagnetic field in the time domain. Following the FDTD algorithm, the work in [12] proposed a finite element based numerical method to build a channel map efficiently.

The millimetre wave (mmWave) channel is proposed as a promising technique for the future wireless networks. The channel has many unique characteristics. To deploy networks equipped with mmWave channels, a channel map construction tool that is capable of building mmWave channel map is essential. However, such a tool is still missing. In this chapter, we propose a simulation based channel map construction tool based on an intelligent ray launching algorithm (IRLA) [26], especially for modelling the path loss value of 60 GHz indoor channel. It exploits the characteristics of the mmWave channels to simplify the computational complexity of the traditional simulation tools, while still preserves high degree of accuracy of the original physical electromagnetic propagation models. The simulation model is then verified by the measurement result in a real propagation environment.

The rest of the chapter is organised as follows. Section 3.2 describes the new ray tracing based model. Section 3.4 is the comparison and analysis of simulation. Section 3.5 is the conclusion.

3.2 The Path Loss Model based on Ray Launching

A widely used path loss model is the empirical model of log distance model. The model is simply given as

$$PL(d) = PL(d_0) + 10\gamma \log_{10}(\frac{d}{d_0}) \tag{3.1}$$

where $PL(d)$ is the path loss value at the distance d; $PL(d_0)$ is the path loss value at the reference distance d_0; γ is the path loss exponent. The path between the transmitter and receiver can be seen as the sole propagation path chosen in the model. Hence, the

model can be seen as a single propagation path model. It is an empirical model widely used in modelling the path loss of propagation channel [71].

Wireless channel is widely modelled as multipath propagation. In multipath propagation model, the channel is written as

$$H(d) = \sum_{i=1}^{n} a_i \exp(-j\theta_i(d_i)) \tag{3.2}$$

where $H(d)$ is the channel impulse response at distance d; i is the multipath index; n is the number of the multipath components;d_i is the propagation distance of the i-th multipath component; a_i and θ_i are the amplitude and phase of the i-th multipath component, respectively. For calculating the path loss value of the channel from the multipath propagation model, we have the path loss value at d as

$$PL(d)_{mp} = -\log_{10} |H(d)|^2 \tag{3.3}$$

In traditional ray tracing algorithms, the path loss value is calculated according to (3.3). The value of the total channel effect $H(d)$ in multipath propagation is characterised through tracing the individual propagation paths. It is realised in GO and UTD [60]. However, the simulation of GO and UTD is computationally heavy. For the purpose of calculating the path loss value, we can adopt the simple log distance model in (3.1).

In our model, we calculate the path loss value of each individual multipath component via the ray launching simulation. Thus the path loss value becomes:

$$PL(d)_{mpe} = \frac{1}{n} \sum_{1}^{n} pl(d_i) \tag{3.4}$$

where $PL(d)_{mpe}$ is the path loss value at distance d; $PL(d_i)$ is the path loss value of the i-th multipath component. In appearance, the model in (3.4) differs from the model in (3.3). However, next we will show that the model in (3.4) is adequately accurate in comparison to the model in (3.3).

With a fixed distance d, we write the path loss value in (3.4) as

$$PL_{mpe} = \frac{-\sum_{i=1}^{n} 10 \log_{10} |a_i|^2}{n} \tag{3.5}$$

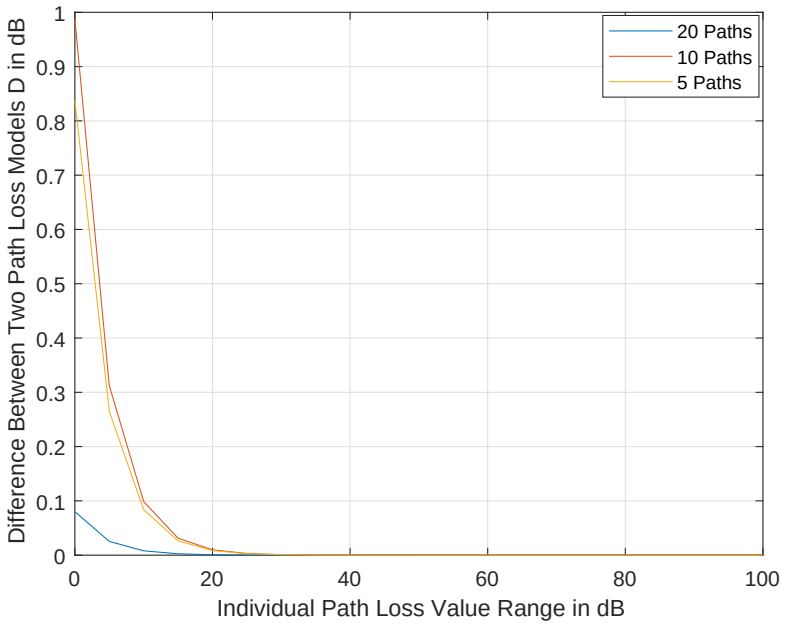

FIGURE 3.1: Path Loss Calculation Difference Using Sum-and-Average

and the path loss value from multipath propagation (3.3) as

$$PL_{mp} = -10\log_{10}|\sum_{i=1}^{n} a_i \exp(-j\theta_i)|^2 \tag{3.6}$$

We define the difference between the two path loss values as D in the equation below, and it has the unit in dB.

$$D = |PL_{mpe} - PL_{mp}| \tag{3.7}$$

In Figure 3.1, the value D is plotted against the loss value of the individual paths. The difference between the two models becomes negligible in the high path loss region. When the path loss values fall in the region above 20 dB, the difference is negligible. In this region, the path loss value calculated by (3.4) is a good approximation of the original multipath model.

This result shows that the model in (3.4) is adequately accurate in modelling the path loss values for channels in the path loss value region above 20 dB. To consider the realistic application of the model in network planning, the poor coverage where the path loss is high, is more to the interests of the network planning. Therefore the model offers a reasonable approximation to the original multipath propagation model. We can draw the following observation:

Proposition 3.1. *When the path loss values are in the region of larger than* 20*dB, the model in (3.4) is a good approximation to the model in (3.3).*

The model in (3.4) calculates the path loss value of each individual multipath and average the values. The advantage is that the calculation avoids the complexity of modelling the environment for the GO and UTD and still considering the multipath propagation mechanism of the wireless channel. By focusing on the path loss values, the computation can be significantly simplified without considering the GO and UTD. The drawback is that it is only suitable as an approximate model for the path loss values.

In the 60 GHz frequency band, the advantage of the model is even more obvious. The high path loss exponent of the 60 GHz frequency makes the high path loss region significantly smaller. In path loss channel map construction, the model has higher accuracy in even the vicinity regions of the network planning region.

The value of D against the distance is plotted in Figure 3.2. The figure shows that over the propagation distance of 0.1 metre, the difference between the two models is below 0.025 dB. With the increase of the propagation distance, the difference drops quickly. When the propagation distance is over 0.5 metre, the difference is negligible. This result shows that the 60 GHz frequency band has significantly reduced the suitable distance of adopting the model in (3.4).

For 60 GHz band indoor channels, we simplify the model in (3.4) by omitting the diffraction in the propagation. Thus the empirical path loss in the propagation calculation only considers the reflection and transmission in the propagation. The comparison between the simulation results and measurement in Section 3.5 shows this is an acceptable approximation in indoor path loss prediction.

The path loss of the reflected path is given as:

$$PL_{rf} = PL(d) - 10\log_{10}|\Gamma^2| \tag{3.8}$$

where $PL(d)$ is the empirical path loss values through the distance d; Γ is the Fresnel reflection coefficient.

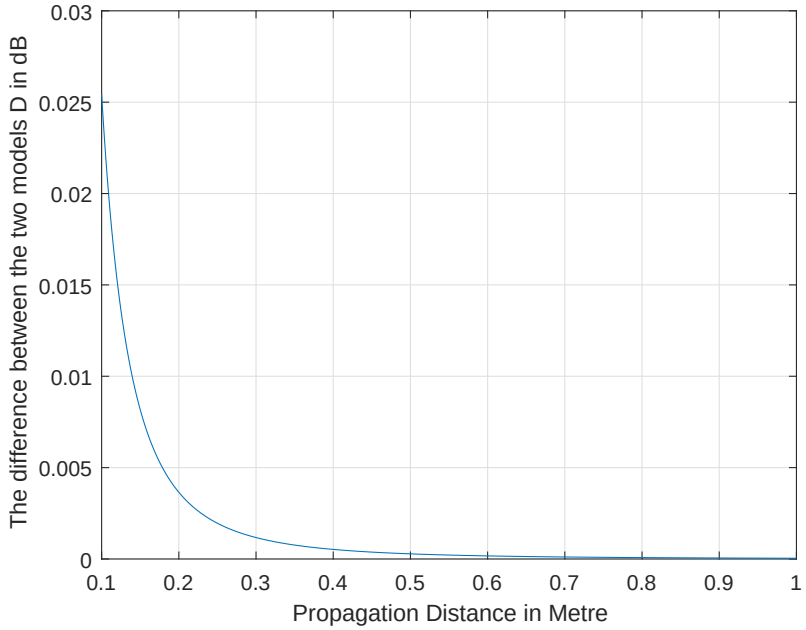

FIGURE 3.2: The Value of D vs the Propagation Distance

And the path loss value for transmission is given as:

$$PL_{tr} = PL(d) - 10\log_{10}|1 - \Gamma^2| \tag{3.9}$$

We use the three single loss values in (3.1), (3.8) and (3.9) to calculate the path loss value in each multipath component. Thus the total path loss of an individual path is written as:

$$PL_i = PL(d) + PL_{rf} + PL_{tr} \tag{3.10}$$

The path loss exponent value in (3.10) is chosen as $\gamma = 2.2$ for an indoor office environment with 60 GHz according to [71]. To trace the multipath propagation in the environment, we adopt an intelligent ray launching algorithm (IRLA) from [26]. The reflection coefficient values for various materials at 60 GHz in indoor office environments are taken from the work in [72]. The individual path loss values from the multipath components are then used to obtain the total path loss values. Following the model in (3.4), the path loss value now can be written as:

$$PL_{sa} = \frac{1}{n}\sum_{i}^{n} PL_i \tag{3.11}$$

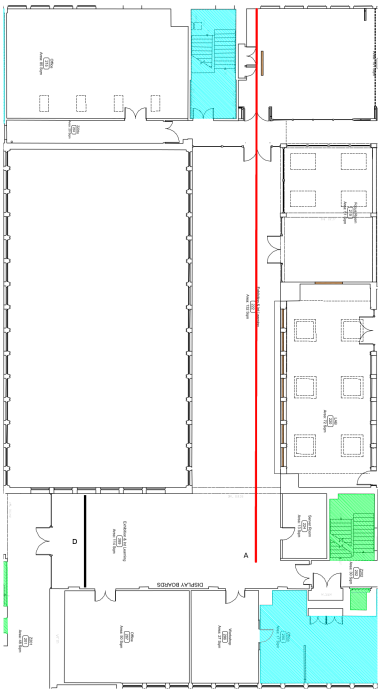

FIGURE 3.3: Buidling Floor Map

where PL_i is given in (3.10) and n is the total number of the chosen paths.

3.3 Channel Measurement

In this section, we briefly describe the channel measurement settings. The measurement environment is a typical office environment in the Department of Engineering at Durham University. The floor map is shown as in Figure 3.3. The floor is carpeted. The doors are wooden. The windows contain metal frames. The walls are bricks with plastered outer layer. There are some inner walls and doors are replaced by glass. The ceiling is made of plastic material. An overview of the measurement environment is shown in Figure 3.3.

The channel information is measured using the Durham channel sounder. The transmitter antennas and the receiver antennas are horn antennas. More detailed information about the channel sounder can be found in the work of [68]. Both the transmitter and the receiver are equipped with 2 antennas. The height of the transmitter is 2.35 metre. The height of the receiver is 1.46 metre. The centre frequency of the measurement is

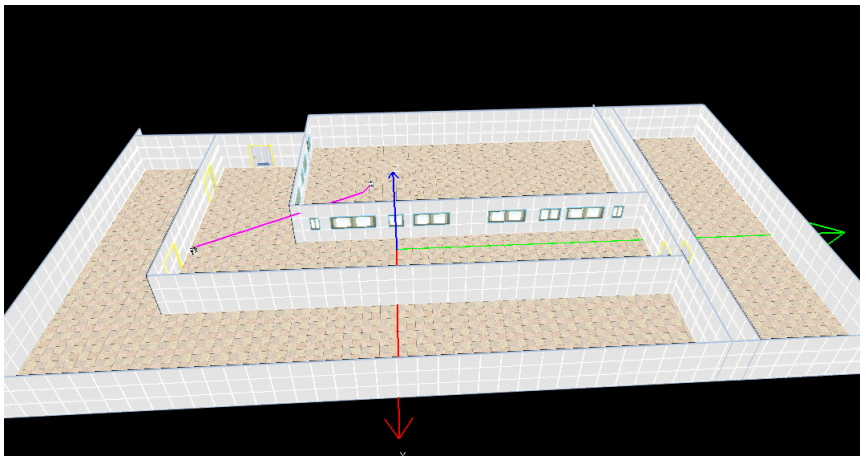

FIGURE 3.4: 3D Buidling Model

60 GHz. The measurement campaign was carried out in the Department of Computer Science of Durham University in the spring of 2014.

After the channel sounder was calibrated, the measurement was carried in the environment with the transmitter fixed. The location of the transmitter is indicated in Figure 3.3 as point 'A'. The height of the transmitter is fixed at the ceiling to emulate the typical placement of an indoor wireless network access point. Various receiver locations are chosen. The receiver locations are drawn along the red line in Figure 3.3 with various distances specified. The channel sounder data are recorded and processed. The path loss value at each measurement location is averaged over the 2 transmitter antennas and 2 receiver antennas. Thus, each measurement location has only one averaged path loss value.

3.4 Simulation Results and Comparison

The simulation is carried out using the path loss model in (3.4) based on the (IRLA) algorithm in[26]. The environment is modelled in a 3D building structure. The indoor environment is included in the model. The walls, doors, and windows are all included in the 3D building model. The 3D building model is shown in Figure 3.4. The simulation result of the path loss is shown in Figure 3.5. A 2D view of the path loss map is shown in Figure 3.6.

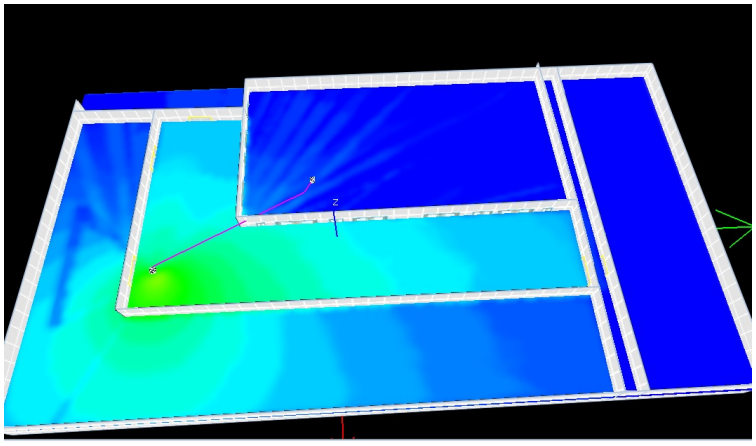

FIGURE 3.5: 3D Path Loss Simulation Result

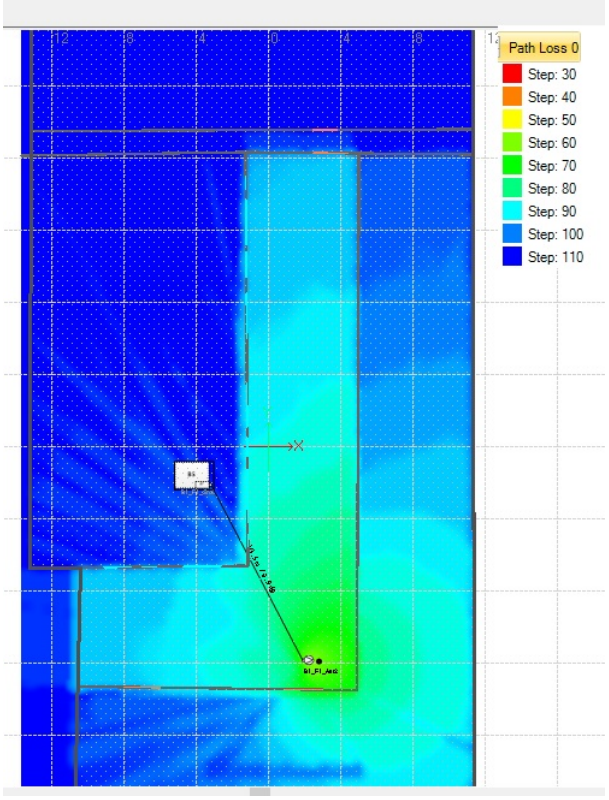

FIGURE 3.6: 2D Path Loss Simulation Result

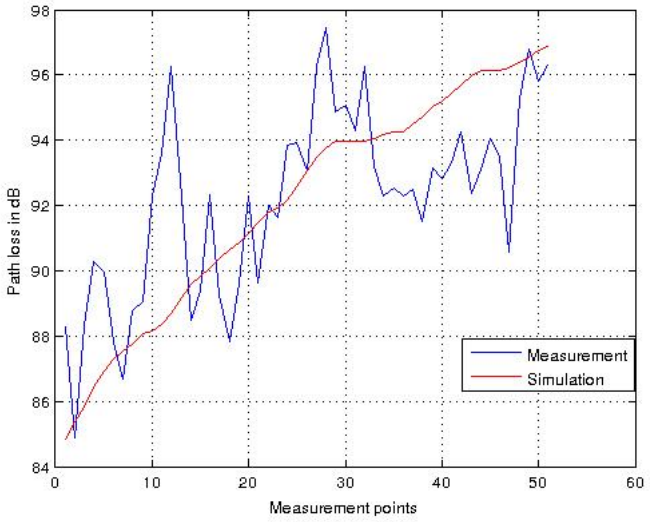

FIGURE 3.7: Path Loss Value Comparison

The comparison between the simulation and the measurement result is shown in Figure 3.7. The measurement locations are chosen along the red straight line in the map. In total 50 measurement locations are chosen. The simulation is set to 0.2m resolution.

In Figure 3.7, the red curve is the simulation results. The blue curve is the measurement result. The simulation result gives a good overall prediction of the path loss in the scenario. In most measurement locations, the error is below 3 dB. The overall Root Mean Square (RMS) error is 2.5028 dB. This demonstrates the simulation gives a good prediction to the path loss values in the environment.

3.5 Conclusion

In this chapter, first we analysed the modelling difference between the traditional multipath propagation model in (3.3) and an averaged path loss value model in (3.4). My analytical result showed that when the path loss values are high, the difference between the models is negligible. Based on this observation, I propose a path loss model for the 60 GHz indoor channel using the model in (3.4). The path loss model is an implementation of multipath empirical path loss model based on ray launching algorithm. The simulation model result is also compared with the measurement data in a typical indoor office scenario. Comparison between the simulation results and the measurement

demonstrates that the proposed model is an accurate model for indoor channel path loss prediction in the 60 GHz band.

The main contribution of this chapter is a new path loss model based on ray launching for mmWave frequency channel. By exploiting the characteristic of high attenuation of the mmWave channel, an efficient computational ray based path loss model is developed in this chapter. The results of this channel model suggest that channel models for the mmWave frequency can benefit from exploiting the unique characteristics of the channel at this frequency range.

Chapter 4

A Vector MIMO Channel Map Construction and Its Applications

4.1 Introduction

With the increasing demand for higher data rate communication, wireless network operators are facing the challenge of providing high quality network service. Network planning planning plays a central role in meeting the ever increasing demand for high data rate wireless communication. The purpose of network planning is to deploy the network nodes in optimal locations to provide guaranteed quality of network service. In conventional network planning, coverage planning is the key stage in the planning process. The aim of the coverage planning is to achieve optimal radio signal coverage by selecting the optimal base station locations for the network.

Many research works have focused on finding the optimal base station locations to achieve the optimal network performance. Early works in the network planning focused on achieving the coverage planning goal. The early work of [2] gave a non-linear optimisation model for the problem of finding the optimal transmitter location in micro-cellular networks. The work of [3] investigated the optimisation algorithms for the base station location placement in Universal Mobile Telecommunications System (UMTS) networks, with the consideration of not only signal overage but both of network traffic and power control. Following this research, the work of [4] made the effort to optimise the UMTS network coverage by optimising the antenna configuration, which can be

seen as a step further ahead from base station location optimisation. A recent work of [5] studied the optimisation algorithms for base station placement and proposed a hierarchical search algorithm for the optimisation problem. The network base station location optimisation problem has been an active research topic since the second generation wireless network and it is still a key problem for the next generation networks, such as heterogeneous networks (HetNet)[6].

To achieve the target of optimal base station deployment, a signal coverage map over the deployment space is essential. Various candidate locations in the map are compared and the optimal one is chosen. Such a coverage map is widely used in the network planning practice. Many researches have been devoted for such a coverage map for network planning purposes. The pioneering work in [7] partitioned the map into areas and adopted an empirical model to predict the path loss contour plot as a path loss map. The work in [8] followed this method and extended it to an outdoor-indoor transient situation. To accurately predict the channel information requires significant amount of computation, therefore many research works are devoted to computer-based simulation. Early works such as the WiSE tools by Bell Labs [9] and CINDOOR [10] were specially designed for designing and planning indoor networks. The method of building such channel maps is mainly the deterministic channel propagation model, which contains roughly two major modelling methods: FDTD related models and ray based models. The work of [11] first used the name of channel map and proposed a ray tracing method for building the channel map. The work in [12] proposed an efficient computational electromagnetics method for building the channel map. For a complete review of channel modelling in HetNet, I refer the readers to the work of [6]. The channel map has long been widely used as an essential tool in network design. However, it still lacks a rigorous mathematical formulation, which limits the further development of the channel map as an essential tool in network planning, especially for MIMO network planning.

With the application of the modern advanced wireless transmission techniques, such as MIMO system, the network performance is largely benefited from those advanced techniques. These advanced techniques are widely deployed in the current and future generation wireless networks, such as HetNet [6]. Meanwhile, to plan networks equipped with these advanced techniques, network planning tools face the challenges of considering these advanced techniques in the planning process. Many challenges

stem from a lack of high dimensional vector form for the channel map. Although the channel map has been widely used as a tool in network planning, a vector form for the channel map has been missing. This limits the development and functionality of the channel map as a tool in advanced network planning, such as MIMO network planning. The major challenge that facing the conventional channel map tools in MIMO channel modelling is the limitation the 2 dimensional channel map. A conventional 2 dimensional channel map lacks the capability to accommodate the higher dimensions of the MIMO channel. The intrinsic drawback of representing the channel distribution in a 2 dimensional or 3 dimensional map failed to capture the MIMO channel in higher dimensions. Because of the higher dimensions of the vector form of the MIMO system, in order to apply the conventional 2 dimensional channel map for MIMO systems, we need to extend the channel map to a vector form.

The purpose of the chapter is to present a straightforward vector form the channel map to the MIMO system based on a mathematical formulation to the vector form of the channel map. Although in practice, the extension to vector form appears straightforward, this is not true in higher dimension MIMO channel, especially in distributed MIMO channel. In such MIMO channels, conventional single transmitter channel map struggles to provide a complete picture of the channel by using 2 dimensional or 3 dimensional maps. To overcome this challenge, we give a vector channel map in a mathematical form. We then also show that this vector form channel map can be constructed based on the conventional 2 dimensional channel map. We further apply this vector channel map to a distributed MIMO network planning and optimisation scenario, which demonstrates the vector channel map as an effective and straightforward extension of a conventional 2 dimensional channel map.

The rest of the chapter is as follows: Section 4.2 gives the definition of channel map for both SISO and MIMO channel. Section 4.3 presents a method of building channel maps for distributed MIMO networks. Section 4.4 gives a numerical example to illustrate the construction of a channel map for distributed MIMO network in a typical network planning scenario. Section 4.5 concludes the work.

4.2 Mathematical Formulation of Channel Map

4.2.1 Single Antenna Channel Map

Channel map has been widely used in network planning. In a deterministic propagation setting, when the transmitter location and propagation configuration is fixed, the channel is then determined from a deterministic channel modelling perspective. In such a scenario, a channel map can be drawn to present the channel information over the signal coverage space. A channel map is designed to give an overview of the channel information over the design space in the form of a map.

In conventional channel maps, the most commonly interested channel parameter is the power information. This is due to the conventional network planning targets, for which coverage planning is the primary target. The coverage planning relies on the power parameters, such as path loss and signal to noise ratio, of the channel information. However, for modern network planning other parameters such as phase and delay are also of interest. Our channel map definition incorporates complete channel information.

In channel map, the receiver location information in the map is modelled as a discrete locational set. In most cases, it is modelled as a discrete grid over the design space. Each potential receiver location is specified by its Cartesian coordinate location. Therefore the receiver locations in the grid covering the map is given as a set:

$$\mathcal{L} = \{(x, y, z) \in \mathbb{R}^3 | (x, y, z) \text{ are the Cartesian coordinates of locations in the map}\} \quad (4.1)$$

The set is a finite set. In channel map, it is common to plot the channel information over all the potential receiver locations, with a fixed source location. Then the *receiver location* set is given as the location set $\mathcal{L}$ subtracting the source location s. It is denoted as:

$$\mathcal{M} = \mathcal{L} \backslash \{s\} \quad (4.2)$$

The number of the potential receiver locations is the cardinality of the set and is denoted as $|\mathcal{M}|$.

Under the assumption that the channel is a narrow band static channel, the channel information set is given as the set of complex number $\mathbb{C}$.

The channel map is defined as a function mapping from the location set $\mathcal{L}$ to the channel set $\mathbb{C}$. The wireless channel can be modelled as the electromagnetic field in the coverage space. In electromagnetic channel modelling, the channel value at a location is the electric field value of the electromagnetic field [73, 74]. Thus we can write:

$$H(s,l) = E(s,l) \tag{4.3}$$

where $E(s,l)$ is the electric field at location l and with the source radiating at location s, and $H(s,l)$ represents the channel information at location l, with the radiating source at location s.

Following the above definitions, we can give a definition of the single antenna channel map

Definition 4.1. (Single Antenna Channel Map) A single antenna channel map is defined as the set of channel map functions that gives the mapping from the physical location set $\mathcal{M}$ to the channel information set $\mathbb{C}$.

Thus, we can write the channel map as a function:

$$f : \mathcal{M} \to \mathbb{C} \quad \text{where} \quad f(l) = H(s,l) \tag{4.4}$$

This definition gives a mathematical formulation of the widely used single antenna channel map in network planning. The channel map is a function that maps the potential receiver locations in a physical map to the channel information. The channel map describes the channel information over the location map.

The channel map function characterises the channel information over the design space. The channel map function at each potential location is determined by the physics of the propagation. Therefore each map function can be written in the form of a Green function [75] as:

$$H(s,l) = \int_s G(p,l)J(p)dp \tag{4.5}$$

where $G(p,l)$ represents the Green function with source at p and the field value at l; $J(p)$ denotes the source current at p; p is the points in the source domain s; the integral is over

the source current. In practice there are specific numerical electromagnetic simulation tools to solve the channel map, such as in [12, 49].

4.2.2 MIMO channel map

For MIMO channel map, the multiple transmitters of the MIMO channel are assumed to be determined at fixed locations. The objective of the MIMO channel map as in the single antenna channel map is to draw a channel information map over the potential receiver locations.

Based on the formulation of the single antenna channel map, we have a vector form of channel map for MIMO systems. In MIMO the propagation channel is extended to multiple transmitters. The channel information is to track each sub-channel between each transmitter and receiver pair. In this case, we write the channel map of multiple transmitters in a form of channel map vector. Each element in the channel map vector is a single antenna channel map generated by one single transmitter. Thus we define the channel map vector as:

Definition 4.2. (Channel Map Vector) A channel map vector is defined as a vector of the channel maps with the same location set $\mathcal{M}$. It is written as:

$$(f_1(\mathcal{M}), f_2(\mathcal{M}), ...f_n(\mathcal{M})) \tag{4.6}$$

where f_i is the i-th channel map.

For the MIMO system, the potential multiple receiver locations form a set of receiver location vector

$$\mathcal{L}_v = \{(l_1, l_2, ...l_m) | l_i \in \mathcal{M}_i \quad \text{for all} \quad 1 \leqslant i \leqslant m\}. \tag{4.7}$$

where $\mathcal{M}_i$ is the potential receiver location set for the i-th map. Each element in the set $\mathcal{L}_v$ is a receiver location vector, identifying the multiple receiver locations. By applying the receiver location vectors to the channel map vector in (4.2), we obtain the MIMO channel matrices.

The channel information for MIMO systems is a complex matrix and the set of channel information can be written as $\mathbb{C}^{m\times n}$. The channel map function is also written in a matrix form. Each element in the matrix form corresponds to a transmitter-receiver pair in the channel matrix.

$$\mathbf{H}(\mathbf{S},\mathbf{L}) = \begin{bmatrix} H_{1,1}(s_1,l_1) & H_{1,2}(s_2,l_1) & \cdots & H_{1,m}(s_m,l_1) \\ H_{2,1}(s_1,l_2) & H_{2,2}(s_2,l_2) & \cdots & H_{2,m}(s_m,l_2) \\ \vdots & \vdots & \ddots & \vdots \\ H_{n,1}(s_1,l_n) & H_{t,2}(s_2,l_n) & \cdots & H_{n,m}(s_m,l_n) \end{bmatrix} \tag{4.8}$$

Like in the single antenna channel map, the channel information can also be represented by the electric field values in a matrix form:

$$\mathbf{H}(\mathbf{L}) = \mathbf{E}(\mathbf{L}) \tag{4.9}$$

Similar as in the single antenna channel map definition, we define the MIMO channel map as the mapping functions from the receiver location vector set to the channel matrix set. The definition is given as follows.

Definition 4.3. (Vector Channel Map) The MIMO channel map is defined as the set of functions that maps the receiver location vector set $\mathcal{L}_v$ to the channel matrix set $\mathbf{H}(\mathbf{S},\mathbf{L})$ as:

$$\mathbf{F}\colon \mathbf{L}_v \to \mathbb{C}^{m\times n} \quad \text{where} \quad \mathbf{F}(\mathbf{L}) = \mathbf{H}(\mathbf{S},\mathbf{L}) \tag{4.10}$$

According to the representation of the electrical field value, the electrical field value $\mathbf{E}(\mathbf{L})$ can also be written in a matrix form:

$$\mathbf{E}(\mathbf{L}) = \int \begin{bmatrix} G_{1,1}(l_1) & G_{1,2}(l_1) & \cdots & G_{1,m}(l_1) \\ G_{2,1}(l_2) & G_{2,2}(l_2) & \cdots & G_{2,m}(l_2) \\ \vdots & \vdots & \ddots & \vdots \\ G_{n,1}(l_n) & G_{t,2}(l_n) & \cdots & G_{n,m}(l_n) \end{bmatrix} \begin{bmatrix} J_1(\mathbf{S}) \\ J_2(\mathbf{S}) \\ \vdots \\ J_n(\mathbf{S}) \end{bmatrix} d\mathbf{p} \tag{4.11}$$

This definition gives a mathematical formulation of the MIMO channel map. Comparing to the single antenna channel map, the MIMO channel map function is a vector

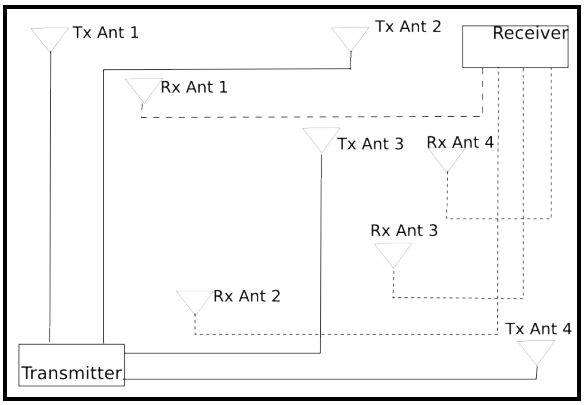

FIGURE 4.1: An Illustration of Distributed Antennas MIMO System

function. It maps the potential receiver location vectors to the channel information matrix. It gives the channel information over the potential receiver locations in the form of a map. The locations in the map are vectors. Such a mathematical formulation has the advantage of representing the abstract location vectors in a vector form map. This feature overcomes the limitation of representing channel information over the 2D or 3D physical map but offering an abstract channel map representing channel information over abstract location vectors. We will utilise this feature in an example of planning distributed MIMO systems in Section 4.4.

4.3 Construction of MIMO channel map using distributed antenna systems

The MIMO has been investigated as one of the key techniques for achieving the high capacity network since the seminal works of [76, 77]. Recently, researchers have focused on applying MIMO techniques in HetNet, especially the distributed MIMO integrated with HetNet [78]. A distributed MIMO system is illustrated in Figure 4.1. In a distributed MIMO system, the multiple antennas in the MIMO systems are not mounted on a conventional antenna array, while they are connected to a central controller to form a distributed antenna array. In HetNet, such a distributed MIMO system can be realised via the cooperation between different tiers of the networks.

We study the method to construct the MIMO channel map based on conventional single antenna channel map in this section. We first introduce the single antenna channel map building tool in network planning. Then we investigate the application

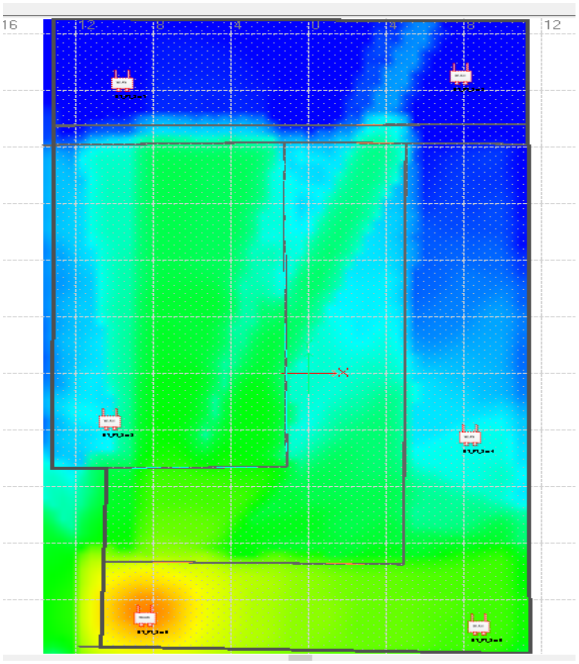

FIGURE 4.2: An Example of Single Antenna Channel Amplitude Map

of the channel map formulation to build MIMO channel map in practice. The focus is to build channel map for networks using distributed MIMO systems. The method follows the formulation of the channel map in the previous section. This demonstrates the application of the channel map formulation in construction of channel maps.

Computational electromagnetic tools are widely used to simulate the propagation of radio waves and predict the channel information in network planning. In this section, we focus on using a single antenna propagation simulation tool to build MIMO channel maps. An example result of channel amplitude information map generated by the simulation tool iBuildNet [79] is shown in Figure 4.2.

According to the definition of the channel map, the channel map predicted by the simulation is a set of channel values mapping onto the location set. In this single antenna channel map case, the locations are the physical locations in the map. Thus, the channel map represents the channel information at each potential location in the map. In distributed antenna systems, the antennas are deployed in a distributed way. Due to the distance between the antennas, we assume the mutual coupling effect between antennas is negligible. So we can simulate the multiple antenna channel map individually without considering the mutual coupling widely existed in antenna array systems. Under such an assumption, the conventional single antenna channel map construction

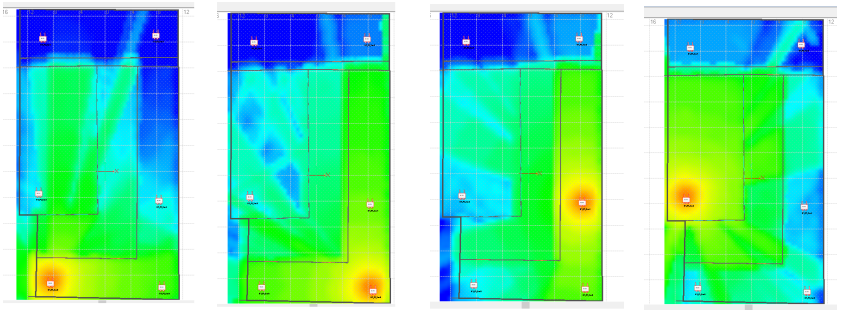

FIGURE 4.3: Channel Amplitude Map Vector

tools by simulating radio wave propagation are suitable in the distributed antenna system case.

With multiple distributed transmitter antennas, the multiple single antenna channel maps generated by single transmitter antenna are arranged to be a channel map vector. Following the single antenna channel map example in Figure 4.2, we set 4 distributed transmitter antennas and construct the channel map vector as in Figure 4.3. Each element map in the vector is a channel map constructed according to one single antenna channel map.

According to the definition of the MIMO channel map, the receiver location vector set is a key component in the construction of the channel map. We discuss the receiver antennas in two different scenarios: traditional antenna arrays and distributed antenna systems. The traditional antenna array is even equipped in mobile terminals. On the other hand, for distributed multiple receiver antennas, it normally requires cooperation between the receiver antennas. It has potential in future wireless network applications, such as high data rate wireless backhaul connections. In this work, we assume the distributed antennas have perfect synchronisation and are deployed in a fully distributed way.

We first study the MIMO channel map construction for multiple receiver antenna using antenna arrays. We assume that the resolution of the map is adequately high to resolve the elements in the receiver array. In this case, the receiver antennas can be represented by the location points in the channel map. Given the fixed array size, geometry and orientation, the receiver location vector is specified using the locations in the map.

The location point set of the channel map in the multiple distributed transmitter antenna channel map is the location set excluding the transmitter locations. It is given as:

$$\mathcal{M} = \mathcal{L} \backslash \{s_1, s_2, \ldots s_m\} \tag{4.12}$$

Following the MIMO channel map Definition 4.3, we have the receiver location vector set as:

$$\mathbf{L}_v = \{(l_1, l_2, \ldots l_m) | l_i \in \mathcal{M} \quad \text{for } 1 \leqslant i \leqslant m\} \tag{4.13}$$

Each receiver location vector $(l_1, l_2, \ldots l_m)$ corresponds to a potential location vector for the array deployment. Each location point l_i in the vector is a physical location point in the map. For each element channel map in the channel map vector, the location point sets only differ in the transmitter location s_i.

Under the assumption of fixed array size, geometry and orientation, we can use a single location point in the set to specify the location of the array. The locations of the rest of the elements in the array can be determined through the geometry of the array. Such a method has been used in modelling the MIMO channel using antenna arrays [80]. In this way, the potential location vector set $\mathbf{L}_v$ for array location degrades to the set of the single location point set of the map $\mathcal{M}$. The relationship can be written as :

$$p : \mathcal{M} \rightarrow \mathcal{L}_v \qquad \text{where } p(l) = (l_1, l_2, \ldots l_m) \tag{4.14}$$

This relationship summarises that the receiver location vector can be replaced by a single location MIMO channel map using antenna array. As the receiver location vector set degrades to the receiver location point set, the MIMO channel map can be built following Definition 4.3 in (4.10). Such a form of MIMO channel map for network planning purposes has been studied in the work of [34, 81]

On the other hand, in MIMO channel map using distributed receiver antenna systems, the receiver locations are chosen from the individual maps in the channel map vector. In this case, the target is to construct an $m \times n$ distributed MIMO channel map. The m receiver antenna locations are chosen from the locations in the map excluding the n

transmitter locations. The receiver location vector can be written as:

$$\mathbb{L} = (l_1, l_2, \ldots l_m) \in \{\mathcal{M} \times \mathcal{M} \times \ldots \mathcal{M}\} \tag{4.15}$$

where '$\times$' represents the Cartesian product of the set. This relation describes the receiver locations for a distributed antenna system are chosen from the combinations of the potential locations in the map.

By the above description for the potential receiver location set, the potential receiver locations are all the possible combinations of m different locations in the map location set. Therefore, we have the following proposition regarding the total number of the potential locations in the channel map.

Proposition 4.4. *The total number of potential locations in a $m \times n$ MIMO channel map is the combination of the m receiver locations from the location set in the map excluding the n transmitters. It is given as*

$$M = C^m_{|\mathcal{M}|-n} \tag{4.16}$$

Each element in the receiver location vector set corresponds to one potential location combination for the multiple receiver antennas. The location vector $L = (l_1, l_2, \ldots l_m)$ specifies the location of the m receiver antenna location in a vector form. Applying this location vector in the single antenna channel map identifies a channel information vector which corresponds to a single-input multiple-output (SIMO) channel vector, which is one column vector as in (4.8). While applying this vector to a channel map vector, the result is a channel matrix.

At this stage, the MIMO channel map construction is completed by looking up the corresponding channel values at each location from the single antenna channel map. This method preserves the conventional single antenna channel map and extends it to build distributed MIMO channel maps.

The resulting matrix is written as:

$$\mathbf{H}(\mathbf{L}) = \begin{bmatrix} f_1(l_1) & f_1(l_2) & \cdots & f_1(l_m) \\ f_2(l_1) & f_2(l_2) & \cdots & f_m(l_m) \\ \vdots & \vdots & \ddots & \vdots \\ f_n(l_1) & f_n(l_2) & \cdots & f_n(l_m) \end{bmatrix} \tag{4.17}$$

The matrix elements $f_i(l_j)$ denotes the channel information in the i-th channel map at location l_j.

Each channel vector $\mathbf{L}$ in the receiver location vector map determines one channel matrix. The channel matrix corresponds to the MIMO channel matrix with the distributed receiver antennas located by the vector $\mathbf{L}$. The channel matrix specifies the MIMO channel matrix with multiple transmitter antennas given in the form of channel map vector and the multiple receiver location vector which is used to identify the channel matrix at each possible receiver location combination.

4.4 Numerical Examples

In this section, we give an example of the MIMO channel map to demonstrate its application in distributed MIMO systems. Following the method in Section 4.3, we build a distributed MIMO channel map for a typical indoor network deployment scenario. The simulation tool for single channel map construction is the Par-Flow simulation method presented in [12, 82, 83].

The simulation scenario is a typical office environment. The floor map is shown in Figure 4.4. The environment comprises walls, doors, windows and ceilings as a typical indoor network planning scenario. The frequency is set to be 2.4 GHz. The bandwidth is set to be 15 KHz as one single carrier bandwidth in the long term evolution (LTE) networks. We deploy a 2×2 distributed MIMO system in the environment.

The 2 transmitter antennas are deployed in a distributed way. For the reason of demonstration, we only choose one set of locations to deploy the 2 distributed transmitter

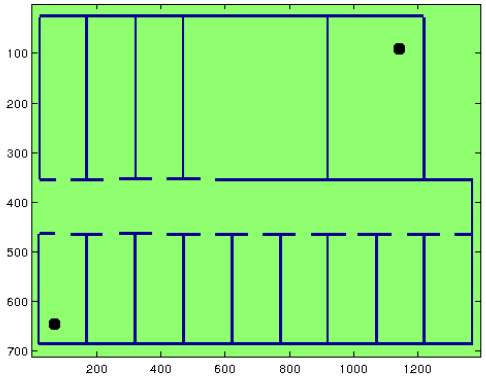

FIGURE 4.4: The Transmitter Antenna Locations

antennas. The transmitter locations are marked in Figure 4.4. The simulated channel amplitude maps and channel phase maps are shown in Figure 4.5 and Figure 4.6, respectively.

Although distributed receiver antennas are still rare in mobile terminals, it is a potential technique for high data rate backhaul connection. It also has the potential to be implemented in a form of cooperative networks [84]. Following the method in Section 4.3, we first construct the channel map vector. The channel amplitude map vector generated by the simulation tool with transmitters at 2 locations is shown in Figure 4.5. The channel phase map vector is shown in Figure 4.6. We arrange the 4 channel maps to a form of channel vector. The mathematical form of the channel map vector follows Definition 4.2. The matrix form is given in 4.8. We generate the complete set of the receiver location vector according to (4.15). Each element in the set is then applied to the channel map vector to identify the channel value as:

$$\mathbf{H}(\mathbf{L}) = \begin{bmatrix} f_1(l_1) & f_1(l_2) \\ f_2(l_1) & f_2(l_2) \end{bmatrix} \tag{4.18}$$

The total number of location points in the map is 988320. According to Proposition 4.4, the number of the total potential location vectors is $C^2_{988320} \sim 4.8839 \times 10^{11}$. In this case, the channel matrix H is a 2×2 channel matrix as in (4.18). The first row of the channel matrix correspond to the Channel Map Vector defined in (4.2) with the first transmitter antenna location. The length of the channel map vector is 2 as the number of the receiver antenna is 2. Next, in the same way we construct the channel map vector

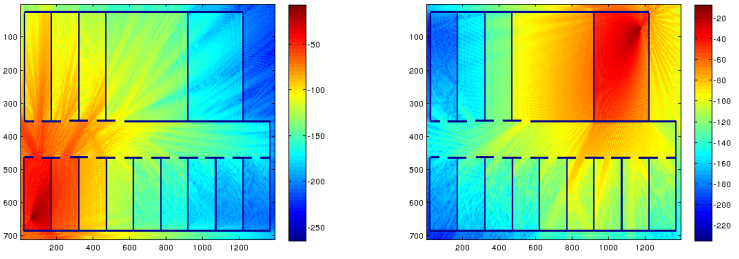

FIGURE 4.5: Channel Amplitude Map Vector

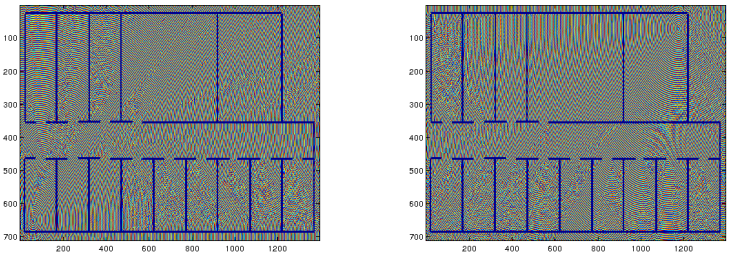

FIGURE 4.6: Channel Phase Map Vector

for the second transmitter location using the channel map of the second transmitter location. After obtaining both channel map vectors, by aligning the 2-element vector from the first set and the 2-element vector from the second set into a 2 matrix form, we have the channel matrix for one potential location combination for receiver antenna. In order to construct the full channel map set all the possible location combination for receivers, we need to list all the possible 2 location combination in the map with the number of $C^2_{988320} \sim 4.8839 \times 10^{11}$.

It costs high computational resource to search the whole possible combinations of the receiver locations. We sample the 988320 receiver locations uniformly to choose 2000 locations as the candidate locations. Thus, the searching space reduces to $C^2_{2000} = 1999000$. It could be argued that the truly optimal locations are outside our searching space due to the sampling. However, the purpose of this example is to show the effectiveness of the vector channel map in network optimisation and also its simple construction based on conventional channel map tools. When precision of the optimisation result is required, we can still search over the whole possible candidate locations to achieve the optimal performance.

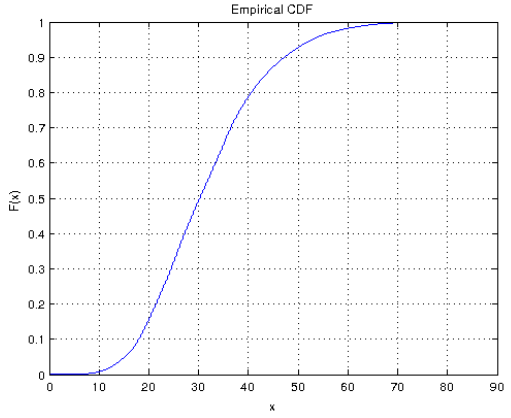

FIGURE 4.7: The CDF of Capacity in Distributed MIMO

4.4.1 Channel Capacity Optimisation

In this part, we optimise the network performance by choosing the receiver locations which achieves the maximum channel capacity.

We look up the channel matrix values in the channel map corresponding to all the receiver location vectors. The result is a table mapping from the receiver location vector to the corresponding channel matrix. Under the assumption of independent noise at each receiver and with uniform power allocation at the transmitter, we then use the channel matrix to calculate the MIMO channel capacity, according to the formula:

$$C = \log_2 \det(I + snrHH^*) \tag{4.19}$$

where H is the channel matrix and H^* is the Hermitian transpose of the channel matrix; $\det(\cdot)$ is the determinant of the matrix and snr is the signal to noise ratio at the receiver.

The transmitting power is set to be 20 dBm. The thermal noise power is given as $N = kTF$, where k is the Boltzmann's constant; T is the temperature in kelvin and F is the bandwidth [85]. Using this formula, as the bandwidth is assumed as 15 KHz and the temperature is assumed as room temperature of 20 degree Celsius, the thermal noise power is obtained as -132 dBm. Plugging the transmitting power and the thermal noise power with the channel matrices from the channel map construction, the channel capacity values are calculated for all the channel matrices constructed in the channel map set.

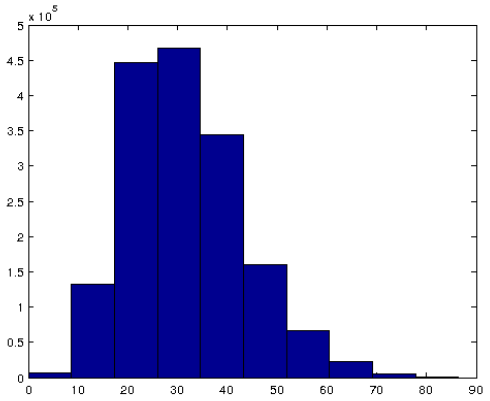

FIGURE 4.8: The PDF of Capacity in Distributed MIMO

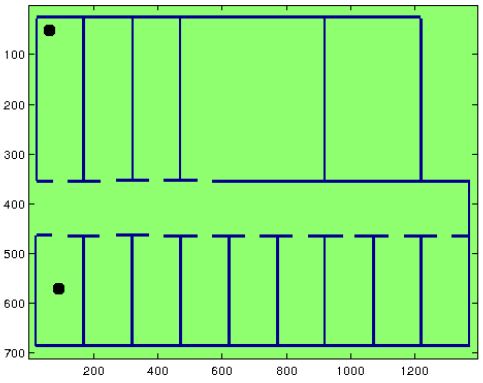

FIGURE 4.9: The Optimal Locations for Receiver Antennas

The cumulative distribution function (CDF) of the resulting channel capacity is shown in Figure 4.7. The probability density function (pdf) of the capacity is shown in Figure 4.8. The statistics of the resulting capacity values are summarised in Table 4.1. The mean value of the capacity is 31.5006 bits/s/Hz and the maximum value is 86.4459 bits/s/Hz. The optimal receiver antenna locations that achieve the maximum capacity are indicated in Figure 4.9.

TABLE 4.1: Statistics of the Capacity Values

Maximum	Minimum	Mean	Median	standard deviation
86.4459	0.0144	31.5006	30.2073	11.5412

The gain of optimally designed receiver location from an arbitrarily random choice of receiver locations is significant in this case. We can see that the majority of the receiver locations support a capacity near the mean value of from 20 to 40 bits/s/Hz range. The optimal capacity value offers a nearly 3 times gain from these mostly likely receiver

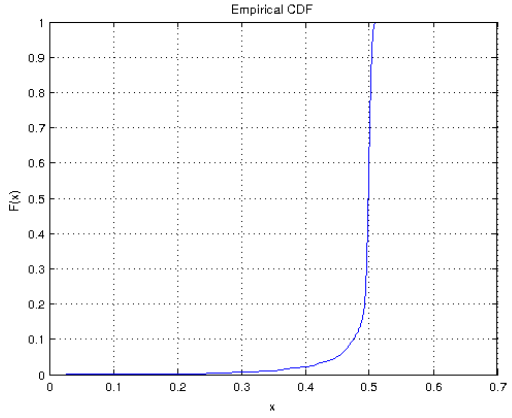

FIGURE 4.10: The CDF of Error Rate in the Distributed MIMO

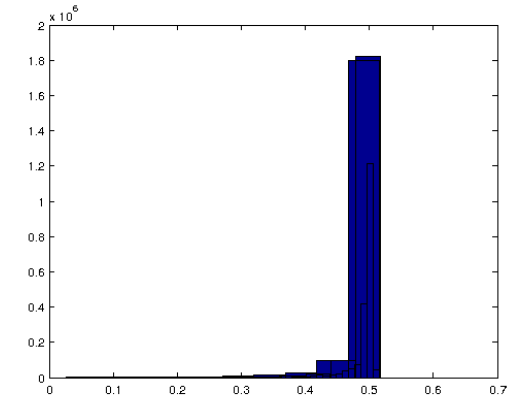

FIGURE 4.11: The PDF of Error Rate in the Distributed MIMO

locations by random choice. This shows that the a significant capacity gain can be achieved by carefully choosing the locations of the distributed antennas.

4.4.2 Error Rate Optimisation

By using the channel map generated for the distributed MIMO system, we also study the choice of receiver locations on error rate performance. We adopt the Alamouti block space time code [86] to be used in the distributed MIMO system in our simulation. The signal-to-noise-ratio (SNR) is set to be 10dB. We simulate the MIMO system using all the candidate channels from the candidate receiver locations. The CDF and the PDF of the error rates at all the candidate locations are given in Figure 4.10 and Figure 4.11, respectively.

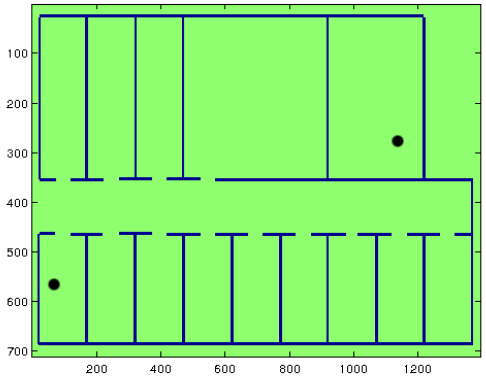

FIGURE 4.12: The Optimal Receiver Antenna Locations

The statistics of the error rate are given in Table 4.2. We see that by choosing the optimal locations of the receiver locations we can achieve the optimal error rate 0.0261 while the mean error rate is about 0.5. The receiver antenna locations achieving this optimal error rate are indicated in Figure 4.12. This result shows that we can achieve good error rate performance even when the majority of the signal coverage is poor, by choosing the optimal receiver locations.

TABLE 4.2: Statistics of the Error Rate

Maximum	Minimum	Mean	Median	Standard Deviation
0.5161	0.0261	0.4906	0.4984	0.0321

4.5 Conclusion

In this chapter, we presented a simple extension of vector channel map based on the conventional 2 dimensional channel map in order to overcome the limitation of modelling higher dimensional vector channels in MIMO systems. We constructed the vector channel map based on a mathematical formulation of the vector form of vector channel maps, which leads to a straightforward construction of vector channel map using conventional 2 dimensional channel maps. Our examples using two different types of 2 dimensional channel map tools (the iBuildNet in Section 4.3 and the Par-Flow in Section 4.3) also showed the adaptability of this vector channel map construction method to different channel map tools.

We also applied the vector channel map to a distributed MIMO network optimisation case. The optimised performance of the MIMO network demonstrated the effectiveness of the proposed vector channel map. Due to the extremely large amount of possible location combinations in the construction of a vector channel map, we reduced the searching location space by uniformly sampling the location space. It could be argued that the truly optimal locations are outside our searching space due to the sampling. However, the purpose of this simulation example is to show the effectiveness of the vector channel map in network optimisation and also its simple construction method based on conventional channel map tools. Therefore, this example demonstrated that the proposed vector channel map is a practical and effective tool in MIMO network optimisation and planning.

Again, the purpose of this chapter is neither to develop a brand new vector channel map tool nor to demonstrate the accuracy of a channel map tool, but to introduce a vector channel map representation in high dimension for MIMO channels and to further demonstrate such a high dimensional channel map can be constructed based on conventional single channel maps. Thus, the vector channel map can serve as a practical tool for network planning and optimisation where efficiency is valued.

Chapter 5

A Least Square Path Loss Model Calibration Method

5.1 Introduction

In order to achieve the performance targets of network planning and optimisation, especially the optimal locations of the network nodes, a path loss map is crucial. For complex environments, empirical path loss models fail to meet the accuracy requirements of network planning and optimisation. In such applications, it is common to employ site-specific computational electromagnetic tools to predict an accurate path loss map.

Ray launching is originally a computer graphics algorithm to emulate the propagation of optic rays. It has also been used in computational electromagnetics for simulating the propagation of electromagnetic waves at high frequency. As an emulation of the multipath propagation of the wireless channel, it offers an effective way to model the wireless propagation channel. In this work, we focus on the use of ray launching algorithms as a site-specific model to predict the path loss map in a specific environment.

The ray optics algorithm has a long history of being employed to simulate the multipath propagation nature of the wireless channel. The early work of [17] first proposed to model the geometric mean value of the multipath channel components using the ray optics method in city street environments. This optic ray based model has been extended

to model the mean channel strength in a large urban environment of Tokyo in [16]. The Bell Labs also developed a ray tracing simulation based channel prediction software tool (WiSE) first for indoor environment [9], then extended to 2D urban environment [19] and full 3D urban environment [20]. The work of [18] developed a ray launching models to model the wireless channel parameters via the simulation of reflection, transmission and diffraction ray propagation mechanisms for indoor environment. For outdoor environment, the work of [51] employed the ray launching model to predict the path loss values. In order to improve the modelling accuracy, the effective building material properties, which use the measurement to calibrate the modelling parameters, have been introduced in [52].

On the other hand, more works have been focused on improving the computational efficiency of the ray optics based simulation channel models. The works of [24, 25, 27] proposed more efficient 3D environment modelling and processing methods for ray optics simulation. These efficient environment modelling and processing methods significantly improved the computational efficiency of the ray optics simulation based channel prediction models.

Despite the aforementioned research works on using ray optics as an effective channel modelling tool, a ray tracing model which directly models the path loss values is still missing. The conventional electromagnetic ray tracing algorithm computes the electromagnetic field, which is a complex value. In order to consider the multipath effect in the path loss calculation, the complex number field values are summed and squared to calculate the power loss from the field value. Such a way is computationally costly and thus limits its applications in the practice of network planning and optimisation.

To overcome the above stated drawbacks of the conventional ray tracing path loss prediction model, we propose a multipath path loss model based on ray launching which traces the path loss values along the individual ray paths and calculates the total channel effect by simply averaging over the path loss values of the individual paths. Such a model has been studied for mmWave channel in Chapter 3. This ray launching simulation model has been extended to accommodate more propagation parameters and to an outdoor environment in this chapter. Moreover, I developed an efficient model parameter calibration method using available measurements, which significantly improves the modelling accuracy.

5.2 The Sum-and-Average Multipath Path Loss Model

5.2.1 Background and Motivation

The wireless channel is normally modelled by the multipath model as

$$H(t) = \sum_i h_i(t) \tag{5.1}$$

where h_i is the individual multipath components. Following the simple channel model, the received signal through this multipath channel can be represented as:

$$r(t) = s(t) \ast H(t) \tag{5.2}$$

where $s(t)$ is the transmitted signal and $\ast$ denotes the convolution operation.

The path loss is defined as the ratio between the transmitted power and the received power in dB as:

$$L = 10 \log_{10} \frac{P_t}{P_r} \tag{5.3}$$

where P_t and P_r are the transmitted power and the received power, respectively. Following the above signal model in (5.2), we can write the path loss as

$$L = -10 \log_{10} H(t)^2 \tag{5.4}$$

According to Jensen's inequality, we have the following result:

$$\log_{10}(\frac{\sum h_i}{n}) \geqslant \frac{\sum \log_{10}(h_i)}{n} \tag{5.5}$$

The path loss values in the multipath signal model (5.2) can be written as:

$$\log_{10}(\sum h_i) = \log_{10}(\frac{\sum h_i}{n}) + \log_{10} n \tag{5.6}$$

Because $\log_{10} n$ is always non-negative, we have the following result:

$$\log_{10}(\sum h_i) = \log_{10}(\frac{\sum h_i}{n}) + \log_{10} n \tag{5.7}$$

$$\geqslant \frac{\sum \log_{10}(h_i)}{n} + \log_{10} n \tag{5.8}$$

If we define the difference between the two path loss values as D, then we have the following form:

$$D = \log_{10}(\sum h_i) - \frac{\sum \log_{10}(h_i)}{n} \tag{5.9}$$

$$\geqslant \log_{10} n \tag{5.10}$$

We see that $\log_{10} n$ can be seen as a lower bound for the difference between the two path loss values from the two calculation methods. The minimum value for the difference D will be bounded by $\log_{10} n$. However, this value only acts as a lower bound. The exact values in applications depend on the values of the multipath channels. We will present a numerical example to illustrate the behaviour of the difference D with various path loss values.

The result in (5.10) gives a lower bound of the difference caused by using the sum-and-average path loss method. However, in real applications, the difference can often be negligible. In Figure 3.1 in Chapter 3, the differences of various numbers of paths using the sum-and-average model has been shown. We notice that when the individual path loss value is above 20 dB the difference is negligible. This behaviour of the path loss values also appears independent of the number of the paths. We will exploit this property of the multipath propagation in the rest of this chapter. Our measurement in this chapter showed that the path loss values measured in our measurement environment are higher than 20 dB. Thus, we can extend the path loss model based on this property to our measurement environment.

Our empirical observation showed that the sum-and-average method of multipath path loss calculation has negligible difference to the conventional method. The validation of this sum-and-average multipath path loss calculation method supports the direct path loss modelling based on ray launching simulation.

5.2.2 The Sum-and-Average Multipath Path Loss Model based on Ray Launching

According to the sum-and-average multipath path loss calculation method, we can calculate the path loss value of a multipath channel by calculating the path loss value of each individual path and averaging them as:

$$L = \frac{\sum L_i}{n} \tag{5.11}$$

where L_i is the path loss value of the i-th individual path. Normally, this individual path loss value is a function of the propagation distance. Thus, we can trace the propagation distance of each individual path and calculate the corresponding path loss values. If we model the propagation mechanisms consisting of free-space propagation, reflection, transmission and diffraction, then we can write the path loss value in terms of the corresponding propagation loss values. In such a case, we have the following path loss model for each individual path as:

$$L_i(d_i) = l_i(d_i) + p \cdot Lr_i + q \cdot Lt_i + s \cdot Ld_i \tag{5.12}$$

where l_i is the distance dependent loss and d_i is the propagation distance; p, q and s are the numbers of the reflections, the transmissions and the diffractions during the propagation path; Lr_i, Lt_i and Ld_i are the reflection loss, transmission loss and diffraction loss; respectively.

Following the sum-and-average multipath path loss calculation method, we can use a ray launching simulation model to trace the propagation distances d_i and the numbers of the propagation mechanisms p, q and s during an individual path, to predict the path loss values for the individual paths. These individual path loss values are then input to the sum-and-average path loss method to calculate the path loss values of the multipath channel.

Different from the conventional ray tracing method for computational electromagnetics which calculates the electromagnetic field values along the ray paths, in this case, we employ a ray launching simulation method to calculate the path loss values of the individual propagation paths by tracing the propagation distance of each ray path and counting the numbers of the propagation mechanisms. Such a ray launching

simulation significantly reduces the computational complexity. Furthermore, existing ray tracing/launching algorithms from computer graphics can be readily transferred to this application.

The traced propagation distances are used to determine the path loss values according to a path loss model, such as free-space, COST-HATA and log-distance model. In this work, we use the free-space path loss model to calculate the distance-dependent path loss values. The free-space model gives the path loss value as:

$$L(d) = 20\log(d) + 20\log(f) + 32.45 \tag{5.13}$$

where d is the propagation distance in kilometre and f is the frequency in megahertz. Replacing the model in (5.13) into (5.12), we have the following result:

$$L_i(d_i, f) = 20\log(d_i) + 20\log(f) + p \cdot Lr_i + q \cdot Lt_i + s \cdot Ld_i + 32.45 \tag{5.14}$$

The ray tracing simulation provides the propagation mechanisms input p, q and s. However, the propagation loss values can be determined either by theoretical values or by calibration using measurement. We will discuss both methods for determining the propagation loss values Lr_i, Lt_i and Ld_i in the following.

5.2.3 Theoretical Model Parameter Values

According to the Fresnel equation, the power reflection coefficients, for an optical ray impinging from free space to a material surface, are given as:

$$R_v = \left|\frac{\sqrt{1 - \frac{(\sin\theta)}{n}} - n\cos\theta_i}{\sqrt{1 - \frac{(\sin\theta)}{n}} + n\cos\theta_i}\right|^2 \tag{5.15}$$

$$R_h = \left|\frac{\cos\theta_i - n\sqrt{1 - (\frac{\sin\theta_i}{n})^2}}{\cos\theta_i + n\sqrt{1 - (\frac{\sin\theta_i}{n})^2}}\right|^2 \tag{5.16}$$

where n is the refractive index, which is given as $n = \sqrt{\epsilon_r \mu_r}$. The quantities ϵ_r and μ_r are the relative permittivity and the relative permeability of the material. The reflection

loss can be written as:

$$Lr = 10\log\frac{p_i}{p_r} \tag{5.17}$$

$$= -10\log R \tag{5.18}$$

where R is the power reflection coefficient or the reflectance, given in (5.16).

For the transmission, the transmission loss can be written as:

$$Lt = -10\log\frac{p_i}{p_t} = -10\log T \tag{5.19}$$

where T is the power transmission coefficient and is given as: $T = 1 - R$.

Thus, we can calculate the refractive index for a material through the relative permittivity and the relative permeability of the material and then use the refractive index to calculate the reflection loss and the transmission loss.

Similarly, the diffraction loss can be written as:

$$Ld = -10\log\frac{E_i}{E_d} \tag{5.20}$$

where E_i and E_d are the incident ray field value and the diffracted ray field value, respectively. The diffracted ray field is given by the uniform diffraction theory as:

$$E_d = E_i RD\sqrt{\frac{S'}{S(S+S')}} \tag{5.21}$$

where R is the amplitude reflection coefficient; the $S^{'}$ and S denote the distance from the diffraction point, to source point and to the receiver point, respectively. The diffraction coefficient D is given as:

$$\begin{aligned} D_v^h = \frac{\exp -j\pi/4}{2n\sqrt{2k\pi}}\{&\cot[\frac{\pi+(\phi+\phi^{'})}{2n}]F(kL\alpha^{+}(\phi-\phi^{'})) \\ &\cot[\frac{\pi-(\phi-\phi^{'})}{2n}]F(kL\alpha^{-}(\phi-\phi^{'})) \\ &R0_v^h\cot[\frac{\pi-(\phi+\phi^{'})}{2n}]F(kL\alpha^{-}(\phi+\phi^{'})) \\ &Rn_{nv}^h\cot[\frac{\pi+(\phi+\phi^{'})}{2n}]F(kL\alpha^{+}(\phi+\phi^{'})) \end{aligned} \tag{5.22}$$

TABLE 5.1: Electromagnetic Parameters of 3 Materials

	Permittivity ϵ	Permeability μ	Refractive Index n
Glass	10	1	3.1622
Brick	9	1	3
Concrete	4.5	1	2.121

where $F(*)$ is the Fresnel integral, given as:

$$F(x) = 2j\sqrt{x}e^{jx}\int_{\sqrt{x}}^{\infty} e^{-j\tau^2}d\tau \tag{5.23}$$

and L is given as:

$$L = \frac{SS^{'}}{S+S^{'}} \tag{5.24}$$

And

$$\alpha^{\pm} = 2\cos^2\left(\frac{2n\pi N^{\pm} - \beta}{2}\right) \tag{5.25}$$

where $\beta = \phi \pm \phi^{'}$. $N^{\pm}$ are the integers which most nearly satisfy the equations:

$$2\pi nN^{+} - \beta = \pi \qquad\qquad 2\pi nN^{-} - \beta = -\pi$$

Following (5.20) and (5.21), we have the diffraction loss given as:

$$Ld = -10\log\frac{E_d}{E_i} = -10\log|RD\sqrt{\frac{S^{'}}{S(S+S^{'})}}| \tag{5.26}$$

where R and D are the reflection coefficient and the diffraction coefficient, respectively. We notice that the diffraction coefficient D and the diffraction loss Ld both are functions of the distances S and $S^{'}$. For simplicity of calculation, we choose the values for S and $S^{'}$ both as one wavelength in the following calculation.

We choose 3 different types of materials that are common in the buildings and constructions: glass, brick and concrete. Their electromagnetic parameters at 2 GHz are listed in Table 5.1 [58].

Using the loss values given in (5.18), (5.19) and (5.26), we can calculate the theoretical values of the propagation loss for different materials. The results of the theoretical loss values for the 3 materials are plotted in Figure 5.1, Figure 5.2 and Fig .5.3. In the 3 figures, the loss values are plotted against the incident angle from 0 to $\pi/2$. For the

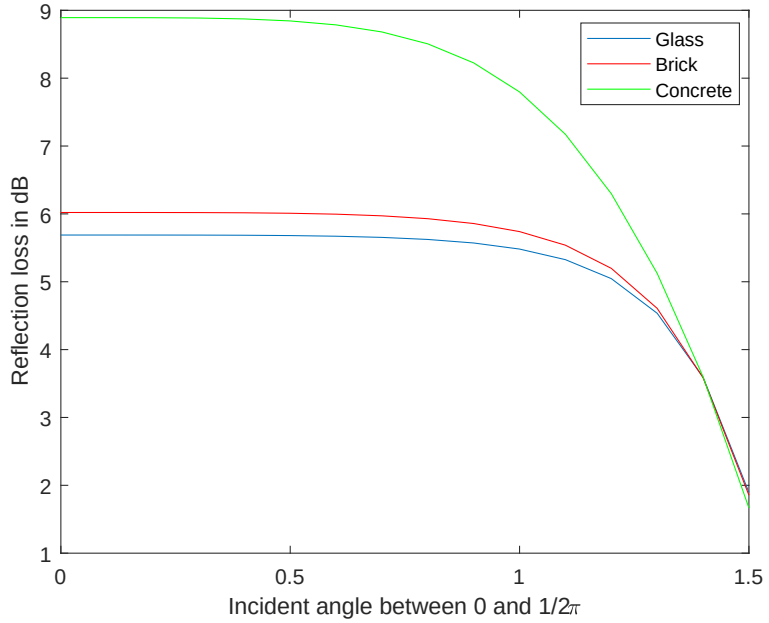

FIGURE 5.1: Theoretical Reflection Loss Values

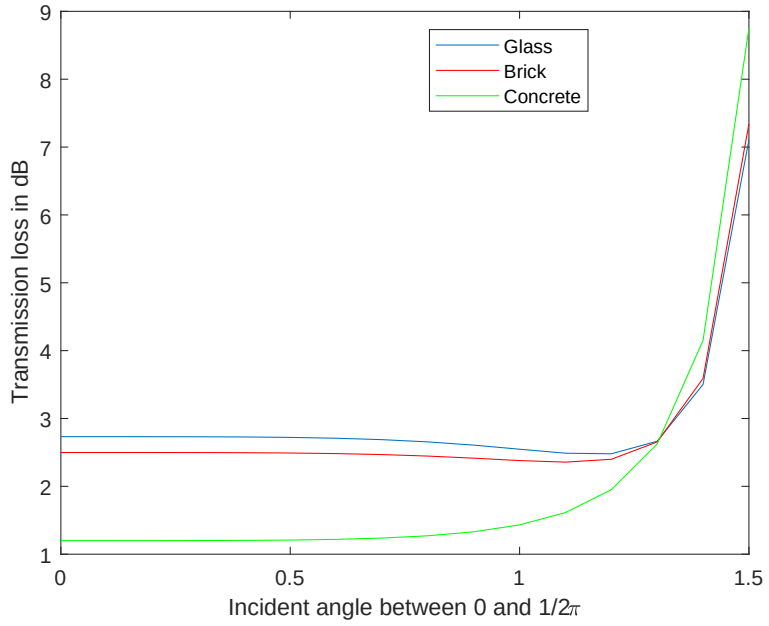

FIGURE 5.2: Theoretical Transmission Loss Values

diffraction loss, the receiver point is fixed as the angle of $\phi = 4\pi/3$ and the diffraction wedge is assumed to be a 90 degree corner.

From the above numerical results of the loss values for the 3 materials, we summarise the loss values of the 3 materials in Table 5.2.

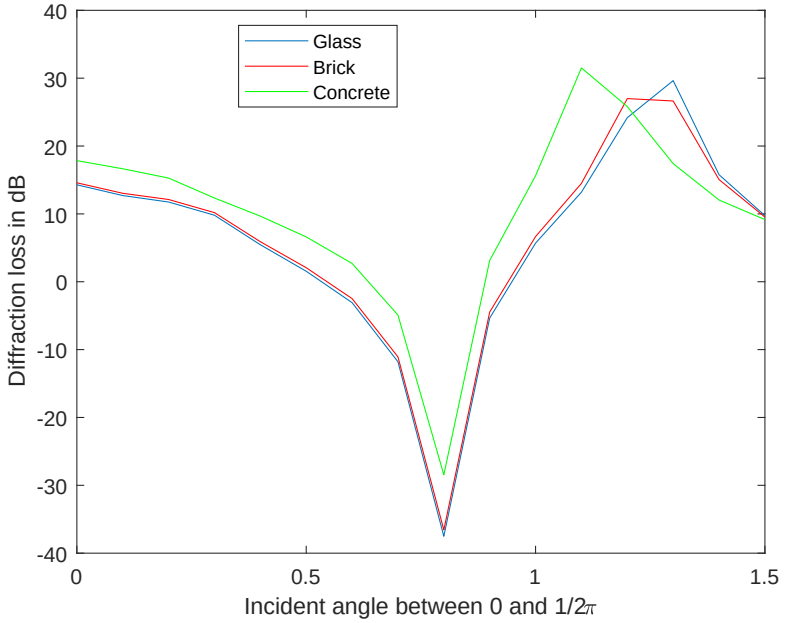

FIGURE 5.3: Theoretical Diffraction Loss Values

TABLE 5.2: Theoretical Loss Values of 3 Materials

	Mean Lr	STD Lr	Mean Lt	STD Lt	Mean Ld	STD Ld
Glass	5.1572 dB	1.0390 dB	2.9891 dB	1.1212 dB	6.0025 dB	15.6057 dB
Brick	5.3990 dB	1.1583 dB	2.8448 dB	1.2333 dB	6.4180 dB	15.2964 dB
Concrete	7.4459 dB	2.1985 dB	2.0498 dB	1.9501 dB	10.1522 dB	13.5537 dB

5.2.4 Sum-and-Average Model with Various Materials

In a complex environment, the multipath propagation encounters various types of materials during a single path propagation. In this case, to improve the modelling accuracy, we can extend the model in (5.14) to account for the multiple materials as:

$$L_i(d_i, f) = 20\log(d_i) + 20\log(f) + \sum_j (p_j Lr_i^j + q_j Lt_i^j + s_j Ld_i^j) + 32.45 \tag{5.27}$$

where j denotes the number of materials; p_j, q_j and s_j are the numbers of the propagation mechanisms for the j-th material; Lr_i^j, Lt_i^j and Ld_i^j are propagation loss values of the j-th material in the i-th path.

In order to implement this model, we establish a database for the propagation loss values for various materials. To determine the theoretical values, we can use the electromagnetic parameters to calculate the propagation loss values for the typical materials as in Table 5.2.

5.2.5 An Efficient Parameter Calibration Method for the Model

Additional to determining propagation loss values via theoretical analysis, if measurement is available, we can also use the measurement to determine the propagation loss values.

We can write the path loss value from a sum-and-average model at one measurement location as:

$$\begin{aligned} L &= \frac{\sum L_i(d_i, f)}{n} \\ &= \frac{1}{n}\sum[20\log(d_i) + 20\log(f) + \sum_j (p_j \cdot Lr_i^j + q_j \cdot Lt_i^j + s_j \cdot Ld_i^j) + 32.45] \end{aligned} \tag{5.28}$$

We can write the path loss values from multiple receiver locations in a vector form as:

$$\begin{aligned} \mathbf{L} &= \{\frac{\sum L_i^1(d_i, f)}{n}, \frac{\sum L_i^2(d_i, f)}{n}, \ldots, \frac{\sum L^k(d_i, f)}{n}\} \\ &= \{\frac{1}{n}\sum[20\log(d_i^1) + 20\log(f) + \sum_j (p_j \cdot Lr_i^j + q_j \cdot Lt_i^j + s_j \cdot Ld_i^j) + 32.45], \\ &\frac{1}{n}\sum[20\log(d_i^2) + 20\log(f) + \sum_j (p_j \cdot Lr_i^j + q_j \cdot Lt_i^j + s_j \cdot Ld_i^j) + 32.45], \ldots, \\ &\frac{1}{n}\sum[20\log(d_i^k) + 20\log(f) + \sum_j (p_j \cdot Lr_i^j + q_j \cdot Lt_i^j + s_j \cdot Ld_i^j) + 32.45]\} \end{aligned} \tag{5.29}$$

where k denotes the k measurement locations.

We can use a nonlinear LS method to estimate the values of the parameters Lr_i^j, Lt_i^j and Ld_i^j. The LS problem can be formulated as:

$$\{Lr, Lt, Ld\} = \arg \min_{Lr_i^j, Lt_i^j, Ld_i^j} \sum\{\mathbf{L} - \mathbf{M}\} \tag{5.30}$$

where $\mathbf{M}$ is the measurement data vector; and vector $\mathbf{L}$ is the modelling path loss value vector resulting from the sum-and-average model based on ray launching simulation in (5.29).

The LS problem formulated in (5.30) can be solved efficiently by various nonlinear LS problem solvers. With the measurement data available, the solution to this nonlinear LS problem provides the parameters for the loss values.

In general this problem is a nonlinear problem because the function of sum-and-average is nonlinear. However, in complex multipath propagation environment, we can further simplify this nonlinear problem to a linear problem, for which highly efficient numerical methods are available to solve.

In a complex environment where rich multipath propagations are available, we can choose the measurement locations where there is only a single arriving ray. In this case, the above propagation path loss values are simplified to single path propagation loss values. This single path value is a special case for the result in (5.29) when $n = 1$:

$$\begin{aligned}\mathbf{L}_1 &= \{L_i^1(d_i, f), L_i^2(d_i, f), \ldots, \sum L(d_i, f)\} \\ &= \{20\log(d_i^1) + 20\log(f) + \sum_j (p_j \cdot Lr_i^j + q_j \cdot Lt_i^j + s_j \cdot Ld_i^j) + 32.45, \\ &\quad 20\log(d_i^2) + 20\log(f) + \sum_j (p_j \cdot Lr_i^j + q_j \cdot Lt_i^j + s_j \cdot Ld_i^j) + 32.45, \ldots, \\ &\quad 20\log(d_i^k) + 20\log(f) + \sum_j (p_j \cdot Lr_i^j + q_j \cdot Lt_i^j + s_j \cdot Ld_i^j) + 32.45\}\end{aligned} \tag{5.31}$$

Now applying (5.31) to replace the path loss modelling vector $\mathbf{L}$ in the LS formulation in (5.30), the nonlinear LS problem becomes a linear LS problem as:

$$\{Lr, Lt, Ld\} = \arg \min_{Lr_i^j, Lt_i^j, Ld_i^j} \sum \{\mathbf{L}_1 - \mathbf{M}\} \tag{5.32}$$

We can write the loss parameter in the form of a vector as :

$$\beta = \{Lr_1, Lt_1, Ld_1, \ldots, Lr_k, Lt_k, Ld_k\}$$

where k denotes the k-th material.

Thus, the linear LS problem can be formulated as:

$$\mathbf{L}\beta = \mathbf{M}$$

The solution of this linear LS problem is given as:

$$\hat{\beta} = (\mathbf{L}^T\mathbf{L})^{-1}\mathbf{L}^T\mathbf{M}$$

These estimated parameters using the measurement data are used as parameter calibration to improve the modelling accuracy. Because of the high computational efficiency of the linear LS algorithm, this calibration method achieves significant improvement in computational efficiency, compared with the nonlinear optimisation method such as simulated annealing used in [26].

5.3 Simulation, Measurement and Calibration

5.3.1 Environment Description

We choose an urban outdoor environment to validate the simulation model with measurement. The environment is a business park in Shenzhen, China. The area is about 500 metres by 500 metres square area. There are several high office buildings in the environment. It is a typical urban city environment for cellular network deployment. The surfaces of the buildings consist of concrete, glass and bricks. There are also trees and plantation in the environment. The map of the environment is shown in Figure 5.4.

5.3.2 The Propagation Setting and Channel Measurement

The transmitter antenna is mounted on an LTE base station. The locations of the transmitter antennas are indicated in the map in Figure 5.7. The frequency is 2.1 GHz as in LTE systems. The receiver antenna is assumed to be omnidirectional with a 1.0 m height above the ground.

5.3.3 Simulation Setting

The simulation uses a 3D ray launching simulation algorithm. The ray launching algorithm traces the propagation distances of the propagation rays via geometric optics. The reflection and the transmission mechanisms are traced along ray propagation paths. The diffraction mechanism is also traced and modelled. The numbers of these reflection, transmission and diffraction propagation mechanisms are recorded. Different from conventional ray tracing/launching algorithms which calculated the field values along the paths, this ray launching algorithm only traces the propagation path distances

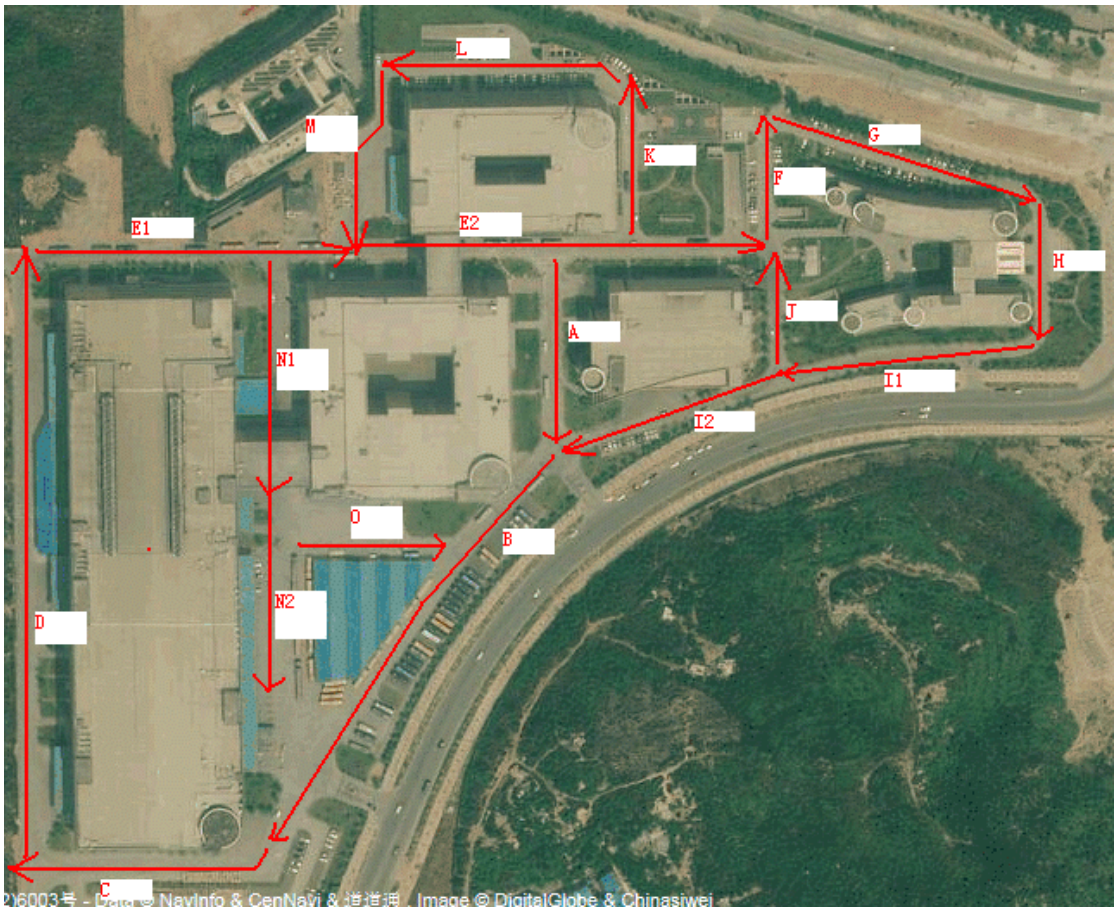

FIGURE 5.4: The Measurement Environment Map

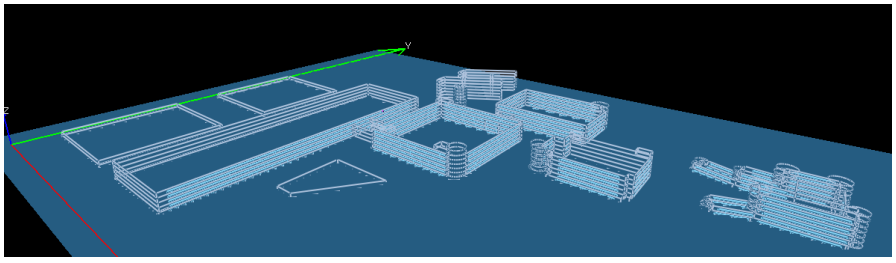

FIGURE 5.5: The 3D Model of the Environment

and records the numbers of the three propagation mechanisms, which is both highly adaptive from the ray optics algorithms and efficient in computation.

The modelling of the environment in a 3D form is essential to implement the ray launching simulation. In this case, we model the environment into a 3D model. The 3D view of the environment model is shown in Figure 5.5. The materials in the environment are specified corresponding to the real environment. The theoretical values for the materials that we use are listed in Table 5.2.

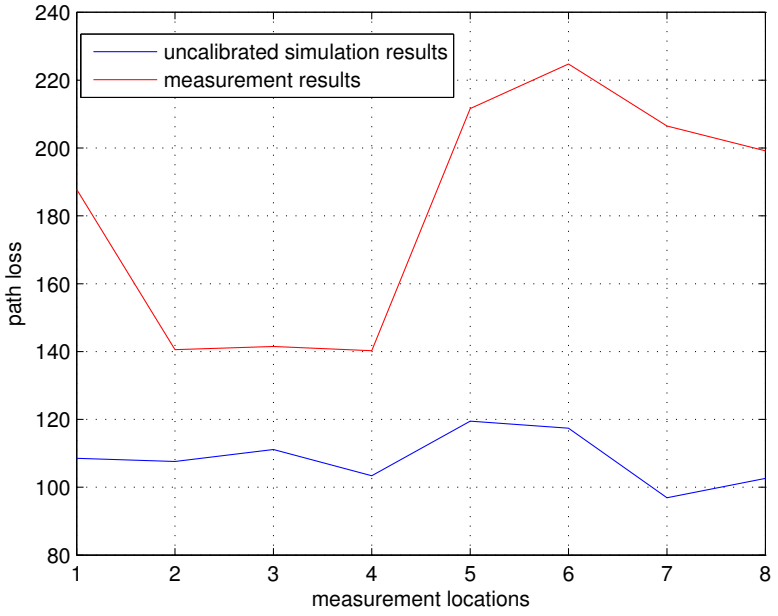

FIGURE 5.6: Simulation Result using Theoretical Parameter Values

5.3.4 Simulation Results - Un-calibrated

The simulation result using the theoretical values for the loss values in Table 5.2 is plotted in Fig 5.6. We can see that the prediction error is large in this case.

5.3.5 Parameter Calibration

The loss parameters are then calibrated using the linear LS method. According to the linear LS method in (5.32), we choose the receiver locations that only have single arriving rays in order to implement the linear LS method. We use the measurement data from the first transmitter antenna location to calibrate the loss parameters. In our simulation, we notice that the diffraction mechanisms take place scarcely. Therefore we ignore the diffraction mechanism in order to improve the computational efficiency. To further simplify the simulation complexity, we assume that the materials in the environment are universal. In this case, we calibrate only the 2 parameters of reflection loss Lr and the transmission loss Lt. The two transmitter antenna locations are indicated in Figure 5.7.

We then use the two calibrated loss values to simulate the ray launching algorithm for the transmitter antenna at location 2. We choose 8 measurement locations in the map

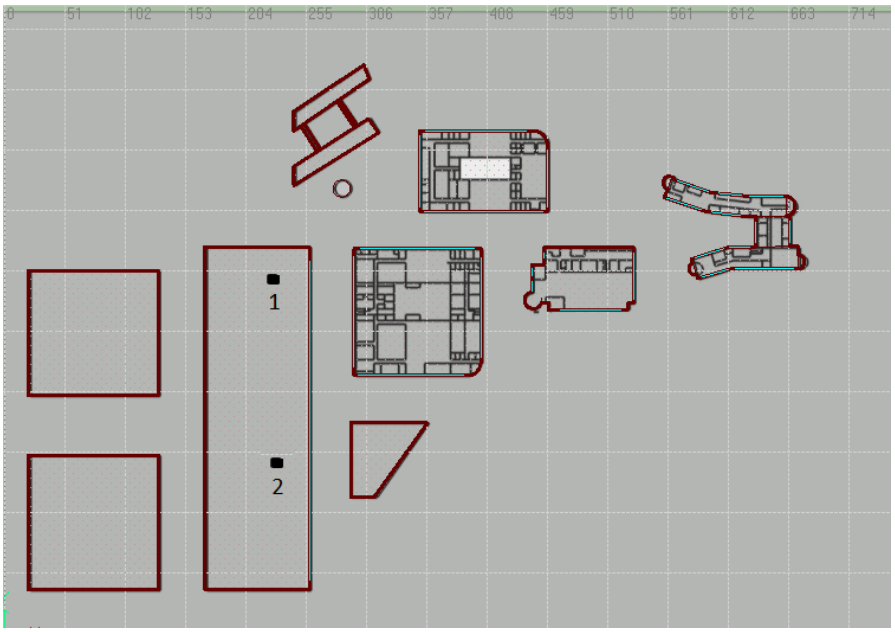

FIGURE 5.7: 2 Transmitter Locations

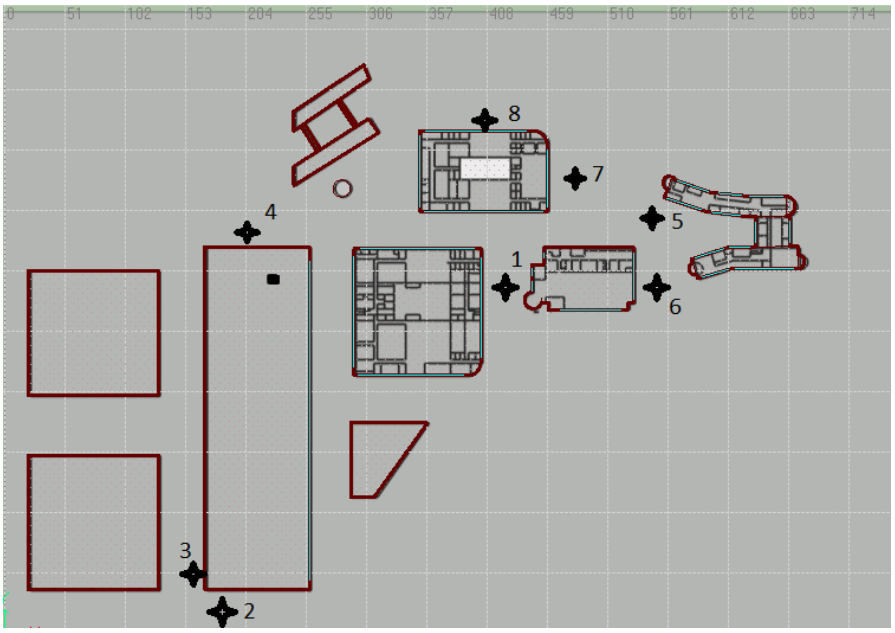

FIGURE 5.8: 8 Measurement Locations

for the channel of transmitter location 2. The 8 measurement locations are indicated in the map in Figure 5.8. The comparison between the calibrated simulation results and the measurement is plotted in Figure 5.9. The loss parameter values before and after calibration are listed in Table 5.3 with the root mean square (RMS) errors.

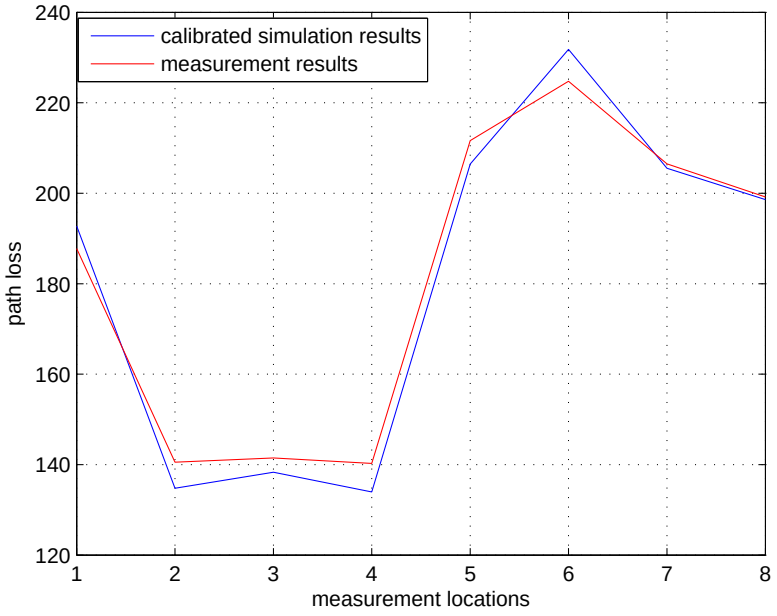

FIGURE 5.9: Calibrated Model Simulation Results

TABLE 5.3: Loss Values and Error Comparison

	Reflection Loss	Transmission Loss	RMS Error
Un-calibrated	7.4457 dB	2.0498 dB	79.8371 dB
Calibrated	10.1760 dB	23.7793 dB	4.8214 dB

5.3.6 Discussion and Analysis

In this simulation, we group the measurement values into 2 groups according to the transmitter antenna locations: the first transmitter antenna location and the second transmitter antenna location. The first set of the measurement data is used to determine the model parameter values. Next we use these calibrated parameter values in the simulation model to predict the channel values of the second transmitter antenna. The result shows that the calibrated modelling parameter significantly improves the modelling accuracy.

We notice that the major difference between the theoretical values and calibrated parameter values is in the transmission loss. This is because in our ray launching simulation the theoretical transmission loss is only calculated at the reflection surface where the thickness of the material is neglected. However, this is inaccurate because the transmission loss is largely caused by the thickness of the wall material. This caused the major error of the theoretical values in the model.

5.4 Conclusion

In this chapter we developed an efficient parameter calibration method for a group of ray launching propagation models, which also include the ray launching model proposed in Chapter 3. For the first time, the loss values from the propagation mechanisms are parametrised as adjustable parameters including reflection loss, diffraction loss, refraction loss and free space propagation loss in the ray based propagation models. However, due to the non-linearity of this model, the high computational complexity in such a calibration method limits its applications in network design. By exploiting the linear structure of the model, we further developed a simplified linear version of the non-linear LS calibration method for the model. Such a linear LS method improves the computational efficiency in network planning and optimisation applications. With the available measurement data, we can then calibrate these loss values in order to improve the overall accuracy of the predication model.

In the calibration of the ray based propagation models, we also calculated the theoretical parameters for the ray launching model as the initial input parameter values for a specific outdoor environment. Then we calibrated the parameters using the linear LS algorithm with the available measurement data from a specific outdoor environment. Our simulation results demonstrated that the linear LS calibration method significantly improves the prediction accuracy over the un-calibrated parameter values.

Again, the purpose of this chapter is not to develop a brand new ray based propagation model, although I extended a ray propagation model similar to the one proposed in Chapter 3 to accommodate more loss parameters. The main contribution of this chapter is a new linear LS method to calibrate these newly introduced loss parameters for the model, which plays an important role to improve the accuracy of such ray based propagation models.

Chapter 6

Wireless Channel Capacity from Electromagnetic Propagation Perspective

6.1 Introduction

Wireless channel capacity has played a key role in evaluating the wireless network performance. The classical view on the wireless channel is the fading channel model [87] which models the wireless channel as a random channel. Such a view overly simplifies the wireless channel by statistical characteristics of the channel. Without considering the physics underlying the wireless channel, the purely statistical characterisation of the wireless channel failed to address the spatial characterisation of the wireless channel. For the purpose of understanding the spatial property of the wireless channel capacity, electromagnetic field and propagation concepts are essential to understand the physical limits of the wireless channel as the electromagnetic field and propagation underpin the wireless channel.

The classical Shannon channel capacity is defined based on a point-to-point channel model. While from electromagnetic field and propagation perspective, the wireless channel is characterised by its spatial property from the continuous electromagnetic field. The continuous electromagnetic field poses a challenge to the classical point-to-point channel model in fully capturing the spatial property of the wireless channel.

For example, the performance of the wireless networks relies on the electromagnetic field coverage which normally considers the coverage space as a whole continuous space instead of discrete points. Closing the gap between the classical Shannon information theoretical channel capacity and the Maxwellian electromagnetics has been a challenging problem [74].

Various attempts to tackle the issue of the spatial property of wireless channel capacity introduces new definitions for the wireless channel capacity by taking the spatial property into account. In [88], the authors introduced the concept of transport capacity. The transport capacity is defined as a distance weighted capacity. By weighing the Shannon capacity with the distance between the transmitter and the receiver, the transport capacity simplifies the spatial treatment of distance-dependent capacity to a capacity-distance product. The work of [89] studied the wireless network capacity by averaging the Shannon capacity over the coverage space. Such an averaging operation to the network coverage space is common practice in evaluating the wireless channel capacity over the whole coverage space.

On the other hand, research efforts trying to capture the physical limits of the wireless channel from an electromagnetic view have a long history. The early work in [90] pioneered the investigation on the equivalent frequency bandwidth a 2D scatter field can support as a communication channel. The work showed that the equivalent bandwidth is proportional to the size of the receiver. The following work of [91] extended the work to the case of the equivalent discrete number of degree-of-freedom of the 2D scattering field. The work in [92] investigated the degree-of-freedom of an electromagnetic scattering field under various propagation and environment conditions. A more recent work in [93] established a relationship between the degree of freedom in a scattering field by assuming the scatterers are independent and identically distributed. The authors of [94] derived the space channel capacity using the concept of the degree of freedom in the electromagnetic field. The work of [95] established the duality between space and time in wireless channel, based on the concept of the degree-of-freedom of electromagnetic field originated from [91].

One of the major applications of the degree of freedom of space channel is to study the capacity limit of the MIMO channel. The work of [96] derived the limiting result of degree-of-freedom from electromagnetic radiation principle, for the MIMO system.

The following work of [97] studied performance of the MIMO channel under various propagation conditions. The work in [98] investigated the number of degree-of-freedom in MIMO channel using the concept in [91] and gave a MIMO channel performance limit from electromagnetics. The following work of [99] extended the study further to understand the electromagnetic propagation limits on the performance of the MIMO channel.

Besides the applications to the study of the MIMO channel, the performance of the scaling law in wireless networks is another active topic where the study of the electromagnetic propagation on the network performance has been carried out. The work of [88] inspired the study of the scaling law of the wireless network capacity. The work in [100] studied the capacity scaling law under the physical limits is a square root of n. More recently, the work in [101] investigated the capacity scaling law of wireless networks under physical propagation limits and resolved a contradiction between the results in [102] and in [100] for dense networks.

Nevertheless, despite the aforementioned works, characterising the wireless channel capacity from electromagnetic field point of view remains a challenge. First, such treatments as averaging the capacity over the coverage space fail to fully capture the spatial property of the wireless channel in the coverage space. Second, the works studied spatial degree-of-freedom(DoF) have been restricted to the discrete spatial DoFs and failed to address the wireless channel capacity from a continuous field perspective, which includes the radiating power of the electromagnetic field. To fully characterise the wireless channel capacity from electromagnetic field perspective, we need a new perspective to the problem.

In this work, we introduce a new wireless channel capacity definition characterising the continuous spatial property of the wireless channel. We define the wireless channel capacity of an enclosed volume space containing the transmitter. It is the first wireless channel capacity definition capturing spatial volume property of the wireless channel. Our new definition is based on the electromagnetic field, which considers the spatial property of the wireless field by nature. At the same time, our new definition takes the electromagnetic radiating power into account at the same time, which gives an accurate characterisation of the wireless channel capacity from electromagnetic perspective.

We choose two different shapes and four different sources to demonstrate the application of the new wireless capacity definition. The chosen settings are applications in wireless network performance evaluation. To calculate the capacity of the cube-shaped volume space, we give an alternative way to implement the calculation. Then, we present the analytical and numerical results of the capacity of wireless channel for the two shapes of volume space with 4 types of radiating sources, using the new wireless channel capacity. The results offer insight to the evaluation of wireless network capacity performance. This demonstrates that our new definition of the wireless channel capacity can play an important role in wireless network design and planning.

The rest of the chapter is organised as follows. Section 6.2 revisits the basic theory and concepts of the electromagnetic field channel capacity. Section 6.3 introduces the concept of capacity flow density and the new wireless channel capacity for enclosed volume space. Section 6.4 presents the total capacity of a sphere volume space. Section 6.6 gives an alternative method of calculating the new wireless channel capacity through the divergence theorem. Section 6.7 presents the total capacity results of the cube volume space. Section 6.8 gives the numerical results for the integral forms in Section 6.4 and Section 6.7. Section 6.9.3 concludes the chapter.

6.2 Channel Capacity and Electromagnetic Fundamentals

In this section, we first review the fundamentals of the additive white Gaussian noise (AWGN) channel capacity and then the fundamentals of electromagnetics.

6.2.1 AWGN Channel Capacity

The classic additive white Gaussian noise channel is widely adopted as the standard communication channel. The channel is based on a point-to-point channel model as illustrated in Figure 6.1.

The transmitter sends the information to the receiver. The channel has a Gaussian noise added to the received signal. The channel capacity defines the maximum error free transmission rate that the channel can achieve. The capacity of the AWGN channel is

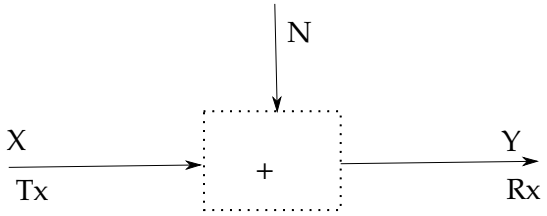

FIGURE 6.1: The Classical Point-to-point AWGN Channel Model

given in Shannon's classic paper [103] as:

$$C = \log_2(1 + \frac{P}{N}) \tag{6.1}$$

where C is the channel capacity; P is the received signal power and N is the noise power. The unit of the capacity is bits per second when the base of the logarithm is 2.

6.2.2 Electromagnetics Fundamentals

The propagation of the electromagnetic field is the medium for wireless channel. It is well known that the propagation of the electromagnetic field is governed by Maxwell's equations [75].

$$\begin{aligned} \vec{\nabla} \times \vec{E} &= -\frac{\partial \vec{B} d}{\partial t} \\ \vec{\nabla} \times \vec{B} &= \mu(\vec{J} + \epsilon \frac{\partial \vec{E}}{\partial t}) \\ \vec{\nabla} \cdot \vec{E} &= \frac{\rho}{\epsilon} \\ \vec{\nabla} \cdot \vec{B} &= 0 \end{aligned} \tag{6.2}$$

The 4 equations describe the 2 key components of the electromagnetic field propagation: the electrical field $\vec{E}$ and the magnetic field $\vec{B}$. The first equation is Maxwell-Faraday law and the second equation is Ampere's law. These two equations together describe the spatial temporal relationship of the electrodynamics. The identity $\vec{E}$ is the electrical field and $\vec{B}$ is the magnetic field. They are two vector fields forming the electromagnetic field. The parameters ϵ and μ are the permittivity and permeability of the media. The last two equations describe the electrostatic field and magnetostatic field. The parameter ρ is the local electric charge density. The operator $\vec{\nabla}\times$ denotes the curl operator; the operator $\vec{\nabla}\cdot$ denotes the divergence operator.

The power of the electromagnetic field is characterised by the Poynting vector:

$$\vec{S} = \vec{E} \times \vec{H} = \frac{1}{\mu_0}\vec{E} \times \vec{B} \tag{6.3}$$

The Poynting vector is defined as the power flow density. It quantifies the power flux flowing through a unit surface area in the field. By the definition of the Poynting vector it is straightforward to have the power flow through a unit area surface in the field as:

$$P = \vec{S} \cdot d\vec{a} \tag{6.4}$$

where $\cdot$ denotes the vector multiplication of the two vectors and $d\vec{a}$ is the infinitesimal surface area.

6.3 Capacity Flow Density

In this section, we introduce the concept of capacity flow density based on electromagnetics and channel capacity. We also derive the propagation of the the capacity flow density field, which is similar to electromagnetic field. We also apply the concept of capacity flow density to define a new channel capacity for the wireless channel.

6.3.1 Capacity Flow Density Definition

The AWGN channel capacity is defined on the point-to-point channel model. The communication channel is between a pair of transmitter and receiver. From the channel capacity perspective, the physical size and dimension of both the transmitter and receiver are not relevant to the study of the channel capacity from the point-to-point channel model. The transmitter and the receiver are treated as single points of receiver and transmitter while the physical size and dimension are neglected. On the other hand, in electromagnetics, the wireless channel is studied from a physical electromagnetic waves and fields. The physical size and dimension have to be taken into account.

To study the channel capacity from an electromagnetic perspective, we need to make an assumption for the communication channel. We assume an infinitely small receiver such that the receiver can be seen as an ideal point from a mathematical point of view. By placing such a 'point receiver' at each point in the electromagnetic field, therefore we have a 'receiver field'. Such an assumption connects the point-to-point channel model from information theory to the electromagnetic field. Under this assumption, each point in the electromagnetic field can be seen as a receiver as in the classic AWGN communication channel model. When we assume that the noise power is identically independent distributed AWGN, we have a definition of the capacity flow density field as: In a Cartesian coordinate system, where the power flow density is given as:

$$\vec{S} = S_i\vec{i} + S_j\vec{j} + S_k\vec{k} \tag{6.5}$$

The capacity flow density field is defined based on the power flow density field as:

$$\vec{C} = \log_2(1 + \frac{S_i}{N})\vec{i} + \log_2(1 + \frac{S_j}{N})\vec{j} + \log_2(1 + \frac{S_k}{N})\vec{k} \tag{6.6}$$

Similarly, in spherical coordinate system, the capacity flow density is given as:

$$\vec{C} = \log_2(1 + \frac{S_r}{N})\vec{r} + \log_2(1 + \frac{S_\theta}{N})\vec{\theta} + \log_2(1 + \frac{S_\phi}{N})\vec{\phi} \tag{6.7}$$

where S_r, S_θ and §$_\phi$ are the 3 vector components at the directions $\vec{r}$, $\vec{\theta}$ and $\vec{\phi}$.

Our assumption of infinitely small receivers and a continuous receiver field is similar to the assumption made in a recent work of [104]. The work assumed an infinite number of receivers placed in the receiving surface and studied the channel capacity under such a limiting condition. Our perspective is also related to the early work of [96], in which the authors pointed out that the total spatial degree-of-freedom of a MIMO system is limited by the minimum of the transmitter angle or the receiver solid angle. This result showed that the total spatial degree of freedom is bounded by the continuous total degree of the antenna aperture angle provided that the antenna is capable to resolve the spatial angle. Our definition of capacity flow density steps further to remove the constraints of antenna array and path independence to study the channel capacity on a continuous electromagnetic field. By introducing the concept of capacity flow density,

we avoid the complexity of tracing the discrete spatial independent paths and treat the whole spatial property channel as a continuous electromagnetic field. In this way, the continuous electromagnetic field has been extended to incorporate the discrete point-to-point channel model in a form of continuous receiver field

6.3.2 Capacity Flow Density Application: Surface Capacity

The definition of the capacity flow density in (6.6) and (6.7) shows that the capacity flow density has a similar property to power flow density. It characterises the capacity vector flowing through an infinitesimally small area in the field. Thus, the total amount of capacity flowing through a surface area is given as:

$$C_S = \vec{C} \cdot \vec{S} \tag{6.8}$$

where C_S is the total capacity; and $\vec{S}$ is the surface area vector.

This relationship reveals a new definition for the wireless channel capacity from electromagnetic perspective. The classic point-to-point channel model treating the receiver as a point by neglecting the physical size and dimension of the receiver. This definition of channel capacity shows that the surface area of the receiver has a definitive influence on the wireless channel capacity. Although this channel capacity definition offers a new perspective to see the wireless channel capacity, it is not straightforward to apply this definition in application. We will develop another wireless channel capacity characterisation in the following section.

6.3.3 A New Definition of Wireless Communication Channel Capacity

In many wireless system designs, the design environment and the volume of space of the environment is determined. In such cases, we can introduce a new wireless channel capacity for an enclosed volume space containing the radiating source.

Following the definition of the wireless channel capacity in (6.8), we define a new wireless channel capacity as:

Definition 6.1. The total capacity of an enclosed volume space containing the radiating source is given as:

$$C = \oiint_{\mathcal{S}} \vec{C} \cdot \vec{S} \tag{6.9}$$

where $\mathcal{S}$ is the surface of the enclosed volume space.

This new definition of total capacity characterises the spatial channel capacity of an enclosed volume space. In the following sections, we will study the total capacity of enclosed volume space of two shapes and with various radiating sources.

6.4 Total Capacity of A Sphere

In this section, we study the total capacity of a sphere shaped volume space. We first calculate the total capacity of a sphere with the source at the centre of the sphere. And then we calculate the total capacity of a sphere with the source at a non centre location.

6.4.1 Total Capacity with A Central Source

In this section, the total capacity of a sphere shaped volume space is calculated, under 4 types of radiating sources at the centre of the sphere. The 4 types of radiating sources include, a half wavelength dipole antenna, a 2-element linear array with half wavelength dipole antenna, a 4-element linear array with half wavelength dipole antenna and an isotropic source. We calculate the total capacity for each type of these sources in the following.

6.4.1.1 Total Capacity of A Sphere with Half Wavelength Dipole Antenna

We calculate the total capacity of a sphere with a half wavelength dipole antenna. First in the spherical coordinate system the far electrical field of a half wavelength dipole is given as [105]:

$$E_\theta = j\omega\mu \frac{2I}{\beta} \frac{e^{-j\beta r}}{4\pi r} \frac{\cos(\frac{\pi}{2}\cos\theta)}{\sin\theta} \hat{\theta} \tag{6.10}$$

The far magnetic field of the half wavelength dipole is given as:

$$H_\phi = \frac{j\omega\mu}{\eta}\frac{2I}{\beta}\frac{e^{-j\beta r}}{4\pi r}\frac{\cos(\frac{\pi}{2}\cos\theta)}{\sin\theta}\hat{\phi} \tag{6.11}$$

Replacing the above two fields into the definition of Poynting vector, we have the complex Poynting vector as

$$\begin{aligned} S &= E \times H^* \\ &= E_\theta \times H_\phi^* \\ &= \frac{\eta I^2}{4\pi^2 r^2}\frac{\cos^2(\frac{\pi}{2}\cos\theta)}{\sin^2\theta}\hat{r} \end{aligned} \tag{6.12}$$

where H^* represents the complex conjugate of the H field.

Thus the time average Poynting vector is given as

$$\begin{aligned} \overline{S} &= \frac{1}{2}S \\ &= \frac{\eta I^2}{8\pi^2 r^2}\frac{\cos^2(\frac{\pi}{2}\cos\theta)}{\sin^2\theta}\hat{r} \end{aligned} \tag{6.13}$$

where η is the wave impedance of the medium. Replacing this Poynting vector into the definition of capacity flow density in (6.7), we have the capacity flow density of the half wavelength dipole as:

$$\vec{C} = \log_2\left(1 + \frac{\eta I^2}{8\pi^2 N r^2}\frac{\cos^2(\frac{\pi}{2}\cos\theta)}{\sin^2\theta}\right)\hat{r} \tag{6.14}$$

Therefore, using the capacity flow density given in (6.14) to calculate the total capacity of a sphere as in (6.9), we have the total capacity as:

$$
\begin{aligned}
C &= \oiint_{\mathcal{S}} \vec{C} \cdot d\vec{s} \\
&= \oiint_{\mathcal{S}} \log_2 \left(1 + \frac{\eta I^2}{8\pi^2 N r^2} \frac{\cos^2(\frac{\pi}{2}\cos\theta)}{\sin^2\theta}\right) \hat{r} \cdot d\vec{s} \\
&= \int_0^{2\pi} \int_0^{\pi} \log_2 \left(1 + \frac{\eta I^2}{8\pi^2 N r^2} \frac{\cos^2(\frac{\pi}{2}\cos\theta)}{\sin^2\theta}\right) r^2 \sin^2\theta d\theta d\phi \\
&= 2\pi r^2 \int_0^{\pi} \log_2 \left(1 + \frac{\eta I^2}{8\pi^2 N r^2} \frac{\cos^2(\frac{\pi}{2}\cos\theta)}{\sin^2\theta}\right) \sin\theta d\theta
\end{aligned} \tag{6.15}
$$

where $\mathcal{S}$ denotes the surface of the sphere.

The above equation is the total capacity of a sphere with a half wavelength dipole at the centre. As the integral in the equation does not have a simple closed form, we resort to numerical integration to obtain the results. We calculate the total capacity of sphere with other types of sources in this section before we present the numerical integration results in Section 6.8.

6.4.1.2 Total Capacity of a Sphere with 2-element Linear Array

In this section, we consider a uniform linear array antenna as the radiating source and calculate the total capacity of a sphere. The linear array we consider is a 2-element array. Each element is a half wavelength dipole antenna with one wavelength apart.

According to the array multiplication principle [105], the E field and H field of the array are the E field and H field of the element antenna multiplied by the array factor. Thus, the fields can be written as:

$$E_{array} = E_{single} f(\theta, \phi) \tag{6.16}$$

$$H_{array} = H_{single} f(\theta, \phi) \tag{6.17}$$

where $f(\theta, \phi)$ is the normalised array factor; E_{array} and H_{array} are the fields of the array antenna and E_{single} and H_{single} are the fields of the element antenna.

We assume a simple 2-element array with one wavelength apart. Thus, the array factor is given as [105] :

$$f(\theta)_{2element} = \cos(\pi \cos\theta) \tag{6.18}$$

We assume a 2-element array antenna with each element a half wavelength dipole antenna. With the fields of the element of half wavelength dipole given in (6.10) and (6.11), we the fields of the 2-element half wavelength dipole array antenna as:

$$E_{2element} = j\omega\mu \frac{2I}{\beta} \frac{e^{-j\beta r}}{4\pi r} \frac{\cos(\frac{\pi}{2}\cos\theta)}{\sin\theta} \cos(\pi\cos\theta)\hat{\theta} \tag{6.19}$$

$$H_{2element} = \frac{j\omega\mu}{\eta} \frac{2I}{\beta} \frac{e^{-j\beta r}}{4\pi r} \frac{\cos(\frac{\pi}{2}\cos\theta)}{\sin\theta} \cos(\pi\cos\theta)\hat{\phi} \tag{6.20}$$

With the field values, we have the capacity flow density of the 2-element array as:

$$\vec{C}_{2element} = \log_2\left(1 + \frac{\eta I^2}{8\pi^2 N r^2} \frac{\cos^2(\frac{\pi}{2}\cos\theta)\cos^2(\pi\cos\theta)}{\sin^2\theta}\right)\hat{r} \tag{6.21}$$

Thus the total capacity follows as:

$$\begin{aligned} C_{2element} &= \oiint \vec{C}_{2element} \cdot d\vec{s} \\ &= 2\pi r^2 \int_0^{\pi} \log_2\left(1 + \frac{\eta I^2}{8\pi^2 N r^2} \frac{\cos^2(\frac{\pi}{2}\cos\theta)\cos^2(\pi\cos\theta)}{\sin^2\theta}\right)\sin\theta d\theta \end{aligned} \tag{6.22}$$

Again the total capacity is an integral form.

6.4.1.3 4-element array

To further see the effects of the array antenna, we adopt a 4-element uniform linear array antenna with each element a half wavelength dipole antenna. The distance between each element is one wavelength. The array geometry is shown in Figure 6.2.

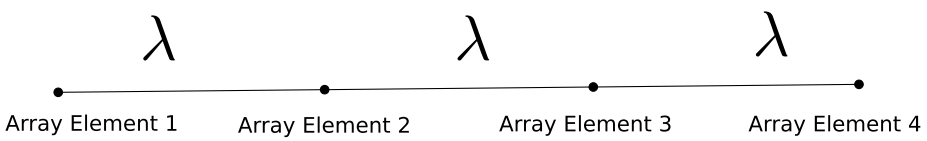

FIGURE 6.2: Array Geometry of a 4-element Uniform Linear Array

Following the array multiplication principle in [105], the total array factor is written as:

$$AF = Ie^{j\beta\frac{d}{2}\cos\theta} + Ie^{-j\beta\frac{d}{2}\cos\theta} + Ie^{j\beta\frac{3d}{2}\cos\theta} + Ie^{-j\beta\frac{3d}{2}\cos\theta} \tag{6.23}$$

where d is the distance between the array elements. In our case, $d = \lambda$.

The array factor can be further simplified and normalised. The normalised array factor is given as:

$$f(\theta)_{4element} = \cos(\pi\cos\theta)\cos(2\pi\cos\theta) \tag{6.24}$$

Again, using this array factor, we have the capacity flow density of the array as:

$$\vec{C}_{4element} = \log_2\left(1 + \frac{\eta I^2}{8\pi^2 N r^2}\frac{\cos^2(\frac{\pi}{2}\cos\theta)\cos^2(\pi\cos\theta)\cos^2(2\pi\cos\theta)}{\sin^2\theta}\right)\hat{r} \tag{6.25}$$

And the total capacity is:

$$C_{4element} = \oiint \vec{C}_{4element}\cdot d\vec{s} \tag{6.26}$$

$$= 2\pi r^2\int_0^\pi \log_2\left(1 + \frac{\eta I^2}{8\pi^2 N r^2}\frac{\cos^2(\frac{\pi}{2}\cos\theta)\cos^2(\pi\cos\theta)\cos^2(2\pi\cos\theta)}{\sin^2\theta}\right)\sin\theta d\theta \tag{6.27}$$

6.4.1.4 Total Capacity of An Isotropic Source

For comparison purpose, we also look into the total capacity of an isotropic radiating source. An isotropic source is a source that radiates power uniformly in all the spatial

directions. It is an idealised radiating source. It is used as a basis for comparing the radiation performance of a specific antenna.

We first compute the power flow density of an isotropic source which has the same total radiating power as a half wavelength dipole antenna.

With the Poynting vector given in (6.12), the total radiating power of a half wavelength dipole antenna is given as:

$$\begin{aligned} P_t &= \oiint_S \vec{S} \cdot d\vec{s} \\ &= \int_0^{\pi} \frac{\eta I^2}{2\pi} \frac{\cos^2(\frac{\pi}{2}\cos\theta)}{\sin\theta} d\theta \end{aligned} \tag{6.28}$$

Following the assumption that the isotropic source radiating the power uniformly into all the spatial direction, the power flow density is given as the total radiating power averaged over a uniform sphere. Thus, it is given as:

$$\begin{aligned} \vec{S}_{iso} &= \frac{P_t}{4\pi r^2}\vec{r} \\ &= \int_0^{\pi} \frac{\eta I^2}{8\pi^2 r^2} \frac{\cos^2(\frac{\pi}{2}\cos\theta)}{\sin\theta} d\theta\vec{r} \end{aligned} \tag{6.29}$$

The integral result of the equation

$$\int_0^{\pi} \frac{\cos^2(\frac{\pi}{2}\cos\theta)}{\sin\theta} d\theta = \frac{1}{2}(-C_i(2\pi) + \gamma + \ln(2\pi)) \tag{6.30}$$

where $C_i(*)$ is the cosine integral function and γ is the Euler-Mascheroni constant. Thus, the final result of the above integral is:

$$\int_0^{\pi} \frac{\cos^2(\frac{\pi}{2}\cos\theta)}{\sin\theta} d\theta \approx 1.2188 \tag{6.31}$$

Thus the Poynting vector of the isotropic source can be written as:

$$\vec{S}_{iso} = 0.6094 \frac{\eta I^2}{4\pi^2 r^2} \vec{r} \tag{6.32}$$

This is the power flow density vector of an isotropic source which has the same amount of radiating power P_t as the half wavelength dipole. We will use this equivalent power isotropic antenna to compare with other realistic radiation sources.

Following the definition of the capacity flow density, we replace (6.32) to the definition of capacity flow density. The resulting capacity flow density of an isotropic source is thus written as:

$$\vec{C}_{iso} = \log_2 \left(1 + 0.6094 \frac{\eta I^2}{4\pi^2 r^2 N} \right) \vec{r} \tag{6.33}$$

Similarly, using this capacity flow density, the total capacity of the isotropic source is thus given as:

$$\begin{aligned} C_{iso} &= \oiiint_S \vec{C}_{iso} \cdot ds \\ &= 4\pi r^2 \log_2 \left(1 + 0.6094 \frac{\eta I^2}{4\pi^2 r^2 N} \right) \end{aligned} \tag{6.34}$$

Until now, we have the integral forms of total capacity of a sphere of 4 types of sources: half wavelength dipole; 2-element dipole array; 4-element linear dipole array and equivalent isotropic source. However, the results involve complex integral forms. We will present numerical integral results in the next section.

6.4.2 Total Capacity of Sphere with A Non-central Source

It is an ideal assumption that the radiating source is always at the centre of the sphere. In this section, we calculate the total capacity of a sphere shape volume space when the radiating source is not at the centre of the sphere. We study the influence of the location of the source inside the sphere has on the total capacity of the sphere.

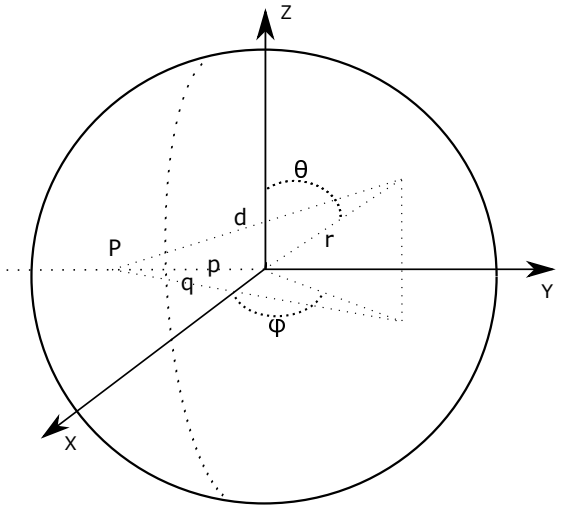

FIGURE 6.3: Geometry of a Sphere with a Non-centre Source

First we assume the location of the source is at the location $(p, 0, 0)$ in the spherical coordinate system. The sphere has the origin as the location $(0, 0, 0)$. The geometry is illustrated in Figure 6.3.

Based on the geometry in Figure 6.3, we have the following relationship:

$$d^2 = r^2 \cos^2 \theta + q^2$$

where d is the distance from the source to a certain point on the sphere surface; r is the radius of the sphere; and q is given in the following equation according to the according to the law of cosine.

$$q^2 = p^2 + r^2 \sin^2 \theta + 2pr \sin \theta \sin \phi \tag{6.35}$$

Thus, we obtain the distance from the source at $(p, 0, 0)$ to a certain point on the sphere surface as:

$$d = \sqrt{r^2 + p^2 + 2rp \sin \theta \sin \phi} \tag{6.36}$$

Then we replace this distance into the capacity flow density in (6.14), (6.21), (6.25) and (6.33), we have the capacity flow density with the radiating source at the location of $(p, 0, 0)$ for the 4 types of sources that we have derived for centre location as:

$$\vec{C} = \log_2\left(1 + \frac{\eta I^2}{8\pi^2 N(r^2 + p^2 + 2rp\sin\theta\sin\phi)}\frac{\cos^2(\frac{\pi}{2}\cos\theta)}{\sin^2\theta}\right)\hat{r} \tag{6.37}$$

$$\vec{C}_{2element} = \log_2\left(1 + \frac{\eta I^2}{8\pi^2 N(r^2 + p^2 + 2rp\sin\theta\sin\phi)}\frac{\cos^2(\frac{\pi}{2}\cos\theta)\cos^2(\pi\cos\theta)}{\sin^2\theta}\right)\hat{r} \tag{6.38}$$

$$\vec{C}_{4element} = \log_2\left(1 + \frac{\eta I^2}{8\pi^2 N(r^2 + p^2 + 2rp\sin\theta\sin\phi)}\frac{\cos^2(\frac{\pi}{2}\cos\theta)\cos^2(\pi\cos\theta)\cos^2(2\pi\cos\theta)}{\sin^2\theta}\right)\hat{r} \tag{6.39}$$

$$\vec{C}_{iso} = \log_2\left(1 + 0.6094\frac{\eta I^2}{4\pi^2 N(r^2 + p^2 + 2rp\sin\theta\sin\phi)}\right)\vec{r} \tag{6.40}$$

The four equations in (6.37), (6.38), (6.39) and (6.40) are the capacity flow density for the half wavelength dipole, 2-element dipole array, 4-element linear dipole array and the equivalent isotropic source, respectively, with the source located at $(p, 0, 0)$.

Thus, by integrating the capacity flow density over the sphere surface, we have the total capacity of the sphere with the source at the location of $(p, 0, 0)$ as:

$$C(r,p)_{dipole} = \int_0^{2\pi}\int_0^{\pi}\log_2\left(1 + \frac{\eta I^2}{8\pi^2 N(r^2 + p^2 + 2rp\sin\theta\sin\phi)}\frac{\cos^2(\frac{\pi}{2}\cos\theta)}{\sin^2\theta}\right)r^2\sin^2\theta d\theta d\phi \tag{6.41}$$

$$C(r,p)_{2element} = \int_0^{2\pi}\int_0^{\pi}\log_2(1 + \frac{\eta I^2}{8\pi^2 N(r^2 + p^2 + 2rp\sin\theta\sin\phi)} \frac{\cos^2(\frac{\pi}{2}\cos\theta)\cos^2(\pi\cos\theta)}{\sin^2\theta})r^2\sin^2\theta d\theta d\phi \tag{6.42}$$

$$C(r,p)_{4element} = \int_0^{2\pi}\int_0^{\pi} \log_2(1 + \frac{\eta I^2}{8\pi^2 N(r^2+p^2+2rp\sin\theta\sin\phi)} \frac{\cos^2(\frac{\pi}{2}\cos\theta)\cos^2(\pi\cos\theta)\cos^2(2\pi\cos\theta)}{\sin^2\theta})r^2\sin^2\theta d\theta d\phi \quad (6.43)$$

$$C_{iso} = \int_0^{2\pi}\int_0^{\pi} \log_2\left(1 + 0.6094\frac{\eta I^2}{4\pi^2 N(r^2+p^2+2rp\sin\theta\sin\phi)}\right) r^2\sin^2\theta d\theta d\phi \quad (6.44)$$

The above 4 equations in (6.41), 6.42), (6.43) and (6.44) are the total capacity calculation equations of the half wavelength dipole antenna, the 2-element dipole antenna array, the 4-element dipole antenna array and the equivalent isotropic source, respectively, with the location at $(p,0,0)$. We write the total capacity as a function of both the sphere radius r and the shift from the origin p. Again, the total capacity involves an integral form. The numerical integral results are presented in Section 6.8.

6.5 Properties of Capacity of A Sphere

We have derived the integral forms of the total capacity of 4 types of sources both at the centre location and the non-centre location of the sphere. The numerical integral results will be presented in Section 6.8. However, we have two important general results concerning the total capacity of sphere.

The first property is a general result of the total capacity of sphere concerning the antenna types.

Proposition 6.2. *Among the sources placed at the centre of the sphere, the isotropic radiating source has the maximum total capacity.*

Proof. For simplicity we can write the Poynting vector of an arbitrary source as in [105]:

$$U(\theta,\phi) = D(\theta,\phi)U_{ave} \quad (6.45)$$

where $D(\theta, \phi)$ is the directive gain; U_{ave} is the radiating intensity of an isotropic source and $U(\theta, \phi)$ is the radiating intensity defined as:

$$U(\theta, \phi) = \vec{S} \cdot r^2 \vec{r} \tag{6.46}$$

Replacing (6.46) into (6.45), we have the Poynting vector as:

$$\vec{S} = D(\theta, \phi)\vec{S}_{ave} \tag{6.47}$$

where $\vec{S}_{ave}$ is the Poynting vector of an isotropic source defined as:

$$\vec{S}_{ave} = \frac{P_r}{4\pi r^2}\vec{r} \tag{6.48}$$

Therefore, following the capacity flow density in (6.7), we have the capacity flow density as:

$$\vec{C} = \log_2\left(1 + \frac{P_r D(\theta, \phi)}{4\pi N r^2}\right)\vec{r} \tag{6.49}$$

and the total capacity as:

$$C = 2\pi r^2 \int_0^{\pi} \log_2\left(1 + \frac{P_r D(\theta, \phi)}{4\pi N r^2}\right) \sin\theta d\theta \tag{6.50}$$

Under the condition that the directive gain is between 0 and 1:

$$0 \leqslant D(\theta, \phi) \leqslant 1$$

, we obtain the maximum of the the total capacity in (6.50) when $D(\theta, \phi) = 1$ for all the spatial angle of θ which is equivalent to isotropic radiation as:

$$\begin{aligned} C &= 2\pi r^2 \int_0^{\pi} \log_2 \left(1 + \frac{P_r D(\theta,\phi)}{4\pi N r^2}\right) \sin\theta d\theta \\ &\leqslant 2\pi r^2 \int_0^{\pi} \log_2 \left(1 + \frac{P_r}{4\pi N r^2}\right) \sin\theta d\theta \\ &= 4\pi r^2 \log_2 \left(1 + \frac{P_r}{4\pi N r^2}\right) \\ &= C_{iso} \end{aligned} \tag{6.51}$$

This concludes the proof.

□

The second property is concerning the location of the source in a sphere. We have the following proposition:

Proposition 6.3. *For a source at a distance shift p from the origin of the sphere, among the distance shifts p, where $0 \leqslant p \leqslant r$, when $p = 0$, which means the source is at the centre of the sphere, the total capacity has the maximum value.*

Proof. Replacing the geometry relation in (6.36) into the total capacity in (6.50), we have the total capacity as a function of p as:

$$C(p) = 2\pi r^2 \int_0^{\pi} \log_2 \left(1 + \frac{P_r D(\theta,\phi)}{4\pi N(r^2 + p^2 + 2pr\cos\theta)}\right) \sin\theta d\theta \tag{6.52}$$

Taking derivative of the function $C(p)$ we have:

$$\begin{aligned} \frac{dC(p)}{dp} &= \frac{d}{dp}\left(\log_2 \left(1 + \frac{P_r D(\theta,\phi)}{4\pi N(r^2 + p^2 + 2pr\cos\theta)}\right) \sin\theta d\theta\right) \\ &= -2\pi r^2 \int_0^{\pi} \frac{(2p + 2r\cos\theta) P_r D(\theta,\phi)}{4\pi N(r^2 + p^2 + 2pr\cos\theta)^2 + P_r D(\theta,\phi)(r^2 + p^2 + 2pr\cos\theta)} d\theta \end{aligned} \tag{6.53}$$

The condition to find the maximum value of function $C(p)$ is to set the derivative of $C(p)$ as zero :

$$\frac{dC(p)}{dp} = 0$$

.

Thus, by setting the capacity derivative in (6.53) as zero, we have the following condition:

$$p = -r\cos\theta \tag{6.54}$$

Under the condition that p is a non-negative value; and r is a non-zero value, with $0 \leqslant \theta \leqslant \pi$, the value to achieve the condition in (6.54) is $\cos\theta = 0$, which results in $p = 0$.

This concludes the proof. □

6.6 Calculating the Total Capacity using Divergence

The total capacity of an enclosed volume space is defined as the total capacity flow density flux flowing through the enclosed surface. Following this definition, we have calculated the capacity of a sphere shape volume capacity containing a radiating source in the last section. However, in applications the shape of the volume space is not a perfect sphere, which leads to difficulty in deriving the integral form of the total capacity. In this section, we present an alternative method of calculating the total capacity of an enclosed volume space by applying the divergence theorem to the definition of the total capacity.

The total capacity of an enclosed volume space is defined as the total capacity flow density flux flowing through the total surface area in (6.9).

Under the assumption that the volume space is enclosed, applying the divergence thorem to this definition, we arrive at:

$$\oiint_{\mathcal{S}} \vec{C} \cdot d\vec{s} = \iiint_{\mathcal{V}} (\nabla \cdot \vec{C}) dv \tag{6.55}$$

where $\nabla \cdot \vec{C}$ is the divergence of the capacity flow density.

This equation provides an alternative method of calculating the total capacity of an enclosed volume space via calculating the divergence of the capacity flow density. While divergence of the capacity flow density is crucial in applying this method, we first study the divergence of the capacity flow density with the 4 types of sources we have used in Section 6.4.

6.6.1 Divergence of Various Sources

As the divergence of the capacity flow density field is the key to use the divergence theorem to calculate the total capacity, we first compute the divergence of various sources in this section.

6.6.1.1 Divergence of Half Wavelength Dipole Antenna

The capacity flow density of the half wavelength dipole is given in (6.14). Following the definition of divergence of a vector A in spherical coordinate system as [106]:

$$\nabla \cdot \vec{A} = \frac{1}{r^2}\frac{\partial}{\partial r}(r^2 A_r) + \frac{1}{r\sin\theta}\frac{\partial}{\partial \theta}(\sin\theta A_\theta) + \frac{1}{r\sin\theta}\frac{\partial A_\phi}{\partial \phi} \tag{6.56}$$

where A_r, A_θ and A_ϕ are the three vector components of vector A in the spherical coordinate system. For the capacity flow density in our case, the capacity flow density in the far field only has a component in the $\vec{r}$ direction. Thus the divergence of the capacity flow density is given as:

$$\begin{aligned} \nabla \cdot \vec{C} &= \frac{1}{r^2}\frac{\partial}{\partial r}(r^2 C_r) \\ &= \frac{1}{r^2}(2rC_r + r^2\frac{\partial C_r}{\partial r}) \\ &= \frac{2C_r}{r} + \frac{\partial C_r}{\partial r} \end{aligned} \tag{6.57}$$

where C_r is the capacity flow density in the $\vec{r}$ direction.

We use this equation in the calculation of the divergence of capacity flow density of various sources. Applying the above (6.57) to the capacity flow density of the 4 types

of the sources in (6.14), (6.21), (6.25) and (6.33), we have the divergence of the capacity flow density of the 4 types of sources as:

$$\nabla \cdot \vec{C}_{dipole} = \frac{2}{r}\log_2\left(1 + \frac{\eta I^2}{4\pi^2 r^2 N}\frac{\cos^2(\frac{\pi}{2}\cos\theta)}{\sin^2\theta}\right) - \frac{2\eta\frac{I^2}{N}\cos^2(\frac{\pi}{2}\cos\theta)}{4\pi^2 r^3\sin^2\theta + \eta\frac{I^2}{N}r\cos^2(\frac{I^2}{N}\cos\theta)} \tag{6.58}$$

$$\nabla \cdot \vec{C}_{2element} = \frac{2}{r}\log_2\left(1 + \frac{\eta I^2}{4\pi^2 r^2 N}\frac{\cos^2(\frac{\pi}{2}\cos\theta)\cos^2(\pi\cos\theta)}{\sin^2\theta}\right) - \frac{2\eta\frac{I^2}{N}\cos^2(\frac{\pi}{2}\cos\theta)\cos^2(\pi\cos\theta)}{4\pi^2 r^3\sin^2\theta + \eta\frac{I^2}{N}r\cos^2(\frac{I^2}{N}\cos\theta)\cos^2(\pi\cos\theta)} \tag{6.59}$$

$$\nabla \cdot \vec{C}_{4element} = \frac{2}{r}\log_2\left(1 + \frac{\eta I^2}{4\pi^2 r^2 N}\frac{\cos^2(\frac{\pi}{2}\cos\theta)\cos^2(\pi\cos\theta)\cos^2(2\pi\cos\theta)}{\sin^2\theta}\right) - \frac{2\eta\frac{I^2}{N}\cos^2(\frac{\pi}{2}\cos\theta)\cos^2(\pi\cos\theta)\cos^2(2\pi\cos\theta)}{4\pi^2 r^3\sin^2\theta + \eta\frac{I^2}{N}r\cos^2(\frac{I^2}{N}\cos\theta)\cos^2(pi\cos\theta)\cos^2(2\pi\cos\theta)} \tag{6.60}$$

$$\nabla \cdot \vec{C}_{isotropic} = \frac{2}{r}\log_2\left(1 + 0.6094\frac{\eta I^2}{4\pi^2 r^2 N}\right) - \frac{1.288\eta\frac{I^2}{N}}{4\pi^2 r^3\sin^2\theta + 0.6094\eta\frac{I^2}{N}r} \tag{6.61}$$

The above divergence results in (6.58), (6.59), (6.60) and (6.61) are the divergence of capacity flow density of half wavelength dipole antenna, 2-element dipole array, 4-element dipole uniform linear array and the equivalent isotropic source, respectively. Except the isotropic source, the divergence of the rest 3 sources depends on both the distance r and the angle θ. We plot the divergence of the half wavelength dipole in Figure 6.4 as a 3D surface as a function of both the distance r and the angle θ, where the $\frac{I^2}{N} = 5$.

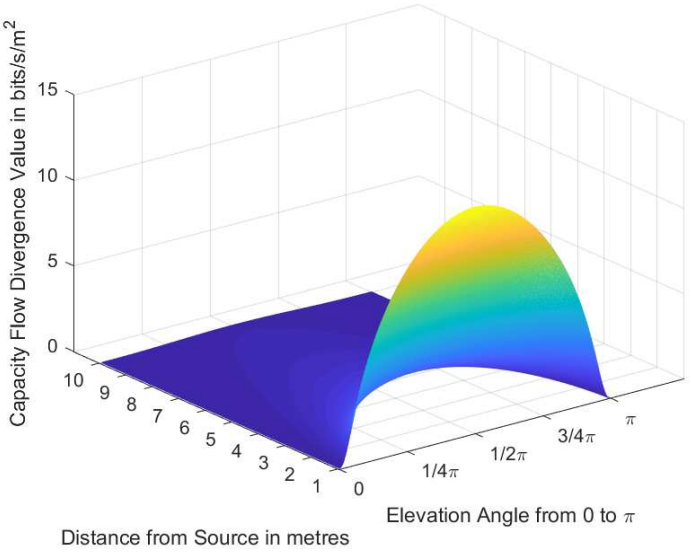

FIGURE 6.4: 3D Plot of the Divergence of a Half-wavelength Dipole Antenna

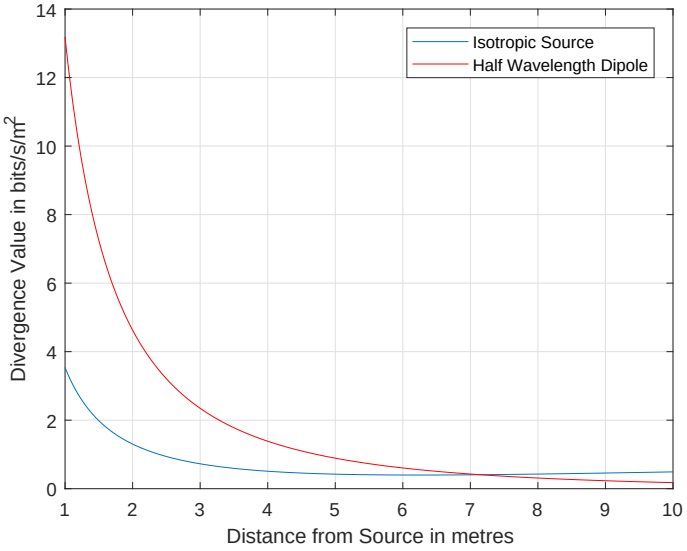

FIGURE 6.5: Divergence Values of Half-wavelength Dipole and Isotropic Source when $\theta = 0$

In Figure 6.5, we plot the divergence of all the 4 types of source against the distance r by fixing the angle $\theta = 0$.

From both Figure 6.4 and Figure 6.5, we see that the divergence of the capacity flow density is a function of the distance r. After dropping from the peak near the source, it still extends with the distance fairly far from the source. If we see the divergence of the capacity flow density as a 'source' of the capacity, then this explains the total capacity increase with the volume space as the 'source' extends with the distance extends. In the

next section, we use the divergence of the capacity flow density to calculate the total capacity of an enclosed volume space of cube shape.

6.7 Total Capacity of A Cube

In Section 6.4 we calculated the total capacity of an enclosed volume space of perfect sphere shape. However, in practical applications, it is rare that the interested design space is a perfect sphere. For example, in indoor wireless network design, the shape of indoor rooms is often cuboid. To gain an insight of the influence of the shape of the volumes space on the total capacity, in this section, we calculate the total capacity of a cube shaped volume space. Different from the sphere shaped volume space, where the integral of capacity flow density is performed over the perfect sphere shape, the irregularity of the cube surface leads to difficulty in obtaining the integral form of the capacity flow density over the cube surface. Therefore, we resort to the method of divergence introduced in Section 6.6 to calculate the total capacity of a cube. Similar to the sphere case, we also calculated the 4 types of sources at the centre of the cube and at the non-centre of the cube. We use the divergence of the 4 types of source computed in Section 6.6 to calculate the total capacity in this case.

6.7.1 Total Capacity of A Cube with Centre Source

In this section, we derive the mathematical form of the total capacity of a cube shaped enclosed volume space with the source at the centre of the cube.

We assume a cube with the edge length $2a$ with the original of the Cartesian coordinate system at the centre of the cube. The radiating source is also placed at the centre of the cube. The geometry is illustrated in Figure 6.6.

The divergence of the 4 types of source given in (6.58), (6.59), (6.60) and (6.61) are in the form of spherical coordinate system. In our calculation, it is desirable to convert to the Cartesian coordinate system to integral the cube volume space. The transformation from the spherical coordinate system to the Cartesian coordinate system utilises the following identities:

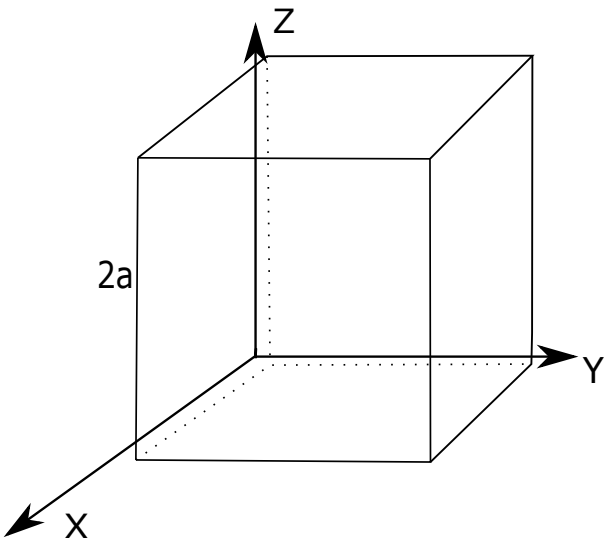

FIGURE 6.6: Geometry of Cube-Shaped Volume Space

$$r = \sqrt{x^2 + y^2 + z^2} \tag{6.62}$$

$$\cos\theta = \frac{z}{\sqrt{x^2 + y^2 + z^2}} \tag{6.63}$$

$$\sin\theta = \frac{\sqrt{x^2 + y^2}}{\sqrt{x^2 + y^2 + z^2}} \tag{6.64}$$

Replacing (6.64) in (6.58), (6.59), (6.60) and (6.61) yields the divergence of the 4 types of sources in the Cartesian coordinate system as:

$$D(x,y,z)_{dipole} = \frac{2}{\sqrt{x^2 + y^2 + z^2}} \log_2 \left(1 + \frac{\eta I^2 \cos^2(\frac{\pi}{2} \frac{z}{\sqrt{x^2+y^2+z^2}})}{4\pi^2 (x^2 + y^2) N} \right) - \frac{2\eta \frac{I^2}{N} \cos^2(\frac{\pi}{2} \frac{z}{\sqrt{x^2+y^2+z^2}})}{4\pi^2 (x^2 + y^2) \sqrt{x^2 + y^2 + z^2} + \eta \frac{I^2}{N} \sqrt{x^2 + y^2 + z^2} \cos^2(\frac{\pi}{2} \frac{z}{\sqrt{x^2+y^2+z^2}})} \tag{6.65}$$

$$D(x,y,z)_{2element} = \frac{2}{\sqrt{x^2 + y^2 + z^2}} \log_2 \left(1 + \frac{F(x,y,z)_{2element}}{4\pi^2 (x^2 + y^2)} \right) - \frac{2F(x,y,z)_{2element}}{4\pi^2 (x^2 + y^2) \sqrt{x^2 + y^2 + z^2} + F(x,y,z)_{2element}} \tag{6.66}$$

$$D(x,y,z)_{4element} = \frac{2}{\sqrt{x^2+y^2+z^2}} \log_2 \left(1 + \frac{F(x,y,z)_{4element}}{4\pi^2(x^2+y^2)}\right) - \frac{2F(x,y,z)_{4element}}{4\pi^2(x^2+y^2)\sqrt{x^2+y^2+z^2} + F(x,y,z)_{4element}} \tag{6.67}$$

$$D(x,y,z)_{isotropic} = \frac{2}{\sqrt{x^2+y^2+z^2}} \log_2 \left(1 + 0.6094\frac{\eta I^2}{4\pi^2(x^2+y^2+z^2)N}\right) - \frac{1.288\eta\frac{I^2}{N}}{4\pi^2(\sqrt{x^2+y^2+z^2})^3 + 0.6094\eta\frac{I^2}{N}\sqrt{x^2+y^2+z^2}} \tag{6.68}$$

where

$$F(x,y,z)_{2element} = \eta\frac{I^2}{N}\sqrt{x^2+y^2+z^2}\cos^2(\frac{\pi}{2}\frac{z}{\sqrt{x^2+y^2+z^2}})\cos^2(\pi\frac{z}{\sqrt{x^2+y^2+z^2}}) \tag{6.69}$$

$$F(x,y,z)_{4element} = \frac{\eta}{N}I^2\cos^2(\frac{\pi}{2}\frac{z}{\sqrt{x^2+y^2+z^2}})\cos^2(\pi\frac{z}{\sqrt{x^2+y^2+z^2}})\cos^2(2\pi\frac{z}{\sqrt{x^2+y^2+z^2}}) \tag{6.70}$$

The divergence values $D(x,y,z)$ in the above equations in (6.65), (6.66), (6.67) and (6.68) are written as a function of the Cartesian coordinate location (x,y,z) which represents the divergence at the location (x,y,z). Following the divergence method of calculating the total capacity in (6.55), we have the total capacity of the 4 types of sources as:

$$
\begin{aligned}
C_{dipole} &= \iiint_{\mathcal{V}} D(x,y,z)_{dipole}\,dv \\
&= \int_{-a}^{a}\int_{-a}^{a}\int_{-a}^{a} D(x,y,z)_{dipole}\,dxdydz \\
&= \int_{-a}^{a}\int_{-a}^{a}\int_{-a}^{a} \frac{2}{\sqrt{x^2+y^2+z^2}} \log_2\left(1+\frac{\eta I^2 \cos^2(\frac{\pi}{2}\frac{z}{\sqrt{x^2+y^2+z^2}})}{4\pi^2(x^2+y^2)N}\right) \\
&- \frac{2\eta\frac{I^2}{N}\cos^2(\frac{\pi}{2}\frac{z}{\sqrt{x^2+y^2+z^2}})}{4\pi^2(x^2+y^2)\sqrt{x^2+y^2+z^2}+\eta\frac{I^2}{N}\sqrt{x^2+y^2+z^2}\cos^2(\frac{\pi}{2}\frac{z}{\sqrt{x^2+y^2+z^2}})} dxdydz
\end{aligned}
\tag{6.71}
$$

$$
\begin{aligned}
C_{2element} &= \iiint_{\mathcal{V}} D(x,y,z)_{2element}\,dv \\
&= \int_{-a}^{a}\int_{-a}^{a}\int_{-a}^{a} D(x,y,z)_{2element}\,dxdydz \\
&= \int_{-a}^{a}\int_{-a}^{a}\int_{-a}^{a} \frac{2}{\sqrt{x^2+y^2+z^2}} \log_2\left(1+\frac{F(x,y,z)_{2element}}{4\pi^2(x^2+y^2)}\right) \\
&- \frac{2F(x,y,z)_{2element}}{4\pi^2(x^2+y^2)\sqrt{x^2+y^2+z^2}+F(x,y,z)_{2element}} dxdydz
\end{aligned}
\tag{6.72}
$$

$$
\begin{aligned}
C_{4element} &= \iiint_{\mathcal{V}} D(x,y,z)_{4element}\,dv \\
&= \int_{-a}^{a}\int_{-a}^{a}\int_{-a}^{a} D(x,y,z)_{4element}\,dxdydz \\
&= \int_{-a}^{a}\int_{-a}^{a}\int_{-a}^{a} \frac{2}{\sqrt{x^2+y^2+z^2}} \log_2\left(1+\frac{F(x,y,z)_{4element}}{4\pi^2(x^2+y^2)}\right) \\
&- \frac{2F(x,y,z)_{4element}}{4\pi^2(x^2+y^2)\sqrt{x^2+y^2+z^2}+F(x,y,z)_{4element}} dxdydz
\end{aligned}
\tag{6.73}
$$

$$
\begin{aligned}
C_{isotropic} &= \iiint_{\mathcal{V}} D(x,y,z)_{isotropic} dv \\
&= \int_{-a}^{a}\int_{-a}^{a}\int_{-a}^{a} D(x,y,z)_{isotropic} dxdydz \\
&= \int_{-a}^{a}\int_{-a}^{a}\int_{-a}^{a} \frac{2}{\sqrt{x^2+y^2+z^2}} \log_2\left(1 + 0.6094 \frac{\eta I^2}{4\pi^2(x^2+y^2+z^2)N}\right) \\
&- \frac{1.288\eta\frac{I^2}{N}}{4\pi^2(\sqrt{x^2+y^2+z^2})^3 + 0.6094\eta\frac{I^2}{N}\sqrt{x^2+y^2+z^2}} dxdydz
\end{aligned} \tag{6.74}
$$

The above equations in (6.71), (6.72), (6.73) and (6.74) give the total capacity of a cube shape with the half wavelength dipole, 2-element dipole array, 4-element uniform linear dipole array and the equivalent isotropic source, respective, all at centre of the cube. The results require multiple integrals. We will present the numerical integration results in the later section.

6.7.2 Total Capacity of Cube with Non-Centre Source

Same as the sphere shaped volume space case, we also calculate the total capacity of the cube with the sources at the non-centre location. We assume that the location of the source is shifted to the location of $(p, 0, 0)$ in Cartesian coordinate system. According to the total capacity results in a multiple integral form in (6.71), (6.72), (6.73) and (6.74), the total capacity of the source at $(p, 0, 0)$ results only a shift in one dimension of the integral limits from $\int_{-a}^{a}$ to $\int_{-a+p}^{a+p}$. Thus it is straightforward to have the following integral forms of the total capacity of the 4 types of sources at location $(p, 0, 0)$ as:

$$
\begin{aligned}
C_{dipole} &= \iiint_{\mathcal{V}} D(x,y,z)_{dipole} dv \\
&= \int_{-a}^{a}\int_{-a}^{a}\int_{-a+p}^{a+p} D(x,y,z)_{dipole} dxdydz \\
&= \int_{-a}^{a}\int_{-a}^{a}\int_{-a+p}^{a+p} \frac{2}{\sqrt{x^2+y^2+z^2}} \log_2\left(1+\frac{\eta I^2 \cos^2(\frac{\pi}{2}\frac{z}{\sqrt{x^2+y^2+z^2}})}{4\pi^2(x^2+y^2)N}\right) \\
&- \frac{2\eta\frac{I^2}{N}\cos^2(\frac{\pi}{2}\frac{z}{\sqrt{x^2+y^2+z^2}})}{4\pi^2(x^2+y^2)\sqrt{x^2+y^2+z^2}+\eta\frac{I^2}{N}\sqrt{x^2+y^2+z^2}\cos^2(\frac{\pi}{2}\frac{z}{\sqrt{x^2+y^2+z^2}})} dxdydz
\end{aligned}
\tag{6.75}
$$

$$
\begin{aligned}
C_{2element} &= \iiint_{\mathcal{V}} D(x,y,z)_{2element} dv \\
&= \int_{-a}^{a}\int_{-a}^{a}\int_{-a+p}^{a+p} D(x,y,z)_{2element} dxdydz \\
&= \int_{-a}^{a}\int_{-a}^{a}\int_{-a+p}^{a+p} \frac{2}{\sqrt{x^2+y^2+z^2}} \log_2\left(1+\frac{F(x,y,z)_{2element}}{4\pi^2(x^2+y^2)}\right) \\
&- \frac{2F(x,y,z)_{2element}}{4\pi^2(x^2+y^2)\sqrt{x^2+y^2+z^2}+F(x,y,z)_{2element}} dxdydz
\end{aligned}
\tag{6.76}
$$

$$
\begin{aligned}
C_{4element} &= \iiint_{\mathcal{V}} D(x,y,z)_{4element} dv \\
&= \int_{-a}^{a}\int_{-a}^{a}\int_{-a+p}^{a+p} D(x,y,z)_{4element} dxdydz \\
&= \int_{-a}^{a}\int_{-a}^{a}\int_{-a+p}^{a+p} \frac{2}{\sqrt{x^2+y^2+z^2}} \log_2\left(1+\frac{F(x,y,z)_{4element}}{4\pi^2(x^2+y^2)}\right) \\
&- \frac{2F(x,y,z)_{4element}}{4\pi^2(x^2+y^2)\sqrt{x^2+y^2+z^2}+F(x,y,z)_{4element}} dxdydz
\end{aligned}
\tag{6.77}
$$

$$
\begin{aligned}
C_{isotropic} &= \iiint_{\mathcal{V}} D(x,y,z)_{isotropic} dv \\
&= \int_{-a}^{a}\int_{-a}^{a}\int_{-a+p}^{a+p} D(x,y,z)_{isotropic} dxdydz \\
&= \int_{-a}^{a}\int_{-a}^{a}\int_{-a+p}^{a+p} \frac{2}{\sqrt{x^2+y^2+z^2}} \log_2\left(1 + 0.6094 \frac{\eta I^2}{4\pi^2(x^2+y^2+z^2)N}\right) \\
&- \frac{1.288\eta\frac{I^2}{N}}{4\pi^2(\sqrt{x^2+y^2+z^2})^3 + 0.6094\eta\frac{I^2}{N}\sqrt{x^2+y^2+z^2}} dxdydz
\end{aligned} \tag{6.78}
$$

6.8 Numerical Results

In this section, we present the numerical integral results for the total capacity forms derived in Section 6.4 and Section 6.7. The results are also presented in two parts: the sphere shaped volume space case and the cube-shaped volume space case.

6.8.1 Total Capacity of A Sphere

The total capacity values for 4 types of sources at centre derived in (6.15), (6.22), (6.27) and (6.34) are plotted a function of the sphere radius r in Figure 6.7.

The value of $\frac{P}{N}$ can be seen as an equivalence to the signal-to-noise ratio (SNR). In the numerical integral calculation, we choose two values for the $SNR_1 = 5$ and $SNR_2 = 10$. The total capacity values show that the isotropic source has the largest value among the 4 types of sources as we have proved in Proposition 6.2.

The total capacity values of the 4 types sources at non-centre location derived in (6.41), (6.42), (6.43) and (6.44) are plotted in Figure 6.8.

Under the SNR condition set as $SNR = 5$, the total capacity values of the 4 types of sources are plotted against the sphere radius r in two locations $p = 1$ and $p = 2$. The numerical results show that the total capacity values increase with the radius r and the sources at the location $p = 1$ have higher total capacity than the sources at the location $p = 2$.

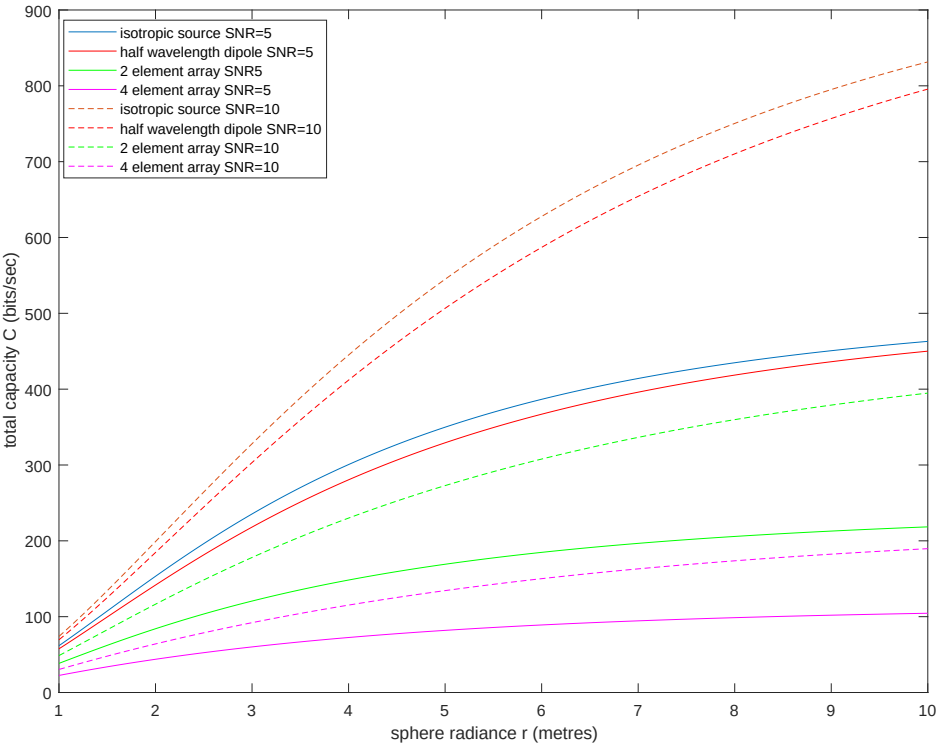

FIGURE 6.7: Total Capacity of Sphere with Centre Source Vs Sphere Radius

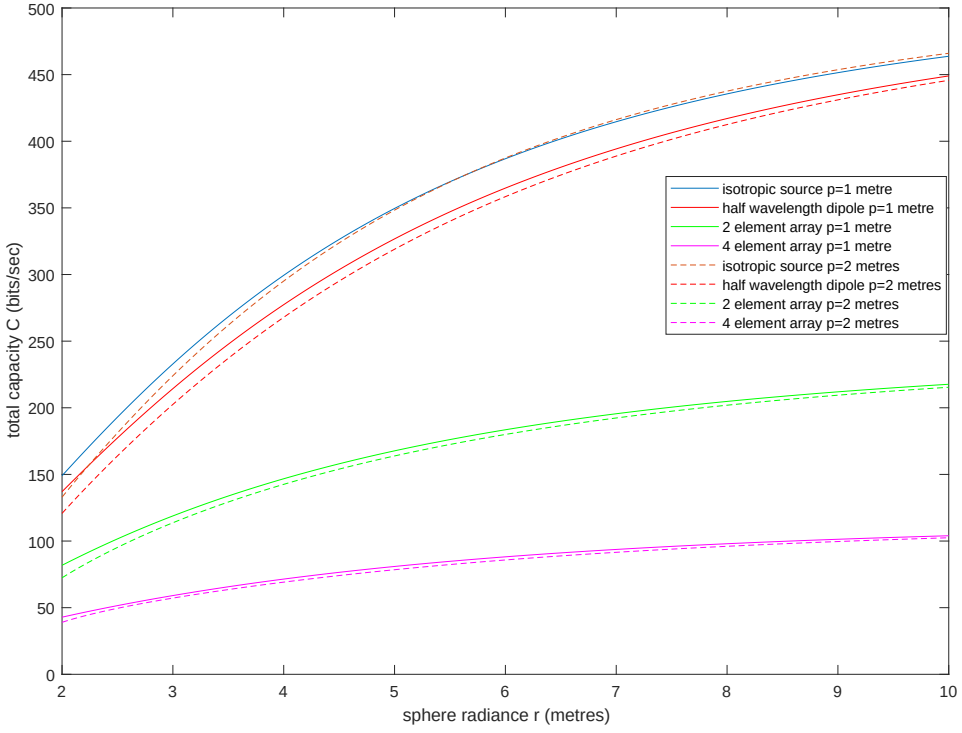

FIGURE 6.8: Total Capacity of Sphere with Non-centre Source Vs Sphere Radius

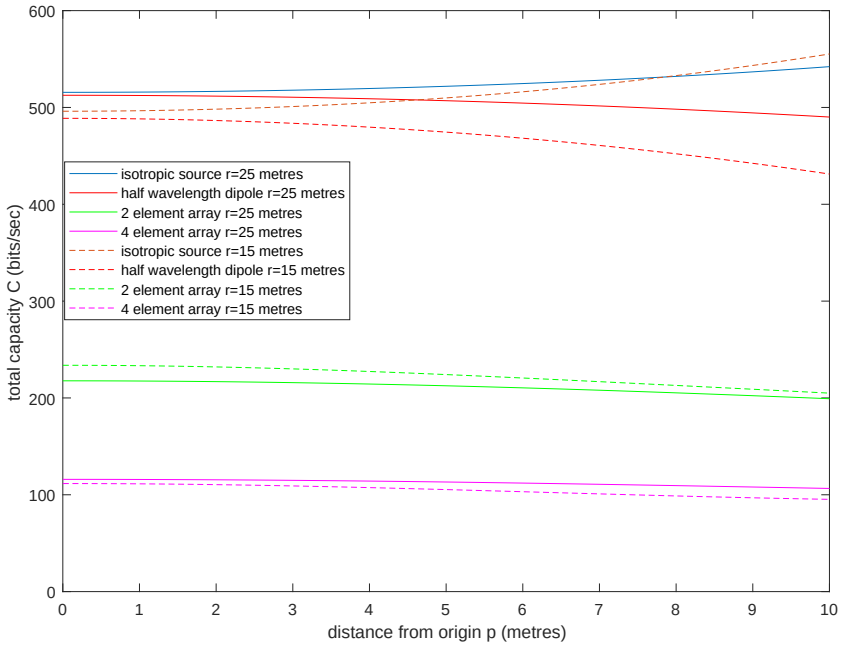

FIGURE 6.9: Total Capacity of Sphere with Non-Centre Source Vs Shift Distance

The total capacity values are also plotted against the distance from the origin p in Figure 6.9. The total capacity values decrease with the distance p as we have proved in Proposition 6.3.

6.8.2 Total Capacity of A Cube

The numerical results of the total capacity of a cube-shaped volume space with a centre source derived in (6.71), (6.72), (6.73) and (6.74) are plotted as a function of half the cube-edge length l in Figure 6.10. The SNR are set as $SNR_1 = 5$ and $SNR_2 = 10$.

The numerical results of the total capacity show similar pattern as in the sphere-shaped case. The total capacity increase with the total volume space and the isotropic source has the largest total capacity.

The numerical results of the total capacity with a non-centre source derived in (6.75), (6.76), (6.77) and (6.78) are plotted in Figure 6.11. The SNR is set as $SNR = 5$ and the positions of the source are chosen as $p = 1$ and $p = 2$.

Again, the numerical values of the total capacity show similar pattern as in the sphere case. The nearer position to the centre (p=1) has a larger total capacity than the farther

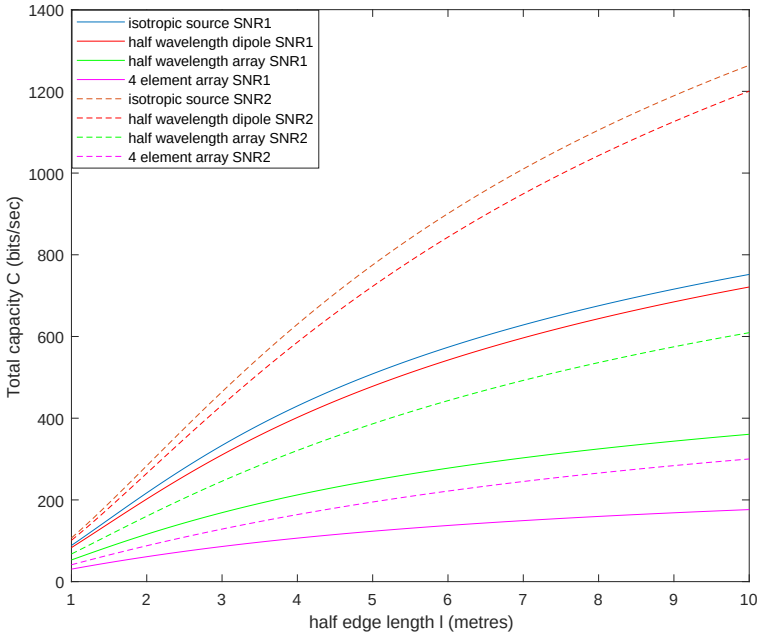

FIGURE 6.10: Total Capacity of Cube with Centre Source Vs Cube Edge Length

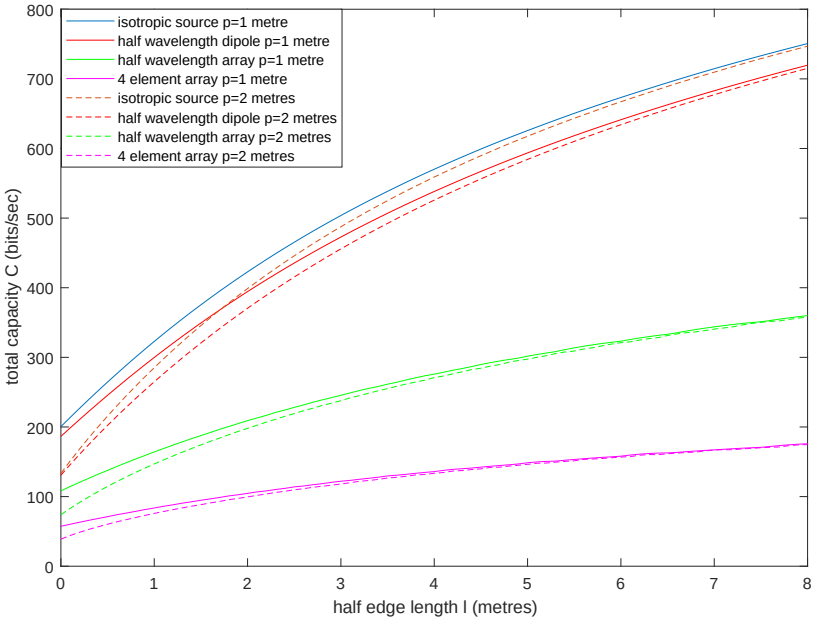

FIGURE 6.11: Total Capacity of Cube with Non-Centre Source Vs Cube Edge Length

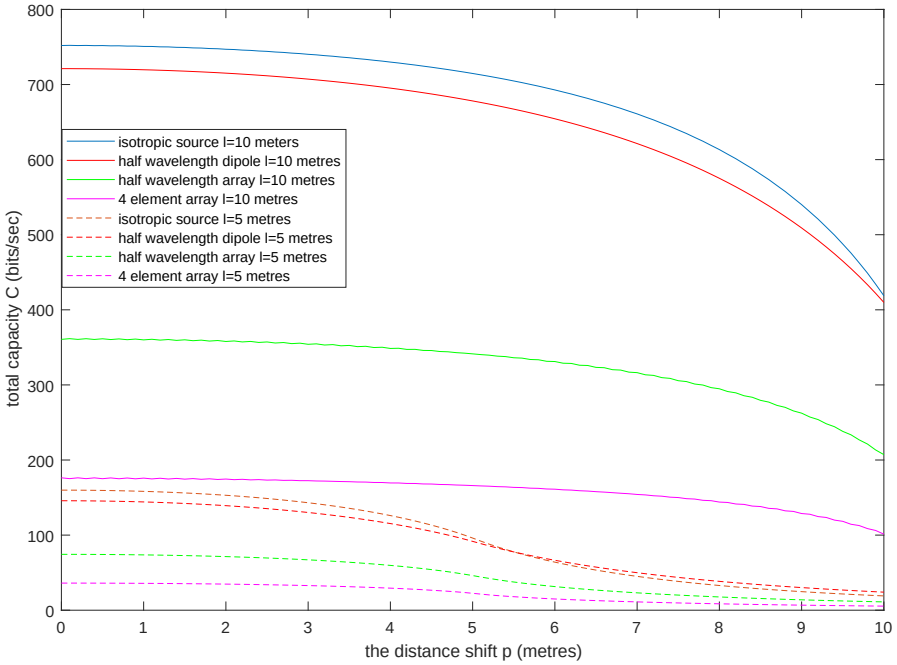

FIGURE 6.12: Total Capacity of Cube with Non-centre Source Vs Shift Distance

position (p=2). The numerical values of the total capacity are also plotted against the distance from the centre in Figure 6.12.

The results again show similar pattern as in the sphere case. The centre position has the largest total capacity of a cube-shaped volume space.

6.9 Discussion and Conclusion

From the integral forms of total capacity derived in Section 6.4 and Section 6.7 and the numerical results in Section 6.8, we have the following conclusions regarding the total capacity of a volume space :

6.9.1 The total capacity increases with the space volume

From both the sphere and cube case, the total capacity increases with the space volume, even with a fixed transmitter power. This result suggests that the capacity of a wireless

channel can always be increased through the increase of the usable spatial degree-of-freedom. Even with a limited transmit power, spreading the power into more degree-of-freedom always results in a positive capacity gain.

6.9.2 Isotropic radiating source has largest total capacity

Conventional antenna design aims to achieve highly directive transmitter antenna by using array, which is based on the point-to-point communication model. However, this conclusion offers an sight to the capacity of wireless channel and the design of communication EM radiating system. To improve the total capacity, it is desirable to spread the total transmitter power into more spatial degree-of-freedom.

6.9.3 Conclusion

In this work, we study the wireless channel capacity limit from electromagnetic perspective. We establish a capacity flow density field based on the power flow density and the classic AWGN channel capacity. Based on the capacity flow density we introduced a new wireless channel capacity limit of volume space, by incorporating the continuous electromagnetic field to study the conventional discrete point-based communication channel. Our results of the total capacity of enclosed volume space show that the capacity of wireless channel always gains through the abundance of the space volume.

The main contribution of this chapter is to calculate the wireless channel capacity of an enclosed volume space. Although the MIMO communication theory proved the number of antennas commands the channel capacity of a MIMO system, the impact of spatial volume on the wireless channel capacity was unknown before this work. In this chapter, the numerical calculation results quantify the amount of wireless channel capacity which a certain spatial volume can support. The results showed that the larger volume space supports higher channel capacity. Such results corroborate the general conclusion of wireless communications that spatial degree-of-freedoms can increase wireless channel capacity.

Chapter 7

Conclusion and Future Work

7.1 Conclusion

In this chapter, I conclude the PhD research project on channel modelling for wireless network planning. I further discuss the limitation of the research presented in this project and presented potential future research directions.

In this PhD research project, I developed advanced channel models for 5G wireless network planning and optimisation. The focus is on massive MIMO channel, mmWave channel and distributed MIMO. Based on traditional ray launching simulation, site-specific channel models are developed for network planning and optimisation applications. Traditional ray launching simulation has been shown to be extended to accommodate the 5G network techniques and still effective in channel map construction. A new model calibration method is also developed and shown to be effective when measurement is available. Furthermore a wireless channel capacity concept from electromagnetic propagation perspective is defined and demonstrated to have potential application network planning and optimisation.

For massive MIMO system, the large number of antenna array posed computational complexity barrier on the physical channel modelling. However, the analysis in this project showed that the physical model can be simplified by utilising the geometry of the large antenna arrays in the massive MIMO systems.

For mmWave channels, the high free space propagation loss can be exploited to develop efficient channel models. In this project, a path loss model for mmWave channel is developed using the high free space loss characteristics. This model has shown accurate prediction results in indoor environment.

For distributed MIMO network planning and optimisation, conventional single antenna channel map is incapable of supporting accurate optimisation. By extending the single antenna channel map to a MIMO channel map, it is used to demonstrate the optimisation of a distributed MIMO network.

Model calibration plays a key part in the process of channel modelling. An efficient LS calibration method is developed to improve the accuracy of the model output when measurement is available. It showed its effectiveness in improving the channel prediction.

Capacity is a key communication network performance metric. In this project, a new wireless channel capacity concept is developed from electromagnetic propagation perspective. It has the potential to be used in indoor network planning and optimisation. The channel capacity is also studied under various environment setting to demonstrate the impact of the environment.

In this PhD project, I have developed advanced site-specific channel prediction models for 5G networks. By exploiting the physical channel features, effective channel models are developed and validated. Ray launching is shown to be an effective choice for site-specific channel modelling in wireless network planning and optimisation. By offering computational efficiency and modelling accuracy, ray launching is demonstrated to be capable of incorporating novel wireless communication techniques in 5G networks.

7.2 Discussion

The channel model in this project has been focused on path loss modelling. Although in network planning and optimisation application path loss is a key channel parameter, other channel parameters are also important in planning and optimisation the network performance. Ray launching simulation is still capable of predicting the other channel parameters by simulating the electromagnetic propagation. With the demands from

future network planning and optimisation, ray launching simulation continues to be an ideal choice for site-specific channel modelling tool.

For mmWave channels, many characteristics of this frequency band have yet been fully known. Due to the high loss and attenuation of mmWave, the transmission range is reduced and the multipath components are also reduced. However, these channel characteristics have yet been fully investigated in this thesis.

7.3 Future Work

Ray launching can be extended to model other channel parameters and characteristics, especially multipath propagation characteristics, including fading statistics, delay spread and angle spread. The location information is naturally associated with the physical model of ray launching. Therefore, one future research direction is to construct channel maps for other channel parameters, including fading map and delay map. These channel maps offer key channel information in wireless network planning and optimisation.

A new trend is to use data driven channel modelling techniques. With the availability of the large environment data from various cities, buildings and application scenarios, channel models can be developed utilising these environment data and more complex machining learning techniques and models can be introduced to develop complex channel models.

In Chapter 6, a new channel capacity is given and some simple capacity results for enclosed volume space are presented. In order to understand the impact of propagation mechanisms on channel capacity, more complex propagation environment can be included in the settings. One future research direction is to study the impact of propagation mechanisms on the channel capacity.

Bibliography

[1] A. Mishra, *Advanced Cellular Network Planning and Optimisation: 2G/2.5G/3G...Evolution to 4G*, ser. IT Pro. Wiley, 2007. [Online]. Available: http://books.google.co.uk/books?id=Y-91Z3y-gokC

[2] H. Sherali, C. Pendyala, and T. Rappaport, "Optimal location of transmitters for micro-cellular radio communication system design," *Selected Areas in Communications, IEEE Journal on*, vol. 14, no. 4, pp. 662–673, May 1996.

[3] E. Amaldi, A. Capone, and F. Malucelli, "Planning umts base station location: optimization models with power control and algorithms," *Wireless Communications, IEEE Transactions on*, vol. 2, no. 5, pp. 939–952, Sept 2003.

[4] I. Siomina, P. Varbrand, and D. Yuan, "Automated optimization of service coverage and base station antenna configuration in umts networks," *Wireless Communications, IEEE*, vol. 13, no. 6, pp. 16–25, Dec 2006.

[5] H. Liang, B. Wang, W. Liu, and H. Xu, "A novel transmitter placement scheme based on hierarchical simplex search for indoor wireless coverage optimization," *Antennas and Propagation, IEEE Transactions on*, vol. 60, no. 8, pp. 3921–3932, Aug 2012.

[6] X. Chu, D. Lopez-Perez, Y. Yang, and F. Gunnarsson, *Heterogeneous Cellular Networks: Theory, Simulation and Deployment*. Cambridge University Press, 2013.

[7] S. Seidel and T. Rappaport, "914 mhz path loss prediction models for indoor wireless communications in multifloored buildings," *Antennas and Propagation, IEEE Transactions on*, vol. 40, no. 2, pp. 207–217, Feb 1992.

[8] G. Durgin, T. Rappaport, and H. Xu, "Radio path loss and penetration loss measurements in and around homes and trees at 5.85 ghz," in *Antennas and Propagation Society International Symposium, 1998. IEEE*, vol. 2, June 1998, pp. 618–621 vol.2.

[9] S. Fortune, D. Gay, B. Kernighan, O. Landron, R. Valenzuela, and M. Wright, "Wise design of indoor wireless systems: practical computation and optimization," *Computational Science Engineering, IEEE*, vol. 2, no. 1, pp. 58–68, Spring 1995.

[10] R. Torres, L. Valle, M. Domingo, and M. Diez, "Cindoor: an engineering tool for planning and design of wireless systems in enclosed spaces," *Antennas and Propagation Magazine, IEEE*, vol. 41, no. 4, pp. 11–22, Sep 1999.

[11] H. Suzuki and A. Mohan, "Measurement and prediction of high spatial resolution indoor radio channel characteristic map," *Vehicular Technology, IEEE Transactions on*, vol. 49, no. 4, pp. 1321–1333, Jul 2000.

[12] J.-M. Gorce, K. Jaffres-Runser, and G. de la Roche, "Deterministic approach for fast simulations of indoor radio wave propagation," *Antennas and Propagation, IEEE Transactions on*, vol. 55, no. 3, pp. 938–948, March 2007.

[13] A. Molina, G. Athanasiadou, and A. Nix, "The automatic location of base-stations for optimised cellular coverage: a new combinatorial approach," in *Vehicular Technology Conference, 1999 IEEE 49th*, vol. 1, Jul 1999, pp. 606–610 vol.1.

[14] A. Mishra, *Advanced Cellular Network Planning and Optimisation: 2G/2.5G/3G...Evolution to 4G*, ser. IT Pro. Wiley, 2007. [Online]. Available: http://books.google.co.uk/books?id=BRMfAQAAIAAJ

[15] S. Salous, *Radio Propagation Measurement and Channel Modelling*. Wiley, 2013. [Online]. Available: http://books.google.co.uk/books?id=3Al4uqB66KUC

[16] F. Ikegami, T. Takeuchi, and S. Yoshida, "Theoretical prediction of mean field strength for urban mobile radio," *Antennas and Propagation, IEEE Transactions on*, vol. 39, no. 3, pp. 299–302, Mar 1991.

[17] F. Ikegami, S. Yoshida, T. Takeuchi, and M. Umehira, "Propagation factors controlling mean field strength on urban streets," *Antennas and Propagation, IEEE Transactions on*, vol. 32, no. 8, pp. 822–829, Aug 1984.

[18] M. Lawton and J. McGeehan, "The application of a deterministic ray launching algorithm for the prediction of radio channel characteristics in small-cell environments," *Vehicular Technology, IEEE Transactions on*, vol. 43, no. 4, pp. 955–969, Nov 1994.

[19] V. Erceg, S. Fortune, J. Ling, A. Rustako, and R. Valenzuela, "Comparisons of a computer-based propagation prediction tool with experimental data collected in urban microcellular environments," *Selected Areas in Communications, IEEE Journal on*, vol. 15, no. 4, pp. 677–684, May 1997.

[20] S.-C. Kim, J. Guarino, B.J., I. Willis, T., V. Erceg, S. Fortune, R. Valenzuela, L. Thomas, J. Ling, and J. Moore, "Radio propagation measurements and prediction using three-dimensional ray tracing in urban environments at 908 mhz and 1.9 ghz," *Vehicular Technology, IEEE Transactions on*, vol. 48, no. 3, pp. 931–946, May 1999.

[21] H.-W. Son and N.-H. Myung, "A deterministic ray tube method for microcellular wave propagation prediction model," *Antennas and Propagation, IEEE Transactions on*, vol. 47, no. 8, pp. 1344–1350, Aug 1999.

[22] M. Catedra, J. Perez, F. Saez de Adana, and O. Gutierrez, "Efficient ray-tracing techniques for three-dimensional analyses of propagation in mobile communications: application to picocell and microcell scenarios," *Antennas and Propagation Magazine, IEEE*, vol. 40, no. 2, pp. 15–28, Apr 1998.

[23] F. de Adana, O. Gutierrez Blanco, I. Diego, J. Perez Arriaga, and M. Catedra, "Propagation model based on ray tracing for the design of personal communication systems in indoor environments," *Vehicular Technology, IEEE Transactions on*, vol. 49, no. 6, pp. 2105–2112, Nov 2000.

[24] Z. Yun, Z. Zhang, and M. Iskander, "A ray-tracing method based on the triangular grid approach and application to propagation prediction in urban environments," *Antennas and Propagation, IEEE Transactions on*, vol. 50, no. 5, pp. 750–758, May 2002.

[25] R. Mathar, M. Reyer, and M. Schmeink, "A cube oriented ray launching algorithm for 3d urban field strength prediction," in *Communications, 2007. ICC '07. IEEE International Conference on*, June 2007, pp. 5034–5039.

[26] Z. Lai, G. De La ROCHE, N. Bessis, P. Kuonen, G. CLAPWORTHY, D. Zhou, and J. Zhang, "Intelligent ray launching algorithm for indoor scenarios," *Radio Engineering*, vol. 20, no. 2, p. 399, 2011.

[27] A. Schmitz, T. Rick, T. Karolski, T. Kuhlen, and L. Kobbelt, "Efficient rasterization for outdoor radio wave propagation," *Visualization and Computer Graphics, IEEE Transactions on*, vol. 17, no. 2, pp. 159–170, Feb 2011.

[28] F. Boccardi, R. Heath, A. Lozano, T. Marzetta, and P. Popovski, "Five disruptive technology directions for 5g," *Communications Magazine, IEEE*, vol. 52, no. 2, pp. 74–80, February 2014.

[29] A. Burr, "Evaluation of capacity of indoor wireless mimo channel using ray tracing," in *Broadband Communications, 2002. Access, Transmission, Networking. 2002 International Zurich Seminar on*, 2002, pp. 28–1–28–6.

[30] S.-H. Oh and N. H. Myung, "Mimo channel estimation method using ray-tracing propagation model," *Electronics Letters*, vol. 40, no. 21, pp. 1350–1352, 2004.

[31] Y. Gao, X. Chen, and C. Parini, "Experimental evaluation of indoor mimo channel capacity based on ray tracing," in *London Communication Symp., University College London*, 2004, pp. 189–192.

[32] O. Stäbler, "Mimo channel characteristics computed with 3d ray tracing model," in *COST2100 TD(08) Workshop, June, 2008, Trondheim, Norway*.

[33] S. Loredo, A. Rodriguez-Alonso, and R. Torres, "Indoor mimo channel modeling by rigorous go/utd-based ray tracing," *Vehicular Technology, IEEE Transactions on*, vol. 57, no. 2, pp. 680–692, 2008.

[34] R. Hoppe, J. Ramuh, H. Buddendick, O. Stabler, and G. Wolfle, "Comparison of mimo channel characteristics computed by 3d ray tracing and statistical models," in *Antennas and Propagation, 2007. EuCAP 2007. The Second European Conference on*, 2007, pp. 1–5.

[35] T. S. Rappaport, S. Sun, R. Mayzus, H. Zhao, Y. Azar, K. Wang, G. N. Wong, J. K. Schulz, M. Samimi, and F. Gutierrez, "Millimeter wave mobile communications for 5g cellular: It will work!" *IEEE Access*, vol. 1, pp. 335–349, 2013.

[36] N. Obeid, M. Heddebaut, F. Boukour, C. Loyez, and N. Rolland, "Millimeter wave ultra wide band short range radar localization accuracy," in *Vehicular Technology Conference, 2009. VTC Spring 2009. IEEE 69th*, April 2009, pp. 1–5.

[37] G. Zhu, D. Guidotti, F. Lin, Q. Wang, J. Cui, Q. Wang, L. Cao, T. Ye, and L. Wan, "Millimeter wave interchip communication," in *Millimeter Waves (GSMM), 2012 5th Global Symposium on*, May 2012, pp. 471–476.

[38] W. H. Chen, S. Joo, S. Sayilir, R. Willmot, T. Y. Choi, D. Kim, J. Lu, D. Peroulis, and B. Jung, "A 6-gb/s wireless inter-chip data link using 43-ghz transceivers and bond-wire antennas," *IEEE Journal of Solid-State Circuits*, vol. 44, no. 10, pp. 2711–2721, Oct 2009.

[39] M. Peter, R. Felbecker, W. Keusgen, and J. Hillebrand, "Measurement-based investigation of 60 ghz broadband transmission for wireless in-car communication," in *Vehicular Technology Conference Fall (VTC 2009-Fall), 2009 IEEE 70th*, Sept 2009, pp. 1–5.

[40] A. P. Garcia, W. Kotterman, R. S. Thoma, U. Trautwein, D. Bruckner, W. Wirnitzer, and J. Kunisch, "60 ghz in-cabin real-time channel sounding," in *Communications and Networking in China, 2009. ChinaCOM 2009. Fourth International Conference on*, Aug 2009, pp. 1–5.

[41] M. Beltran, R. Llorente, R. Sambaraju, and J. Marti, "60 ghz uwb-over-fiber system for in-flight communications," in *Microwave Symposium Digest, 2009. MTT '09. IEEE MTT-S International*, June 2009, pp. 5–8.

[42] S. Hur, T. Kim, D. J. Love, J. V. Krogmeier, T. A. Thomas, and A. Ghosh, "Multilevel millimeter wave beamforming for wireless backhaul," in *GLOBECOM Workshops (GC Wkshps), 2011 IEEE*, Dec 2011, pp. 253–257.

[43] C. Gustafson, K. Haneda, S. Wyne, and F. Tufvesson, "On mm-Wave Multi-path Clustering and Channel Modeling," *IEEE Transactions on Antennas and Propagation*, vol. 62, no. 3, pp. 1445–1455, 2014. [Online]. Available: http://lup.lub.lu.se/record/4276705/file/4276756.pdf

[44] C. Gustafson and F. Tufvesson, "Characterization of 60 GHz Shadowing by Human Bodies and Simple Phantoms," *Radioengineering*, vol. 21, no. 4,

pp. 979–984, 2012. [Online]. Available: http://www.radioeng.cz/fulltexts/2012/12_04_0979_0984.pdf

[45] K. Haneda, C. Gustafson, and S. Wyne, "60 GHz Spatial Radio Transmission: Multiplexing or Beamforming?" *IEEE Transactions on Antennas and Propagation*, vol. 61, no. 11, pp. 5735–5743, 2013. [Online]. Available: http://dx.doi.org/10.1109/TAP.2013.2279091

[46] P. Smulders, "Statistical characterization of 60-ghz indoor radio channels," *IEEE Transactions on Antennas and Propagation*, vol. 57, no. 10, pp. 2820–2829, Oct 2009.

[47] M. R. Akdeniz, Y. Liu, M. K. Samimi, S. Sun, S. Rangan, T. S. Rappaport, and E. Erkip, "Millimeter wave channel modeling and cellular capacity evaluation," *Selected Areas in Communications, IEEE Journal on*, vol. 32, no. 6, pp. 1164–1179, 2014.

[48] T. S. Rappaport, F. Gutierrez, E. Ben-Dor, J. N. Murdock, Y. Qiao, and J. I. Tamir, "Broadband millimeter-wave propagation measurements and models using adaptive-beam antennas for outdoor urban cellular communications," *IEEE Transactions on Antennas and Propagation*, vol. 61, no. 4, pp. 1850–1859, April 2013.

[49] P. Bernardi, R. Cicchetti, and O. Testa, "An accurate utd model for the analysis of complex indoor radio environments in microwave wlan systems," *Antennas and Propagation, IEEE Transactions on*, vol. 52, no. 6, pp. 1509–1520, 2004.

[50] T. Sarkar, Z. Ji, K. Kim, A. Medouri, and M. Salazar-Palma, "A survey of various propagation models for mobile communication," *Antennas and Propagation Magazine, IEEE*, vol. 45, no. 3, pp. 51–82, June 2003.

[51] S. Tan and H. Tan, "Improved three-dimensional ray tracing technique for microcellular propagation models," *Electronics Letters*, vol. 31, no. 17, pp. 1503–1505, 1995.

[52] S. Y. Seidel and T. S. Rappaport, "Site-specific propagation prediction for wireless in-building personal communication system design," *IEEE Transactions on Vehicular Technology*, vol. 43, no. 4, pp. 879–891, Nov 1994.

[53] M. Luo, G. Villemaud, J.-M. Gorce, and J. Zhang, "Realistic prediction of ber and amc for indoor wireless transmissions," *Antennas and Wireless Propagation Letters, IEEE*, vol. 11, pp. 1084–1087, 2012.

[54] F. Boccardi, R. W. Heath, Jr., A. Lozano, T. L. Marzetta, and P. Popovski, "Five Disruptive Technology Directions for 5G," *ArXiv e-prints*, Dec. 2013.

[55] F. Rusek, D. Persson, B. K. Lau, E. Larsson, T. Marzetta, O. Edfors, and F. Tufvesson, "Scaling up mimo: Opportunities and challenges with very large arrays," *Signal Processing Magazine, IEEE*, vol. 30, no. 1, pp. 40–60, 2013.

[56] E. G. Larsson, F. Tufvesson, O. Edfors, and T. L. Marzetta, "Massive MIMO for Next Generation Wireless Systems," *ArXiv e-prints*, Apr. 2013.

[57] Z. Lai, N. Bessis, G. de la Roche, P. Kuonen, J. Zhang, and G. Clapworthy, "On the use of an intelligent ray launching for indoor scenarios," in *Antennas and Propagation (EuCAP), 2010 Proceedings of the Fourth European Conference on*, 2010, pp. 1–5.

[58] I. Cuiñas and M. G. Sánchez, "Permittivity and conductivity measurements of building materials at 5.8 ghz and 41.5 ghz," *Wireless Personal Communications*, vol. 20, no. 1, pp. 93–100, 2002. [Online]. Available: http://dx.doi.org/10.1023/A:1013886209664

[59] X. Tu, H. Hu, Z. Lai, J.-M. Gorce, and J. Zhang, "Performance comparison of mr-fdpf and ray launching in an indoor office scenario," in *Antennas and Propagation Conference (LAPC), 2013 Loughborough*, 2013, pp. 424–428.

[60] R. Kouyoumjian and P. Pathak, "A uniform geometrical theory of diffraction for an edge in a perfectly conducting surface," *Proceedings of the IEEE*, vol. 62, no. 11, pp. 1448–1461, 1974.

[61] X. Gao, O. Edfors, F. Rusek, and F. Tufvesson, "Massive mimo performance evaluation based on measured propagation data," *IEEE Transactions on Wireless Communications*, vol. 14, no. 7, pp. 3899–3911, July 2015.

[62] J. Voigt, R. Fritzsche, and J. Schueler, "Optimal antenna type selection in a real su-mimo network planning scenario," in *Vehicular Technology Conference Fall (VTC 2009-Fall), 2009 IEEE 70th*, 2009, pp. 1–5.

[63] S. Payami and F. Tufvesson, "Channel measurements and analysis for very large array systems at 2.6 ghz," in *Antennas and Propagation (EUCAP), 2012 6th European Conference on*, 2012, pp. 433–437.

[64] A. Abdi, C. Tepedelenlioglu, M. Kaveh, and G. Giannakis, "On the estimation of the k parameter for the rice fading distribution," *Communications Letters, IEEE*, vol. 5, no. 3, pp. 92–94, 2001.

[65] X. Gao, F. Tufvesson, O. Edfors, and F. Rusek, "Measured propagation characteristics for very-large mimo at 2.6 ghz," in *2012 Conference Record of the Forty Sixth Asilomar Conference on Signals, Systems and Computers (ASILOMAR)*, Nov 2012, pp. 295–299.

[66] C. Fang, A. Alayn-Glazunov, F. Tufvesson, and J. Zhang, "Mimo channel measurement in indoor and ourdoor environment," University of Bedfordshire, Luton, UK, Technical Report, Tech. Rep., 2010.

[67] N. Razavi-Ghods and S. Salous, "Wideband mimo channel characterization in tv studios and inside buildings in the 2.22.5 ghz frequency band," *Radio Science*, vol. 44, no. 5, 2009. [Online]. Available: http://dx.doi.org/10.1029/2008RS004095

[68] S. Salous, S. M. Feeney, X. Raimundo, and A. A. Cheema, "Wideband mimo channel sounder for radio measurements in the 60 ghz band," *IEEE Transactions on Wireless Communications*, vol. 15, no. 4, pp. 2825–2832, April 2016.

[69] F. Mani, F. Quitin, and C. Oestges, "Directional spreads of dense multipath components in indoor environments: Experimental validation of a ray-tracing approach," *Antennas and Propagation, IEEE Transactions on*, vol. 60, no. 7, pp. 3389–3396, July 2012.

[70] V. Degli-Esposti, V. Kolmonen, E. Vitucci, and P. Vainikainen, "Analysis and modeling on co- and cross-polarized urban radio propagation for dual-polarized mimo wireless systems," *Antennas and Propagation, IEEE Transactions on*, vol. 59, no. 11, pp. 4247–4256, 2011.

[71] T. Rappaport, *Wireless Communications: Principles and Practice*, 2nd ed. Upper Saddle River, NJ, USA: Prentice Hall PTR, 2001.

[72] K. Sato, T. Manabe, T. Ihara, H. Saito, S. Ito, T. Tanaka, K. Sugai, N. Ohmi, Y. Murakami, M. Shibayama, Y. Konishi, and T. Kimura, "Measurements of reflection and transmission characteristics of interior structures of office building in the 60-ghz band," *IEEE Transactions on Antennas and Propagation*, vol. 45, no. 12, pp. 1783–1792, Dec 1997.

[73] D. Tse and P. Viswanath, *Fundamentals of Wireless Communication*, ser. Wiley series in telecommunications. Cambridge University Press, 2005. [Online]. Available: http://books.google.co.uk/books?id=66XBb5tZX6EC

[74] T. Sarkar, S. Burintramart, N. Yllmazerl, Y. Zhang, A. Del, M. Salazar-Palma, M. Lagunas, E. Mokole, and M. Wicks, "A look at the concept of channel capacity from a maxwellian viewpoint," *Antennas and Propagation Magazine, IEEE*, vol. 50, no. 3, pp. 21–50, June 2008.

[75] J. D. Jackson, *Classical Electrodynamics Third Edition*, 3rd ed. Wiley, 1998.

[76] G. J. Foschini, "Layered space-time architecture for wireless communication in a fading environment when using multi-element antennas," *Bell Labs Technical Journal*, vol. 1, no. 2, pp. 41–59, 1996.

[77] E. Telatar, "Capacity of multi-antenna gaussian channels," *European Transactions on Telecommunications*, vol. 10, no. 6, pp. 585–595, 1999.

[78] H. V. Balan, R. Rogalin, A. Michaloliakos, K. Psounis, and G. Caire, "Achieving high data rates in a distributed mimo system," in *Proceedings of the 18th Annual International Conference on Mobile Computing and Networking*, ser. Mobicom '12, 2012, pp. 41–52.

[79] http://www.ranplan.co.uk, accessed January 15, 2017.

[80] B. Clerckx and C. Oestges, *MIMO Wireless Networks: Channels, Techniques and Standards for Multi-Antenna, Multi-User and Multi-Cell Systems*. Academic Press, 2013.

[81] O. Stabler and R. Hoppe, "Mimo channel capacity computed with 3d ray tracing model," in *Antennas and Propagation, 2009. EuCAP 2009. 3rd European Conference on*, 2009, pp. 2271–2275.

[82] G. de la Roche and J. M. Gorce, "A 3d formulation of mr-fdpf for simulating indoor radio propagation," in *2006 First European Conference on Antennas and Propagation*, Nov 2006, pp. 1–6.

[83] G. de la Roche, J. F. Wagen, G. Villemaud, J. M. Gorce, and J. Zhang, "Comparison between two implementations of parflow for simulating femtocell networks," in *2011 Proceedings of 20th International Conference on Computer Communications and Networks (ICCCN)*, July 2011, pp. 1–4.

[84] G. Kramer, I. Marić, and R. D. Yates, "Cooperative communications," *Foundations and Trends® in Networking*, vol. 1, no. 3, pp. 271–425, 2006.

[85] F. Mazda, *Telecommunications Engineer's Reference Book*. Elsevier Science, 2014. [Online]. Available: https://books.google.co.uk/books?id=x51lAwAAQBAJ

[86] S. Alamouti, "A simple transmit diversity technique for wireless communications," *Selected Areas in Communications, IEEE Journal on*, vol. 16, no. 8, pp. 1451–1458, Oct 1998.

[87] E. Biglieri, J. Proakis, and S. Shamai, "Fading channels: information-theoretic and communications aspects," *Information Theory, IEEE Transactions on*, vol. 44, no. 6, pp. 2619–2692, Oct 1998.

[88] P. Gupta and P. Kumar, "The capacity of wireless networks," *Information Theory, IEEE Transactions on*, vol. 46, no. 2, pp. 388–404, Mar 2000.

[89] J. Andrews, F. Baccelli, and R. Ganti, "A tractable approach to coverage and rate in cellular networks," *Communications, IEEE Transactions on*, vol. 59, no. 11, pp. 3122–3134, November 2011.

[90] O. Bucci and G. Franceschetti, "On the spatial bandwidth of scattered fields," *Antennas and Propagation, IEEE Transactions on*, vol. 35, no. 12, pp. 1445–1455, Dec 1987.

[91] ——, "On the degrees of freedom of scattered fields," *Antennas and Propagation, IEEE Transactions on*, vol. 37, no. 7, pp. 918–926, Jul 1989.

[92] J. Xu and R. Janaswamy, "Electromagnetic degrees of freedom in 2-d scattering environments," *Antennas and Propagation, IEEE Transactions on*, vol. 54, no. 12, pp. 3882–3894, Dec 2006.

[93] R. Janaswamy, "On the em degrees of freedom in scattering environments," *Antennas and Propagation, IEEE Transactions on*, vol. 59, no. 10, pp. 3872–3881, Oct 2011.

[94] F. Gruber and E. Marengo, "New aspects of electromagnetic information theory for wireless and antenna systems," *Antennas and Propagation, IEEE Transactions on*, vol. 56, no. 11, pp. 3470–3484, Nov 2008.

[95] M. Franceschetti and K. Chakraborty, "Space-time duality in multiple antenna channels," *Wireless Communications, IEEE Transactions on*, vol. 8, no. 4, pp. 1733–1743, April 2009.

[96] A. Poon, R. Brodersen, and D. Tse, "Degrees of freedom in multiple-antenna channels: a signal space approach," *Information Theory, IEEE Transactions on*, vol. 51, no. 2, pp. 523–536, Feb 2005.

[97] A. Poon, D. Tse, and R. Brodersen, "Impact of scattering on the capacity, diversity, and propagation range of multiple-antenna channels," *Information Theory, IEEE Transactions on*, vol. 52, no. 3, pp. 1087–1100, March 2006.

[98] D. Migliore, "On the role of the number of degrees of freedom of the field in mimo channels," *Antennas and Propagation, IEEE Transactions on*, vol. 54, no. 2, pp. 620–628, Feb 2006.

[99] ——, "On electromagnetics and information theory," *Antennas and Propagation, IEEE Transactions on*, vol. 56, no. 10, pp. 3188–3200, Oct 2008.

[100] M. Franceschetti, D. Migliore, and P. Minero, "The capacity of wireless networks: Information-theoretic and physical limits," *Information Theory, IEEE Transactions on*, vol. 55, no. 8, pp. 3413–3424, Aug 2009.

[101] S.-H. Lee and S.-Y. Chung, "Capacity scaling of wireless ad hoc networks: Shannon meets maxwell," *Information Theory, IEEE Transactions on*, vol. 58, no. 3, pp. 1702–1715, March 2012.

[102] A. Ozgur, O. Leveque, and D. Tse, "Hierarchical cooperation achieves optimal capacity scaling in ad hoc networks," *Information Theory, IEEE Transactions on*, vol. 53, no. 10, pp. 3549–3572, Oct 2007.

[103] C. E. Shannon, "A mathematical theory of communication," *Bell System Technical Journal*, vol. 27, no. 3, pp. 379–423, 1948. [Online]. Available: http://dx.doi.org/10.1002/j.1538-7305.1948.tb01338.x

[104] W. Jeon and S.-Y. Chung, "The capacity of wireless channels: A physical approach," in *Information Theory Proceedings (ISIT), 2013 IEEE International Symposium on*, July 2013, pp. 3045–3049.

[105] W. Stutzman and G. Thiele, *Antenna Theory and Design*, ser. Antenna Theory and Design. Wiley, 2012. [Online]. Available: http://books.google.co.uk/books?id=xhZRA1K57wIC

[106] L. R©Æde and B. Westergren, *Mathematics Handbook for Science and Engineering*. Springer, 2004. [Online]. Available: https://books.google.co.uk/books?id=zHEjWAgv7joC